DESIGN AND CONTROL OF A
CLOSED-CIRCUIT SERVO-CONTROLLED
MINIATURE HYDRAULIC ROTARY JOINT

DESIGN AND CONTROL OF A CLOSED-CIRCUIT SERVO-CONTROLLED MINIATURE HYDRAULIC ROTARY JOINT

By

MASOUD AREFI, B.Sc., M.Sc.

A Thesis

Submitted to the School of Graduate Studies

in Partial Fulfilment of the Requirements

for the Degree

Master of Applied Science

McMaster University

MASTER OF APPLIED SCIENCE (2008) McMaster University

(Mechanical Engineering) Hamilton, Ontario

TITLE: Design and Control of a Closed-Circuit Servo-Controlled Hydraulic Rotary Joint

AUTHOR: Masoud Arefi, B.Sc., M.Sc. (McMaster University)

SUPERVISOR: Professor Gary M. Bone

NUMBER OF PAGES: xviii, 138

ABSTRACT

In the last few decades, miniaturization has been in increasing demand in many applications. The miniature actuators should comprise high power-weight ratio while having a fast dynamic response, and high efficiency. In this thesis several approaches have been studied to develop a low pressure water hydraulic system driving a miniature rotary joint as the end-effecter. While the system was expected to have a cross sectional diameter of 15 mm, two prototypes were manufactured having cross sections of 12.5 mm x 13 mm (18 mm dia.) and 16 mm x 18 mm (24 mm dia.). The system involves a novel closed-circuit water hydraulic system in which a controlled volume of water supplied by a motor-cylinder pump drives the rotary joint cylinders (4 mm bore). The linear motion of these cylinders is converted to a rotational motion through a sliders-pulley mechanism. The rotation of an arm attached to this pulley is measured by a magnetic rotary encoder.

The dynamic behaviour of the system was studied and the most important parameters have been modelled. This model has been utilized in the design of a model based feedforward (FFWD) controller which was added to a PID controller to enhance the position control of the rotary arm. Numerous experiments were conducted with the horizontal rotation of the rotary arm. The maximum error (e_{max}) recorded for a mixed input (a combination of rising and falling cycloidals of 120° and 60° with pause periods of 1 and 0.5 s) with a PID controller was 8.3° while with the addition of the FFWD term this dropped to 6.2°. The maximum root mean square error (RMSE) for the same trajectory has been 1.7° and 0.9° for PID and FFWD+PID controllers respectively. The steady state error (SSE) which was measured during a cycloidal input of 120° was recorded to be in the range of ±0.2° for both of the controllers. The robustness of the controllers was evaluated by adding a mass of 8.5 g to the end of the rotary arm which produced an un-modelled extra large inertia to the system dynamic when the arm rotating horizontally. Robustness of both controllers was demonstrated as the change in the main numerical performance indicators (RMSE, e_{max}, and SSE) were not remarkable. Another set of experiments performed with the rotary joint positioned vertically introduced with an un-modelled changing force. The numerical performance indicators were almost unchanged again. A comparison between the results of this thesis with the ones from the previous work in our laboratory by R. Sindrey indicates a significant improvement.

ACKNOWLEDGEMENTS

I would like to express my appreciation and gratitude to my supervisor, Professor Gary Bone, for his continued support and direction during this challenging work. He has been a great inspiration for me and I am thankful that I have been given the time to work and learn from him. I am also indebted to the technicians in the machine shop for helping me to complete the experimental setup, as well as my colleagues in the Robotics and Manufacturing Automation Laboratory for their helpful suggestions and support.

My wife and son, Roya and Pouya, deserve a great deal of appreciation for their support, patience, and understanding during my academic endeavour. More than just family, they have been my strongest supporters and motivators. Further, I would like to thank my brother, Rasoul, for his continued support. In addition, I want to thank my brother-in-law, George, for reviewing my thesis and providing valuable advice.

Finally, I would like to dedicate this work and study to my mother and father, who I know in my heart, are pleased at this achievement; although, I will not have the opportunity to share this joy with them.

TABLE OF CONTENTS

LIST OF FIGURES

LIST OF TABLES

NOMENCLATURE

A_1, d_1, r_1	Bore area, diameter, and radius of the pump cylinder
A_2, d_2, r_2	Bore area, diameter, and radius of the joint cylinder
A_i, d_i, r_i	Inner area, diameter, and radius of the tubing
A_o, d_o, r_o	Outer area, diameter, and radius of the tubing
C_v	Viscous friction coefficient
d_p, r_p	Pitch diameter and radius of the pulley
dt	Sampling period
$e, \dot{e}, \int e$	Error between desired and actual arm angles, its derivative, and integral
e_{max}	Maximum tracking error
E, ν	Modulus of elasticity and Poisson's ratio for tubing
f	Total friction
F_1, F_2	Forces on pistons of joint cylinders
F_s, F_c	Static friction, and Coulomb friction
F_{sum}, F_{sumd}	Output force transmitted to rotary joint
$G_p(s)$	Transfer function of the pump
J	Mass moment of inertia
K_p, K_i, K_d	PID controller gains (proportional, integral, derivative)
L_p	Length of tubing
m, m_e	Mass and equivalent mass
M_{max}	Maximum torque transferred to the pulley before string slippage

p_1, p_2	Pressures in line 1 and 2
Re	Reynolds number
$RMSE$	Root mean square error
S	Ratio of air to water in the hydraulic line
SSE	Steady state error
t_p	Wall thickness of tubing
T_1, T_2	Tensions on the string (resistant side, pulling side)
v, a	Water velocity and acceleration
V_p, V_w, V_a	Tubing, water, and air volumes
$x, \dot{x}, \ddot{x}$	Displacement, velocity and acceleration of pump cylinder piston
$y, \dot{y}, \ddot{y}$	Displacement, velocity and acceleration of joint cylinder piston
β	Contact angle between pulley and string
β_e, β_p, β_w, β_a	Effective, tubing, water, and air bulk modulus
θ_a, θ_{ad}	Rotary arm angle (actual, desired)
θ_f	Feedforward angle to pump motor
θ_m, θ_{md}	Pump motor angle (actual, desired)
μ_s	Static friction coefficient between pulley and string
Δp_r, Δp_i	Pressure drop due to hydraulic resistance and inertance
ρ, μ	Water density and viscosity

CHAPTER 1

INTRODUCTION

1.1 Preface

Most of the controlled motion applications rely on traditional electric, pneumatic and hydraulic technologies. In the last few decades, miniaturization has been in increasing demand in many applications such as military, space, optics, medical, robotics and instrumentation. Emerging actuator technologies have attracted more attention in recent years, among which electrostatic, piezoelectric and shape memory alloy are the better candidates for miniature actuators. These actuators should be custom designed and manufactured according to the special requirements of the application. Furthermore, the miniature actuators should comprise high power-weight ratio while having a fast dynamic response and high efficiency. This combination of characteristics cannot be achieved with the existing emerging technologies.

Another solution may be to combine off-the-shelf traditional technologies in a novel way. A miniature low pressure water hydraulic system combines the benefits of a low pressure and cleanliness of pneumatic systems, with the rigidity and controllability of hydraulic systems. Miniature cylinders are commercially available which can be integrated in robotic end-effectors and may be controlled by controlling the pressures or the flow rate of the working fluid. The challenges in these systems are the high static friction which increases the discontinuity near the zero velocity point, and system compliance due to the compressibility of the working fluid and elasticity of the connecting tubing. These effects can dramatically reduce the system performance when a high precision position control is required.

This thesis follows the same objectives as the previous work completed by R. Sindrey [36] in our laboratory while trying to increase the system performance. The main objectives are to build a miniature rotary joint, with a diameter of less than 15 mm, having a rotational range of 180° and being capable of producing a maximum output torque of 20 mNm. The position of the rotary arm should be precisely controlled. The different elements of the system including actuators, rotary joint, and control hardware and software should be studied to develop a system with a higher degree of performance.

1.2 Contents of the Remaining Chapters

This thesis consists of six chapters. The remaining chapters include the following:

Chapter 2: In this chapter the most advanced miniature actuators, their design and applications are first reviewed. Then more attention is given to the previous works related to small pneumatic and hydraulic actuators and their relevant issues. The subjects include the position control approaches, water hydraulic system and techniques to reduce friction.

Chapter 3: This chapter begins with a critical review of the previous work in our laboratory on the design and control of a miniature rotary actuator. Next, different alternative components and designs will be examined to enhance the system performance. Finally a new approach and apparatus will be introduced. The new joint mechanism and system design will be explained in detail.

Chapter 4: The system modeling will be described in this chapter. The model developed in this chapter will be utilized in the model based controller design. The system will be divided into three subsystems: motor-cylinder pump, water power transmission, and rotary joint. Then the most dominant parameters will be identified, and the dynamic of the subsystems and their input/output relations will be mathematically derived. These equations will be implemented in a simulation program, and their validity will be verified by comparing with open-loop tests.

Chapter 5: This chapter will discuss the design of two controllers. A simple PID controller will be enhanced with high frequency signal (dither), error derivative averaging, and initial pressure adjustment to increase the system performance. Next a model based feedforward controller will be designed and added to the PID controller. The experimental results for both of the controllers will be given for a variety of inputs. The robustness of the controllers will be examined by adding an extra mass to the rotating arm and rotating the joint arm in horizontal and vertical positions.

Chapter 6: This chapter presents the conclusions of the research. It commences with a brief summary of the system hardware, modeling, and control. Next, the system performance for both controllers developed in this thesis will be compared to those from the previous work. Finally, a few recommendations for future work will be presented.

CHAPTER 2

LITERATURE REVIEW

2.1 Introduction

This chapter begins with a review of the most developed and refined miniature actuators, their designs and applications. In the remainder, attention is given to pneumatic and hydraulic actuators and relevant issues, including position control, water hydraulic systems, and techniques to reduce friction.

2.2 Applications and Technology

Traditionally, most of the applications involving position or force control have used one and/or a combination of three primary power sources: electric motors, hydraulic cylinders, and pneumatic cylinders [1], [2]. The main advantages and disadvantages of these types of actuators are summarized in Table 2.2.1

In regards to applications which involve miniaturization and micro-actuators, the power to weight ratio and efficiency plays an important role. The limitations of these primary actuation technologies and the need for miniature actuators prompted research into other technologies. Military, space, optics, automotive, medical, robotics and instrumentation applications have stimulated great demand and advances in the field of micro-actuators [3] - [8].

Table 2.2.1: Primary actuators, advantages and disadvantages

Actuator	Advantages	Disadvantages
Electrics	• Clean and easy to use • Medium cost • Low noise • Accurate position and velocity control	• Low power/weight ratio • Indirect drive (generally) • Backlash (due to indirect drive)
Hydraulics	• High power/weight ratio • Low backlash • Direct drive	• Oil leakage (toxic) • High cost • High pressure • Complex control • Noise
Pneumatics	• Low cost • Medium power/weight ratio • Direct drive • Quick response time • Simple 'bang-bang' control • Cleaner than hydraulic	• Difficult position control (due to air compressibility) • Noise

Gilbertson and Busch reviewed different actuator technologies and their applications for miniature spacecraft [9]. Their study included actuators which transform electrical, thermal, or magnetic energy into controllable motion. They noted that the cost of launching a piece of material into the earth's orbit by the Space Shuttle equals half of the item's weight in gold. This showed the importance of power density, the ratio of power to weight of the actuator, in spacecraft design.

2.2.1 Electromagnetic Actuators

DC (brush or brushless) and stepper motors, solenoids, and voice coils are the main types of controllable actuators using electromagnetic force as the driving force. Since this force can be directly controlled by electric signal, they are relatively easy to control.

Electric motors are widely used to provide the power needed in many applications where the combination of space and power is not the primary issue. Usually a transmission system (gearbox, pulleys and belts, sprockets and chain, etc.) is employed to transfer power from the motor to the driven mechanism. The transmission could involve changes in speed (and torque), direction, or a combination of them. These tasks could greatly reduce the efficiency and/or increase the size of the system. Direct drive electric motors are limited by the torque they can generate. This limitation is the major drawback of electric motors, particularly when dealing with miniature position controlled systems.

Miniature motors with a rotor, 1mm in diameter and 0.5mm thick, were reported to be used in micro-cars with an overall dimension of 4.8 mm x 1.8 mm x 1.8 mm [10]. The motor had a similar structure to stepper motors used in quartz watches. The rotating magnet was an isotropic barium ferrite magnet having 4 poles as shown in Figure 2.2.1 [11]. The core shaft was coiled 1,000 turns of copper wire with a diameter of 25 μm. The 3V electric supply with 20 mA current generated a torque of about 1 μNm. The rotor of the motor was joined directly to the front shaft of the micro car. The car was capable of running at a maximum speed of 100 mm/s.

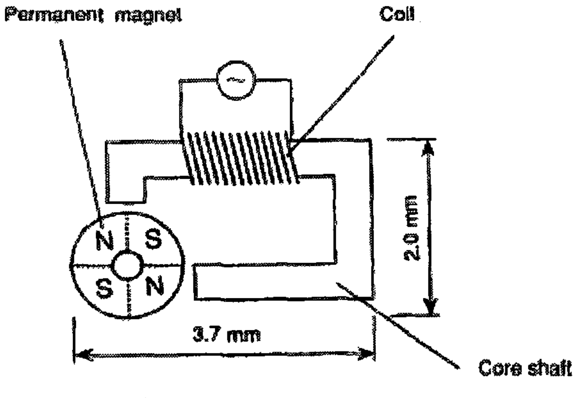

Figure 2.2.1: Electromagnetic motor for micro car [11]

Electric motors are commercially available from several manufacturers in miniature sizes. For example, Minimotor SA, a Faulhaber group company, produces brushless DC-servomotors as small as 6 mm in diameter and 21.9 mm in length capable of generating a maximum torque of 0.37 mNm [12]. Having a weight of 2.5 g, the power-to-weight ratio of this motor is estimated to be 0.63 W/g. Miniature DC motors from Maxon are also available having a diameter of 6 mm and a length of 21 mm and capable of generating a maximum torque of 0.51 mNm [13]. The motor has a weight of 2.8 g with a power-to-weight ratio of 0.43 W/g.

2.2.2 Electrostatic Actuators

The driving force in electrostatic actuators results when two materials having opposite or similar charges approach each other causing an attractive or repulsive force to be generated. The force generated has an inverse relation to the gap between the two opposing materials. That being said, a stronger electrostatic force is generated when this gap is smaller. The extremely low current consumption of this type of actuators categorizes them among the most efficient of actuators. The major drawback is the high voltage requirement of the actuator needed to generate an adequate driving force.

Mehregany, Nagarkar, Senturia, and Lang developed a micro-fabricated harmonic (also known as wobble) electrostatic rotary motor [14], having a rotor diameter of 130 μm and operating at 25 to 36 V at a speed of 2,500 to 15,000 rpm. With this, they managed to generate a torque of up to 0.13 μNm. Their design employed a center bearing to eliminate the necessity for stator insulation (refer to Figure 2.2.2). They also used a hard material

(Si_2N_3) to coat the core shaft and rotor to achieve a higher speed and longer life span, as compared to their previous versions, which lasted for one week at a speed of 10,000 rpm.

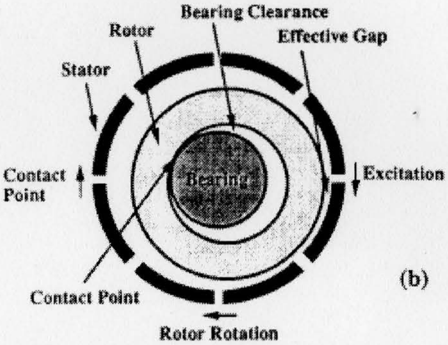

Figure 2.2.2: Structure of a wobble motor [14]

Electrostatic actuators can also be manufactured to act as a linear motion generator. A quad type electrostatic actuator was the basis of the research by Fukuda and Tanaka [15]. This actuator consisted of 4 fixed electrodes made by photo fabrication on a 0.6 mm thick PCB, a spacer, and an elastic movable electrode. A probe made of silicon attached to the moveable electrode was intended to have small displacement (in the order of micrometers) to handle biological cells. They measured the displacement at the tip of the probe by a non-contact eddy current sensor. The actuator required a voltage of approximately 200 V, to achieve a maximum displacement of 8.2 μm.

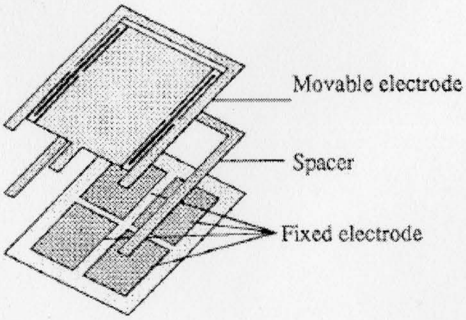

Figure 2.2.3: Structure of a 3DOF electrostatic micromanipulator [5]

2.2.3 Piezoelectric Actuators

Certain materials have the ability to generate proportional electric charges in response to applied force and expand when an electric charge parallel to the direction of polarization of the crystal is applied. Many applications employ this effect for actuating or sensing applications. For instance, in many inkjet printers piezoelectric crystals are used to control the flow of ink from the cartridge.

Piezoelectric actuators are capable of moving large masses over microscopic distances, or light loads at high frequencies. The displacement of a piezoelectric actuator is a function of applied electric field strength, the length of the actuator, the properties of the crystal, and external load. As the force generated by a single crystal is small, usually a piezoelectric actuator is made of several layers. A stacked actuator can achieve a displacement of up to 0.2 % of its total length. The main drawbacks of this technology however, are the small range of motion and sensitivity to temperature change.

There are two main types of piezoelectric actuators: low voltage (100 Volts or less for full extension) and high voltage (1,000 Volts or more for full extension). Low voltage actuators simplify drive electronics and consist of layers, with thicknesses ranging from 0.02 to 0.1 mm. High voltage actuators consist of ceramic disks, with thicknesses ranging from 0.4 to 1.0 mm. They are more suitable than low voltage for applications involving high loads. Piezoelectric actuators can withstand high pressures and exhibit high stiffness.

Roberts et al. developed a novel approach integrating micro-hydraulics and piezoelectric materials [16]. Their system consisted of a circular piston acting as the fluid pumping element, supported by piezoelectric cylinders. The piston was suspended from the circumferential supporting structure by a thin annular micro-machined tether as depicted in Figure 2.2.4. The overall dimension of design was less than 10 mm x 10 mm x 2 mm. The piston displacement reached 1.38 µm, with a sinusoidal voltage of ±500 V at 15 kHz.

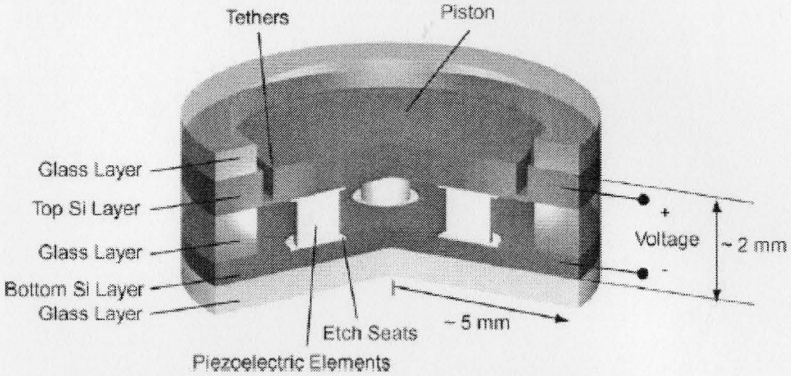

Figure 2.2.4: Piezoelectric actuator for micro-hydraulic application [16]

Ultrasonic motors are special type of piezoelectric actuator. In this type of motor, a piezoelectric ceramic coupled to a stator, is electrically excited with a frequency of 30 to 50 kHz. The vibration of the stator is amplified due to resonance and the rotor (or slider in a linear motor) slides on the stator surface in part due to the friction between the stator and rotor [17]. The ultrasonic motors can offer a wide range of motion in contrast to piezoelectric actuators, which are restricted to the strain of the actuator.

Bexell and Johansson fabricated a piezoelectric inchworm motor with a diameter and height of 4 and 2 mm respectively [18]. The motor consisted of 6 multi-layered piezoceramic elements. Each element included alternating layers of active material (PZT) and palladium electrodes, which separated electrically. Each PZT could be activated separately and caused two modes of motion, bending or longitudinal, according the voltage on each layer (Figure 2.2.5). The periodical activation of two sets of piezoelectric elements, with 180° phase difference, generated an elliptic motion on the tip of the elements, moving the rotor disk with friction force. A maximum torque of 1.4×10^{-3} mNm was achieved experimentally.

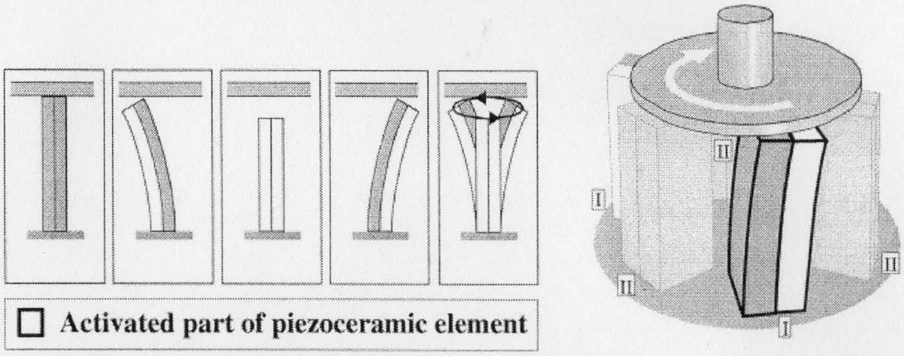

Figure 2.2.5: Working principle of an ultrasonic motor [18]

Ultrasonic motors are commercially available which are currently used in optics and phone camera applications. The world's smallest ultrasonic linear motor has recently been introduced by New Scale Technologies, Inc [19]. The tiny SQL-1.8 SQUIGGLE motor has an overall dimension of 1.8 x 1.8 x 6 mm and weighs only 0.16 g. It can move as fast as 7 mm/s, and is capable of generating a maximum axial force of 0.29 N. The power-to-weight ratio of this actuator is less than 10 mW/g.

2.2.4 Shape Memory Alloy (SMA) Actuators

The shape memory effect was reported more than 50 years ago by Chang and Read, after observing that a gold and copper alloy returned to its original shape when heated after deformation [3]. The heat could be internally generated by the resistance of the SMA material to electric current or induced by an external heat source. The most common SMA is a nickel-titanium alloy (also known as Nitinol), in large part due to its relative non-toxicity, reasonable cost, and suitable electrical resistance.

SMAs have significant features including: the capability of exerting a high force per unit area (more than 200 MPa), high strain rate (300%/s), and a relatively large deformation (greater than 5%). The superior high power density of this actuator (50 W/g) is the highest among the emerging actuators. On the other hand, there are many limitations with these actuators which restrict their use. Their major disadvantage is a slow response time, particularly during the cooling cycle. In addition, their life cycle decreases from millions of cycle at 0.5% strain to hundred cycles at 5% strain [3].

Kode and Cavusoglu employed a SMA actuator in their miniature hybrid actuator for a laparoscopic needle drive [20]. Their design consisted of a dc micro-motor utilized to provide the grasping motion and a SMA actuator to apply the gripping force. The actuator designed was 5.14 mm in diameter and 40 mm in length. The SMA actuator exerted a maximum force of 24 N. The hybrid actuator operated in two phases. In the first phase the dc motor closed the needle driver through a lead-screw and nut assembly, while in the second phase the gripping load was applied through the SMA actuator. The SMA actuator consisted of SMA wires, fixtures and a return spring, as depicted in Figure 2.2.6. The temperature of the wires reached approximately 80°C.

2.2.5 Pneumatic and Hydraulic Actuators

Pneumatic and hydraulic actuators exhibiting a high power to weight ratio could be a possible candidate for miniaturization.

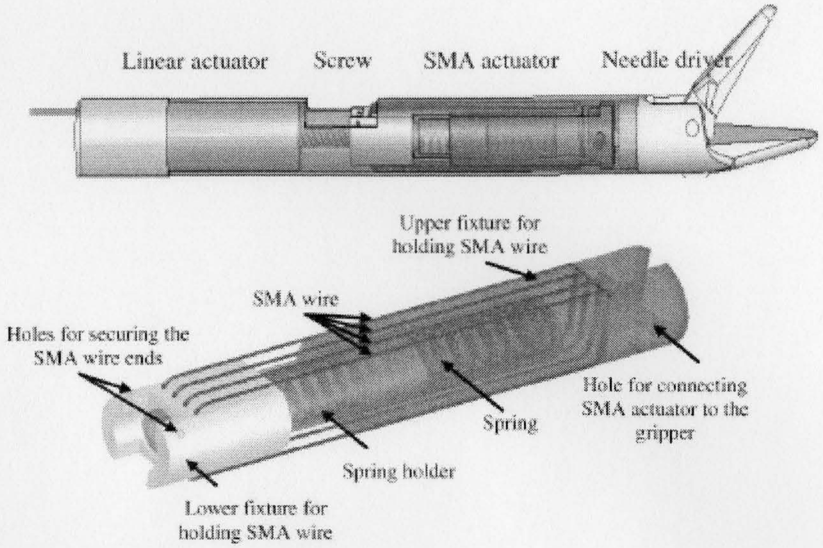

Figure 2.2.6: Hybrid actuator for minimally invasive surgery [20]

2.2.5.1 Pneumatic Muscle Actuators (PMAs)

These actuators are a special type of a pneumatic cylinder. The major difference between a PMA and a pneumatic cylinder is the change in the shape of the actuator in response to supply pressure changes.

Some of the distinctive features of these actuators include: simple structure, high power density (power to weight ratio), and a relatively frictionless mechanism. However, they suffer from a small range of active motion and are not commercially available in smaller sizes. They are also highly nonlinear in nature making them difficult to control.

PMAs are made of flexible reinforced closed membranes, with mechanical attachments at both ends that transfer force. As air is supplied or sucked out of the membrane, the actuator in inflated or squeezed. The radial expansion or contraction is associated with axial movement along the length of the actuator. The actuator behaviour can be given with the following rules [21]:

- A PMA shortens by increasing its enclosed volume;
- The actuator length will change against a constant load if pressure is changed;
- The actuator length will change at a constant pressure if the load is changed, and;
- Maximum contraction occurs at maximum enclosed volume, at which it develops no force.

PMAs exert a pulling force similar to that of a human muscle. In order to generate a bi-directional motion two opposing muscles must be attached in an antagonist configuration. The combination of pressures supplied into each antagonist PMA can be used to control the position of the load.

A variety of PMAs have been designed and fabricated. The most famous and widely used type is the braided muscle actuator (also known as BMA). Figure 2.2.7 shows the structure of this actuator. A BMA consists of an expandable elastic inner layer surrounded by a braided shell to protect the inner layer from over inflation and ruptures, and also convert the inflation of the elastic layer to axial contraction.

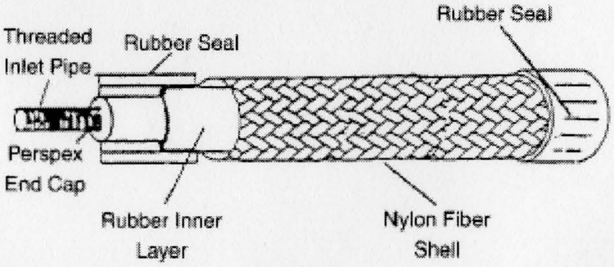

Figure 2.2.7: Braided muscle actuator design [22]

Lee and Shimoyama fabricated miniature BMAs which were employed as the actuators in an artificial hand [23]. The BMAs had a maximum diameter of 3.5 mm and were capable of generating a maximum contraction force of 7.6 N when pressurized to

0.35 MPa. The maximum contraction was reported to be 11% of the original length of the actuator.

Birch et al. developed a micro-robot resembling a cricket using small BMAs as the rear and front legs actuators [24]. The length of the actuators was between 22 to 28 mm, and the inner and outer diameters were 1.27 and 3.18 mm respectively when the actuator was deflated. The inner elastic layer was made by dipping a 1.19 mm wire in uncured latex. A wall thickness of 0.25-0.33 mm was achieved by varying the number of times the wire was dipped and time between dips. Forces and contraction data were not presented.

2.2.5.2 Multi-chamber pneumatic or hydraulic manipulators

Some research has focused on integrating more than one pneumatic or hydraulic actuator into a single manipulator to facilitate miniaturization, while providing more than one degree of freedom.

Suzumori, Iikura, and Tanaka developed a pneumatic (or hydraulic) multi-chamber manipulator, in which the pressure of each chamber was controlled through pressure control valves [25] (Figure 2.2.8). The circular direction reinforcement facilitated axial and bending movements giving three degrees of freedom. Applying equal pressures in all three chambers caused a pure extension movement, while different pressures in each chamber resulted bending movement about x or y axes of the actuator (pitch or yaw), totalling three DOF.

The actuators developed ranged from 1 mm to 20 mm in diameter and were implemented in robotic multi-degree of freedom fingers to manipulate objects. In an experiment they managed to screw a bolt using a four finger manipulator with speed of 0.25 turn/s and maximum torque of 0.01 Nm. The movements were detected using an LED attached to the tip of the finger and a position measuring instrument.

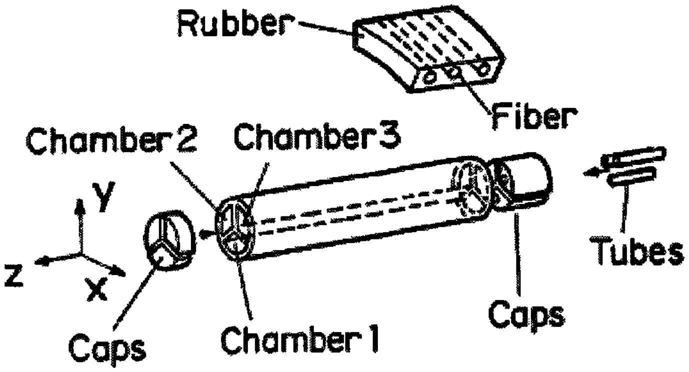

Figure 2.2.8: Structure of a multi-chamber actuator [25]

Peirs, Reynaerts, and Brussel conducted an interesting research project to achieve a miniature 3-DOF manipulator to be used in a self-propelling robotic endoscope [26]. Their extensive work consisted of the fabrication of a hydraulic, as well as an electric manipulator, each integrated with three separated drive modules linked through a 3-DOF Stewart platform. The hydraulic manipulator had an outer diameter of 12 mm and length of 30 mm containing three cylinders 3 mm in diameter, which theoretically could generate 7 N at 1 MPa. The elastic membrane covering the whole system also acted as a return spring reducing the real output force to about 3.5 N for each cylinder. Two O-rings, fixed to the pistons by small steel clamps, were utilized to seal the gap between the pistons and cylinders. The O-rings caused a static friction ranging from 0.4 to 0.9 N and a sliding friction of 0.3-0.4 N. The pistons were connected to piston rods through leaf springs, which served as flexible joints as depicted in Figure 2.2.9(a). The prototype had a maximum longitudinal stroke and rotation of 10 mm and 35° respectively.

To independently control three cylinders, four tubes are needed; three to supply pressure to each cylinder and one as a common return. The researchers used Teflon tubes with an external diameter of 1.6 mm. In order to reduce the number of tubes they integrated the valves into the manipulator, which increased the mechanical flexibility of the endoscope. Piezoelectric valve (Figure 2.2.9(b)) consisting of piezo stacks pushing a steel hemisphere over the inlet of the valve was developed. Two valves were used for each cylinder to control inlet and outlet to the cylinder. A solenoid valve was also fabricated and integrated in another prototype, showing superior performance in flow rate, leakage, and activation voltage. The problem with the solenoid valve was that it worked only up to a pressure of 200 kPa.

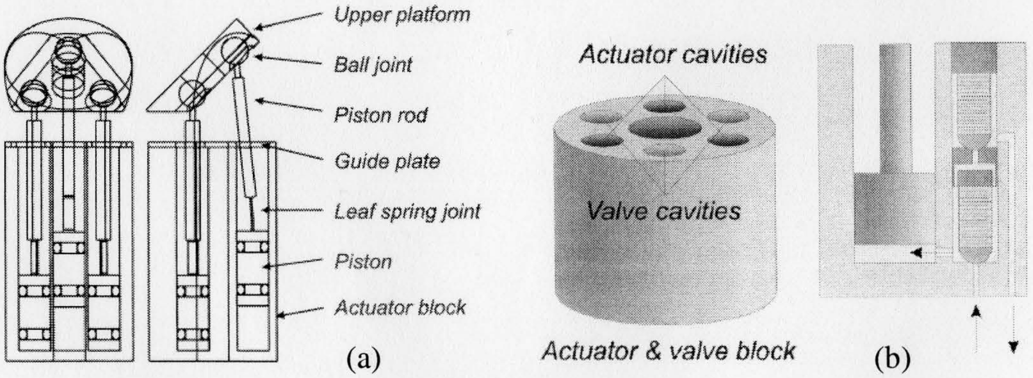

Figure 2.2.9: (a) Endoscope manipulator design, (b) Piezoelectric valve integration [26]

2.2.5.3 Vane Actuators

Vane actuators are rotary pneumatic or hydraulic actuators, where the pressure chambers are circumferentially divided by a blade called a vane (as compared to axial separation in cylinders by a piston). Commercial pneumatic vane actuators are available with a diameter of 29 mm and length of 46 mm, offering 19 Ncm output torque at 0.7 MPa supply pressure [27]. The vane actuators have the following advantages over the regular cylinders:

- Higher power to weight ratio due to increased exposed area to pressure;
- Less noise due to circular balanced rotation, instead of reciprocal linear motion;
- Transmission simplicity where rotary output is required, and;
- Greater ability to achieve higher torques where the cross section area of actuator is the limiting factor.

The major downside of these actuators is the considerable friction caused by a long sealing contact area. In practice, torque is often transferred through a flexible shaft coupling, which is another source of difficulty in modeling and controlling of systems containing vane actuators [28].

2.3 Position Control of Pneumatic and Hydraulic Systems

Pneumatic systems are widely used to actuate many industrial systems and machineries. Most of the applications employ adjustable mechanical stops as the end position control. Continuous motion control of pneumatic systems have been rarely used in industry, except for control systems working under low pressures (around 100 kPa) where the response time is not a crucial factor. Shearer conducted the first comprehensive study on a servo-pneumatic control system, consisting of a 4-way servo-valve and a double acting cylinder [29]. He derived the mathematical model governing a pneumatic servo-motor through nonlinear differential equations.

As an alternative, Shih and Tseng proposed system identification method to obtain the transfer function of the system [30]. They came up with 2nd, 3rd, and 4th order transfer functions. The reduced 2nd order model from the 3rd order model was the basis for their PID controller.

Rao and Bone presented a novel pneumatic position controlled system, which employed four 2-way proportional valves, instead of the traditional approach of using a single 4-way proportional valve [31]. The output of their experimental setup consisted of a cylinder with a bore of 9.5 mm moving a payload of 1.5 kg. They designed a nonlinear controller by the backstepping method. Their controller produced a tracking error of ±0.5 mm for a sine trajectory with an amplitude of 7.5mm with a frequency of 1 Hz.

Another alternative for proportional valves are on/off solenoid valves, which are much cheaper and less bulky, but generating smooth motion using these valves is more difficult. Varseveld and Bone developed a pulsewidth modulation (PWM) algorithm to successfully address this deficiency, generating satisfactory linear open-loop velocity response vs. PWM controller signal [32]. Two solenoid valves having a response time of 5 ms were activated with PWM signals. The system also included a 27 mm bore low friction double acting cylinder with 152 mm stroke connected to a horizontal linear slide. The system controller consisted of PID control, friction compensation using a simple coulomb friction model, and position feedforward. A bounded integral action element was also added to the control to reduce the effect of variation of stiction force along the piston stroke. Tracking error of less than 2 mm to a 64 mm s-curve trajectory was achieved. A maximum steady state error of 0.21 mm for step inputs from 0.11 mm to 64 mm was reported.

2.4 Low Pressure Water Hydraulic Actuators

Generally, two main types of controlled hydraulic drives are used in the industry, those being: pressure supply-resistance controls and flow supply-displacement controls [33]. A hydraulic motor or a cylinder could be used as the fluid supply source of the hydraulic drive system. Pressure supply-resistance control method employs a valve to control the hydraulic resistance of the system. The valve which could be a proportional valve or a control valve controls the pressure drop in the valve and pressure which is applied in the driven component. The energy dissipated through the pressure drop in the valve changes to the heat and raises the temperature of the working fluid. The more the throttling action in the valve, the more loss happens in the system, leading a higher inefficiency of the hydraulic drive system. On the other hand, in the flow supply-displacement control, the driven component is directly controlled through adjustment of the swash plate of an in-line axial piston pump. The efficiency of this method is much higher and usually used in systems with a power above 10 kW [33].

Water as the working fluid in a hydraulic system is attracting the attention of more researchers in recent years. This new technology lies between conventional hydraulics using oil as the working fluid and pneumatics using air as the power transmission media. This technology is also called low-pressure water hydraulics (LPWH), which emphasizes on the low pressure of the system (10-40 bar), as compared to high pressure involved in conventional hydraulics. These systems are low cost and environment friendly similar to pneumatic systems, while they have enough rigidity and controllability that make them a proper alternative for the hydraulic systems where the system does not require very big forces. On the other hand, friction is an important factor in LPWH systems as the viscosity of water as the working fluid is much less than hydraulic oils. This factor is more dominant as the working pressure (and generated force) is much less than traditional hydraulic systems.

Danfoss, a Danish manufacturer of hydraulic systems, introduced its new range of water hydraulic components using tap water as the hydraulic fluid in 1994 [34]. These products developed under trade name of Nessie are commercially available in a wide range of products such as pumps, valves, and cylinders. The engineers in Danfoss had been facing critical issues related to water as the working fluid: cavitations, corrosion, and lubrication. By using innovative component designs and employing non-traditional materials they overcame those problems. Their water hydraulic systems are capable of working in pressures up to 16 MPa. However, they do not manufacture components small enough to be used in miniature applications.

Cho, Linjama, Sairiala, Koskinen, and Vilenius developed a position control algorithm for a LPWH system. Their system included a cylinder and horizontal payload, controlled using a proportional valve [35]. They modeled the plant by separating the nonlinear friction characteristic of the system and representing the rest by a second-order linear transfer function. Finally, a controller consisting of feedforward friction compensation, and sliding mode action was designed. At a test pressure of 3 MPa and over a range of motion of 100 mm, the maximum steady state and tracking errors of the experimental setup with a payload of 200 kg were reported to be 0.23 and 5 mm respectively.

Sindrey and Bone conducted research on controlling a water hydraulic system using off-the-shelf cylinders and solenoid valves [36], [37]. They compared three control techniques: linear PVA, model-based feedforward plus PVA, and sliding mode coupled with PVA and feedforward. The experimental setup consisted of two miniature cylinders, each with a bore diameter of 4 mm and a stroke of 20 mm. Pressurized water supply was provided by using an air-over-water system. To overcome the problem of unavailability of miniature proportional valves, which could appropriately control the small flow rate of the system, two 2/2 on/off solenoid valves were arranged to simulate the behaviour of a proportional valve. A significant improvement in tracking errors was achieved (from 0.25 mm to 0.14 mm for a sinusoidal trajectory with an amplitude of 5 mm at a frequency of 0.5 Hz) when sliding mode and feedforward controllers are added to the PVA controller. The maximum steady-state error was reported to be as low as ±0.07 mm.

2.5 Reducing the Detrimental Effect of Friction on Pneumatic and Hydraulic Actuators

A servo-mechanism can suffer from chattering about a desired set point when the system dynamics include a discontinuity in the friction. Sudden drops from static friction to Coulomb friction cause a sudden release of stored elastic energy, which leads to sudden movement in the output. The sudden movement together with the control inputs could force the output to enter into a stick-slip oscillation.

One of the solutions to reduce this effect is add a high frequency signal to the input. This signal is also referred to as dither. Although the effectiveness of dither in reducing the stick-slip oscillation was often practically observed, there are few analytical works on this subject [38], [39]. It is believed that dither keeps the frictional surfaces in a constant motion and as a result stick-slip cannot develop.

Michaux, Ferri, and Cunefare studied the effect of dither on a single DOF model with two friction models: stribeck friction law and decreasing friction law [39]. In their simulations, when a dither with a frequency of about ten times the natural frequency of the system was applied the stick-slip induced oscillation was decreased to 5% of undeterred response.

While many control algorithms have been studied to reduce the effect of stick-slip friction, only a few researchers have designed actuators that attempt to avoid it altogether. A commercial low friction cylinder is available which employs a precision fit graphite piston that slides without lubrication inside a Pyrex glass cylinder [40]. No rubber or plastic seals are used with this type of actuator; therefore no wear occurs over time. The cylinder responds to a pressure difference as little as 0.0015 MPa and is not affected by a wide range of temperature change. The piston friction is just 1-2% of load. Unfortunately, the smallest bore size available is 9 mm.

In an attempt to make small hydraulic cylinders having low friction, De Volder et al. fabricated a miniature hydraulic microactuator with a bore diameter of only 1 mm and length of 13 mm [41]. The cylinder was capable of generating a force density of 0.23 N/mm^2. The main difficulties encountered in development of such a small cylinder were those related to tolerances and assembly, as well as the seal which is the main source of friction. The researchers investigated the idea that leakage between a rod and orifice can be kept very low, if a small clearance between two components is kept over a certain length. Using μEDM technology, they managed to reach a clearance of 5 μm between the piston and the cylinder. The other challenge was the alignment of cylinder to its rod, to which a radial spring suspension was chosen as a solution. In addition, two elastic hinges were added to the piston rod to compensate for misalignment between piston-cylinder and piston rod-seal orifice sliding joints. A force of more than 0.4 N at 550 kPa was measured using oil as the working fluid, while with water a reduction of 25% was recorded (Figure 2.5.1). The leakage was also measured and was found to be 2.9 mm^3/h per 100 kPa.

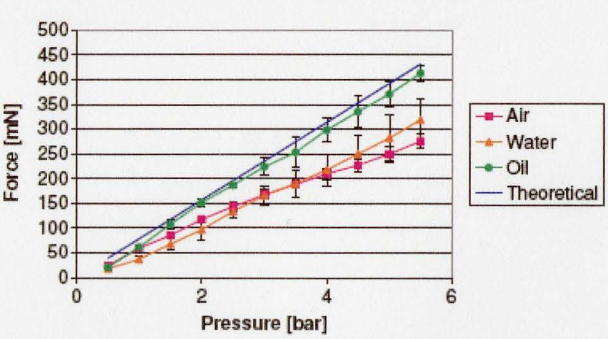

Figure 2.5.1: Pushing force vs. pressure for different working fluids [41]

The leakage is the limiting factor in cylinders with a clearance seal. The supply pressure could not be raised high, as the leakage increases proportional to pressure. Volder, Ceyssens, Reynaerts, and Puers developed a PDMS lipseal for pneumatic and hydraulic actuators [42]. The idea behind their design was to combine the low friction characteristics of a clearance seal at low pressures, with the superior sealing behaviour of U-seals at high pressures. The lipseal was designed such that at lower pressures the flexible lip of the seal was not deformed holding certain clearance between moving parts. As the pressure rose above a certain value (100 kPa in their research), the seal lips expanded and sealed the space between the moving parts. The operation principle of this seal is shown in Figure 2.5.2. The friction in this case increased, but the force generated increased as well. Thanks to the lipseal they could raise the supply pressure up to 1.6 MPa and generate forces of 1.2N, with a cylinder of 1 mm in bore size.

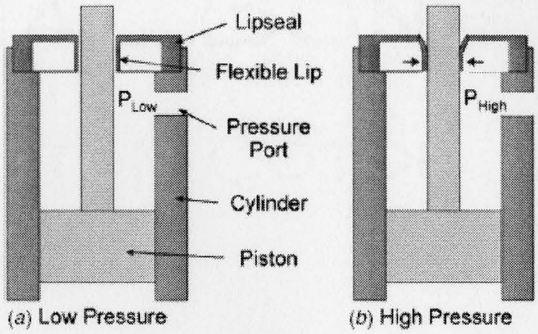

Figure 2.5.2: Schematic of lipseal operating principle [42]

Owen, Croft, and McFarlane proposed a technique to avoid the stick-slip friction in a hydraulic cylinder. Their suggested method involved rotation of the piston while the piston moved along the axial direction [43]. They used the stribeck friction law as their friction model for simulation. Their simulation results showed that by rotating the piston the discontinuity of friction force at very low velocities (near zero) was suppressed.

2.6 Summary

While most of the controlled motion applications rely on traditional electric, pneumatic and hydraulic technologies, new applications involving miniaturization require different approaches. Many researchers have focused on emerging technologies among which electrostatic, piezoelectric and shape memory alloys are better candidates for miniature actuators. All emerging actuators demonstrate strengths and weaknesses, which makes them a suitable candidate for specific applications.

Another solution may be the use of traditional actuators applied with different approaches. Special electromagnetic actuators have been developed in miniature sizes. Pneumatic muscle actuators resembling human muscles comprise high power density and flexibility. Also different approaches of handling pneumatic and hydraulic power sources have been considered. Multi-chamber and hybrid pneumatic (or hydraulic) manipulators increase their adaptability for miniature applications.

Low pressure water hydraulic is a relatively new method which combines the benefits of low pressure and the cleanliness of pneumatic systems, with the rigidity and controllability of hydraulic systems. Hydraulic resistance against the supply pressure may be controlled through proportional valves. Researchers have implemented water hydraulic systems utilizing on/off solenoid valves excited by PWM signals to mimic a proportional valve.

Friction as one of the key determinants of mechanical system performance has been widely studied. To improve performance, different methods and approaches have been studied including: implementing friction compensators within the controller, adding high frequency excitation (dither signal) to the control signal, friction reduction through modification of actuator sealing, and methods to avoid friction discontinuities.

CHAPTER 3

JOINT MECHANISM AND SYSTEM DESIGN

3.1 Introduction

This chapter commences with a critical review of the previous work undertaken on the design and control of a miniature rotary actuator in our laboratory. Next, an examination of alternative designs and methods for improving the performance of the system are described. Finally, the design of the replacement apparatus is presented.

3.2 Studies to Improve Performance of Previous Apparatus

The objectives of the previous work on the design and control of a miniature rotary actuator conducted by Sindrey were studied [36]. The main objectives were to build a miniature rotary joint, with a diameter of less than 15 mm, having a rotational range of 180° and being capable of producing a maximum output torque of 20 mNm. The system structure of this work is depicted in Figure 3.2.1. The system included a rotary joint, utilizing two single acting cylinders, with a 4 mm bore diameter pushing two racks against a pinion. The output rotation was indirectly measured by recording displacement of one of the racks by a hall-effect sensor. The hall effect-sensor assembled close to a magnet glued to one of the racks generated a nonlinear voltage proportional to the displacement of the rack. The pressurized water was supplied to the cylinders by way of a 40 mm bore cylinder. Air, with a constant pressure, was supplied on one side of piston, thereby pressurizing the water stored in the other side. The water flow to the miniature cylinders was controlled through four on/off solenoid valves. Each cylinder was connected to two valves, one to supply water into the cylinder and the other to discharge water from it. To move the rotary joint in CW direction (refer to Figure 3.2.1), valves V1 and V4 were set to the on state, while V2 and V3 were turned off.

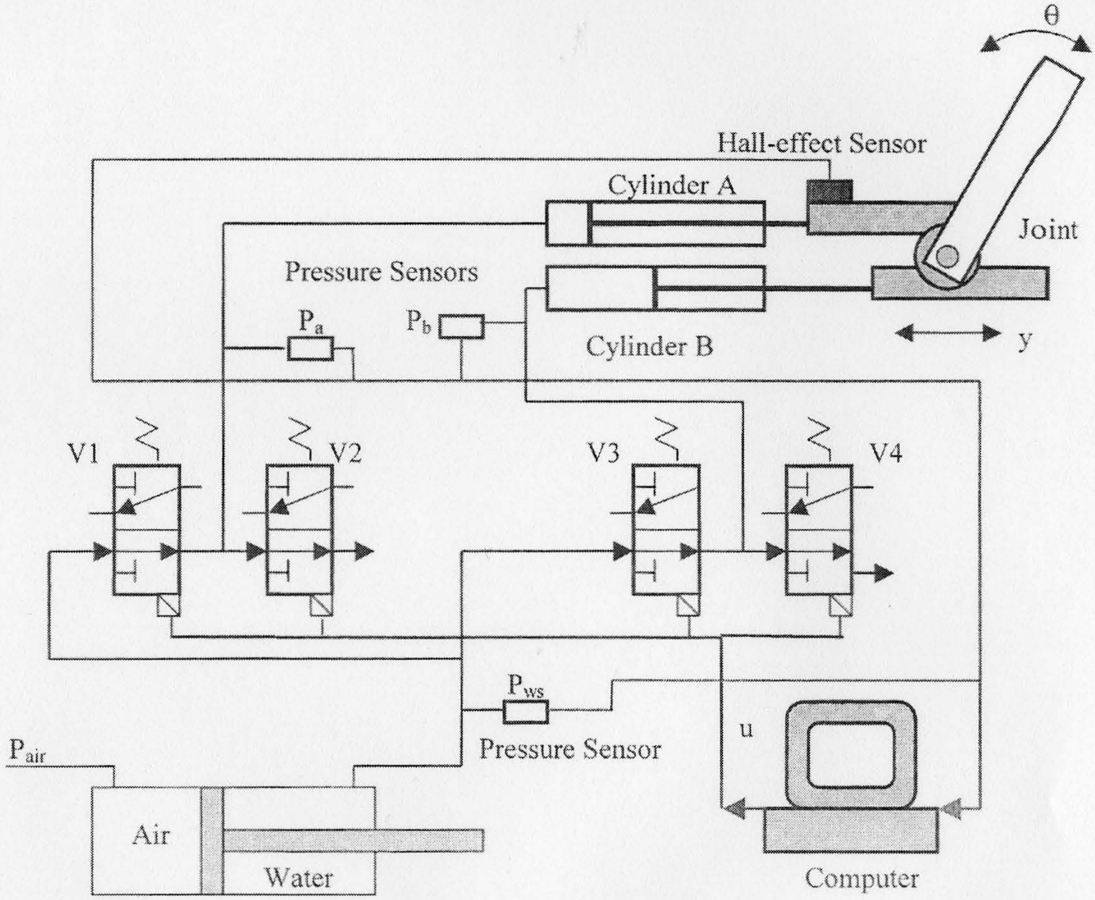

Figure 3.2.1: Hydraulic servo positioning system hardware developed by Sindrey [36]

The following elements in the existing system were studied in an effort to improve the performance of the system:

- **Actuators:** Two alternatives for miniature cylinders are evaluated, including vane actuators and braided muscle actuators.

- **Rotary joint:** The rack and pinion rotary joint suffers from position dependant friction due to small number of teeth, and from backlash. Two rotary joint concepts are studied, including a six-bar linkages mechanism and a slider-pulley mechanism.
- **Output sensor:** A magnetic rotary encoder is used to directly measure the output of the rotary joint.
- **Control and water supply:** A new idea based on a cylinder water pump is introduced acting as both the controller hardware and water supply pump.

3.3 Rotary Vane Actuator

Vane actuators are the rotary hydraulic actuators that have the greatest potential for miniaturization. The differential pressure between two (or four) chambers rotates the output shaft. Typically, there are two kinds of vane actuators (Figure 3.3.1): single vane, and double vane. There are numerous advantages with these actuators, including:

- Vane actuators have superior power performance, as compared to a linear cylinder of similar size. The reason is that the area exposed to the pressure difference in a vane actuator is more than that in a cylinder of equal size.

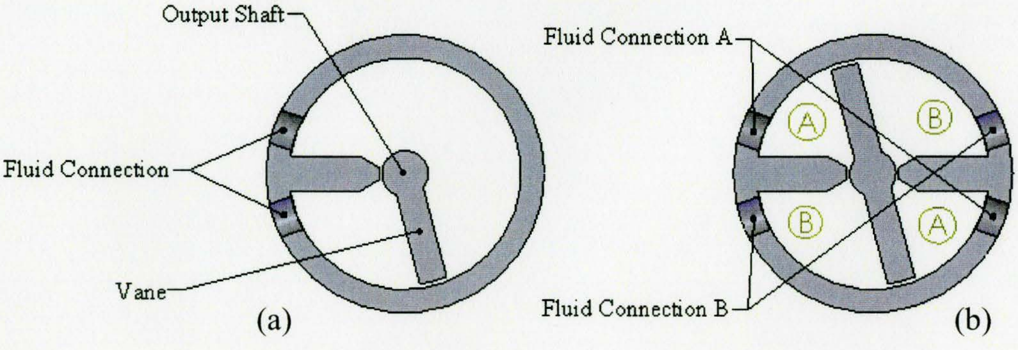

Figure 3.3.1: Rotary vane actuators (a) single vane, and (b) double vane

- The output is directly rotational, which eliminates the necessity for a mechanism to transform a linear motion to an output rotation, making the overall system smaller and simpler.
- By using these actuators, a double acting motion (rotation in two directions) is easily achieved, while with cylinders the tubing limitation forces us to use two single acting cylinders in an antagonistic configuration. The tubing problem with double acting cylinders is illustrated in Figure 3.3.2. As such, the joint mechanism will be simpler and more efficient.

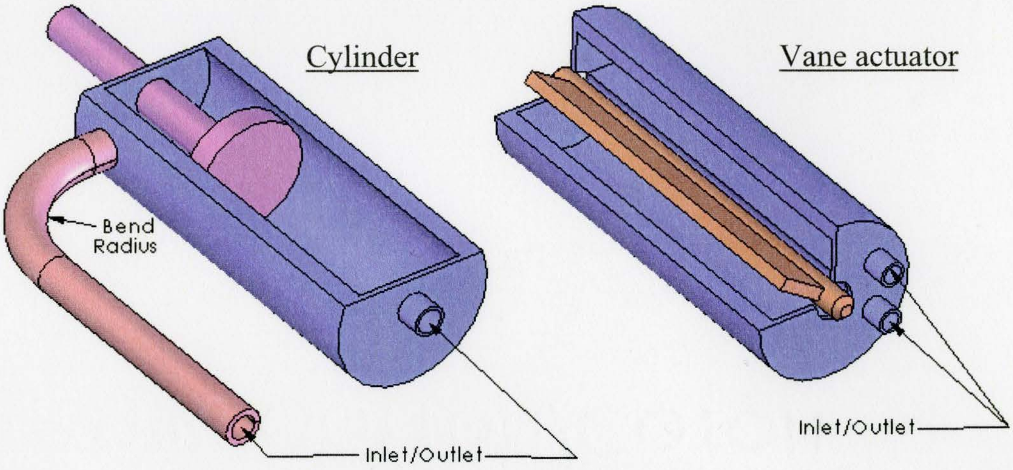

Figure 3.3.2: The bend radius limits use of double acting cylinders

To understand the power-to-weight ratio advantage of rotary vane actuators, the area exposed to pressure is calculated as compared to a rodless cylinder and a double vane actuator having the same overall dimensions as shown in Figure 3.3.3.

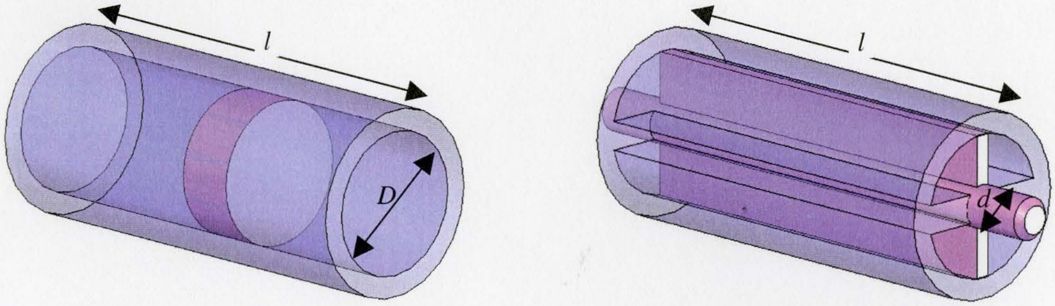

Figure 3.3.3: cylinder vs. double vane actuator

The area exposed to pressurized fluid in the cylinder is the area of the piston, while this area in the case of vane actuator is the total area of the vanes. For rodless cylinders the exposed area equates to:

$$if\begin{cases} D = 10mm \\ l = 50mm \end{cases} \Rightarrow A = \frac{\pi D^2}{4} = 78.5mm^2 \tag{3.3.1}$$

While for double vane actuator this value is:

$$if\begin{cases} d = 2mm \\ D = 10mm \Rightarrow A = (D-d)\times l = 400mm^2 \\ l = 50mm \end{cases} \tag{3.3.2}$$

Comparing (3.3.1) and (3.3.2) one can see that the exposed area for a vane actuator (and consequently force for the same pressure difference) is more than 5 times that of a cylinder. Further, the equations show that in the case of cross sectional size limitations, the exposed area could still be increased by increasing the length of the actuator, while in the case of cylinder this area is fixed.

However, there are disadvantages with dual vane actuators. The range of rotation is limited to less than 110°. Also, the length of the seal in a vane actuator is far more than that for a cylinder of a similar size, thereby increasing the contact length and accordingly the friction between vane and actuator interior body. For the given dimensions on (3.3.1) and (3.3.2), seal lengths will be 31.4 mm for cylinder, while this length will be more than 3.5 times (116 mm) for double vane actuators. This dramatically increases the friction, which is a very important factor in the performance and control of the actuator. The seals between the output shaft and the actuator body are also another issue, which could be avoided by using a magnetic coupling.

To increase the range of rotation and eliminate sealing problems in the area of the output shaft, a modified single vane actuator was designed. The external size of actuator is 13 x 15 x 18 mm and the range of rotation 140° (Figure 3.3.4).

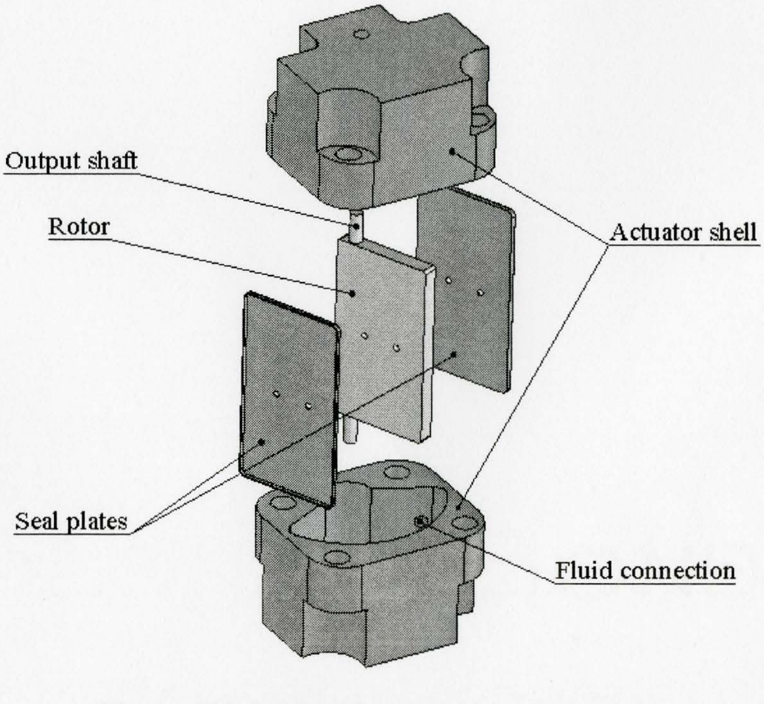

Figure 3.3.4: Modified single vane actuator

The rotor carries two seal plates, which separate the two pressurized fluid chambers. The seal plates have lipseals all around, which are forced to the shell's interior surface as the pressure increases, thereby reducing the leakage between the two chambers. The area exposed to pressurized fluid is about 105 mm^2, which could generate a nominal torque of about 110 mNm (ignoring torque lost due to friction) at a pressure difference of 0.3 MPa between the two chambers. In this design, the contact length is about 48.5 mm.

This modified single vane actuator is simple, small in design, and capable of generating sufficient torque on the output shaft, with a range of rotation more than that of a double vane actuator. On the other hand, seals are still a major issue in this design. The seals should be manufactured in a way to properly stop any leakage between the chambers, while having enough tolerance with the interior surface of shells to minimize friction. Precision machining and assembling is another requirement for the successful implementation of this actuator in the miniature scale.

3.4 Braided Muscle Actuator (BMA)

The structure of a braided muscle actuator is as shown in Figure 2.2.7 and consists of a inflatable membrane protected by a flexible shield. The BMAs are good candidates for miniaturization as they can generate large forces and have a high power-to-weight ratio. Unlike conventional cylinders, they do not involve moving seals which are a major source of friction.

A computer simulation was generated to study the behaviour of these actuators. Figure 3.4.1 compares the isobaric force-displacement diagrams for conventional cylinder (dashdot lines) and BMA (solid lines) of comparable size. The friction between piston and cylinder in a conventional cylinder and the friction between a membrane and a protective shield are not included in this simulation. The cylinder having a bore diameter of 4 mm and stroke of 20 mm, has an outside diameter of 5 mm and overall length of 60 mm. The simulated BMA has a maximum working diameter of 5 mm, initial overall length of 60 mm, and a membrane thickness of 0.25 mm. The BMA generates a higher force as compared to the cylinder, when displacement (contraction) is less than 8 mm. Another property of BMAs is that these actuators demonstrate a higher level of compliance compared with cylinders, due to the dependency of force on the state of inflation.

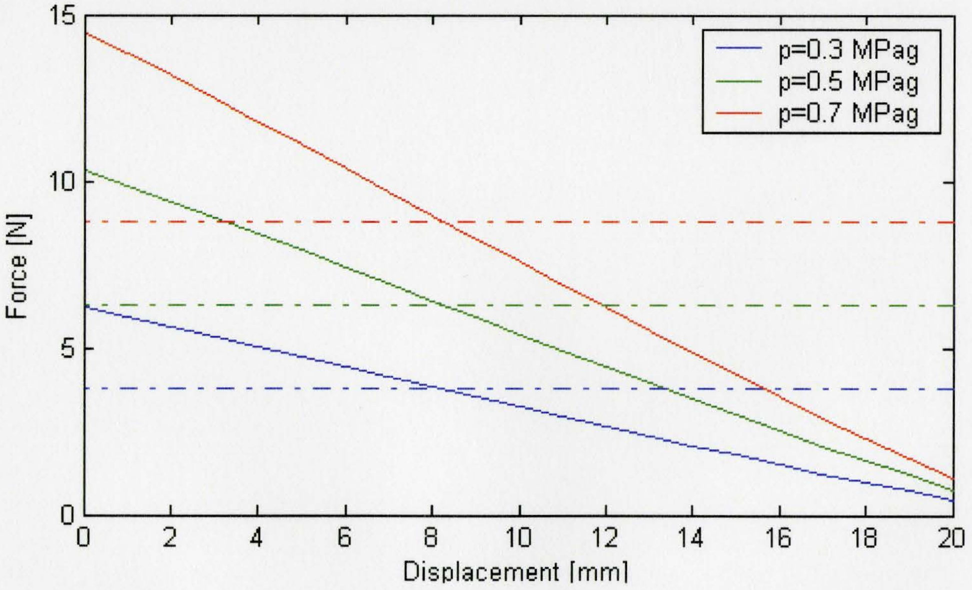

Figure 3.4.1: Force-displacement graphs for BMA (solid) and cylinder (dashdot)

In practice, the range of active motion for BMAs is more limited when compared to a conventional cylinder. Also, comprehensive modeling and subsequently model-based control of a BMA is more difficult. The performance of a BMA highly depends on the membrane and protective shell material, which is particularly critical in smaller configurations. Another practical challenge is the sealing of the membrane and end caps.

Considering the advantages and disadvantages of the actuators studied in this section, conventional miniature cylinders still remain the best choice of actuators to be used in rotary joints for this research.

3.5 Six-Bar Linkages Rotary Joint

A six-bar rotary output mechanism is studied as a potential alternative for the rack and pinion rotary joint. The mechanism depicted in Figure 3.5.1 consisted of 6 links and 7 joints (2 slider and 5 pins). The Gruebler's equation is used to find the degrees of freedom for a planar linkages mechanism with n links and j one-degree-of-freedom joints:

$$m = 3(n-1) - 2j \tag{3.5.1}$$

where m is the mechanism's mobility or degrees of freedom. The mobility of this mechanism using equation 3.5.1 will be one [44].

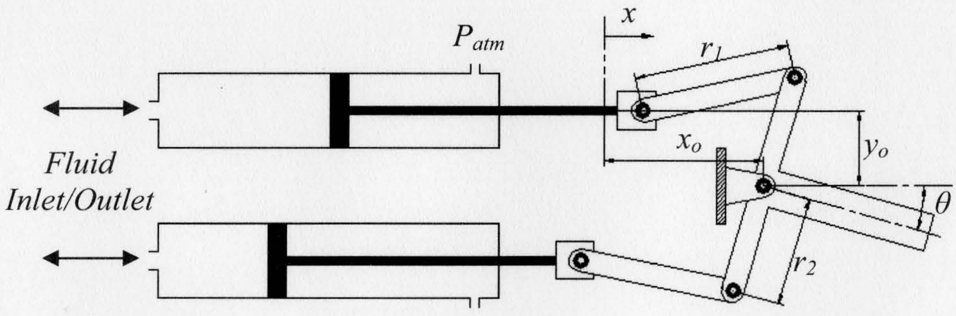

Figure 3.5.1: Six-bar rotary output mechanism

The two cylinders are assembled in an antagonistic configuration and the desired output angle θ is achieved by directing the fluid flow into or out of the two cylinders. A prototype was designed and built as shown in Figure 3.5.2 with dimensions of r_1=9.7 mm, r_2=6.2 mm, y_0=4.0 mm, and x_0=9.45 mm.

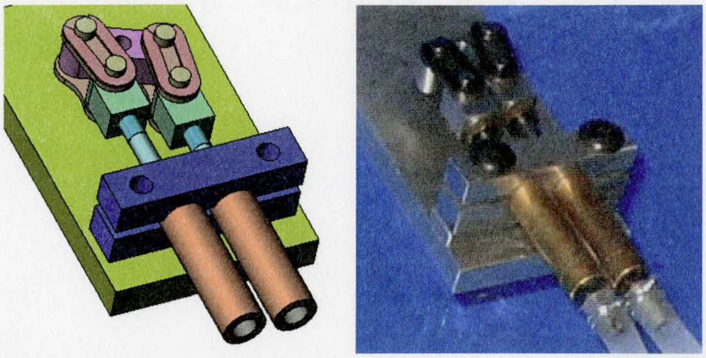

Figure 3.5.2: Design (left) and manufactured (right) prototype of a six-bar rotary output mechanism

The kinematic equation relating input x and output θ, involves trigonometric functions which makes it highly nonlinear. Also, the range of efficient pressure angle on the crank is limited. Although the smooth motion of the prototype joint is very promising, the close to linear range of motion with proper pressure angle on output crank is only ±40° (Figure 3.5.3).

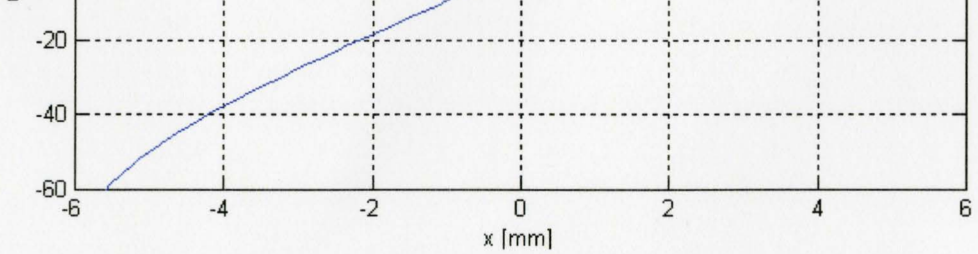

Figure 3.5.3: Joint output angle vs. piston displacement

3.6 Slider-Pulley Rotary Joint

The slider-pulley mechanism shown in Figure 3.6.1 consisted of a pulley, two sliders and a low stretch Nylon string. The cylinders push the sliders, which in turn pull the string. The string is wrapped around the pulley 2.5 turns to increase the friction between the string and pulley. The friction between the pulley and string is very important in generating the proper output torque without slippage. The belt friction formula could be employed to relate the tensions in string and the friction between the pulley and string.

$$\frac{T_2}{T_1} = e^{\mu_s \beta} \tag{3.6.1}$$

T_2 represents the tension on that part of the string which pulls, while T_1 is the tension on resistant side of string. The static friction coefficient represented by μ_s is used when the string is about to slip. The contact angle β is expressed in radians. Therefore, the maximum torque (M_{max}) that can be transferred by pulley before slippage occurs between the pulley with a pitch radius of r_p and string is:

$$M_{\max} = (T_2 - T_1) \times r_p = T_1 \times (e^{\mu_s \beta} - 1) \times r_p \tag{3.6.2}$$

Considering the maximum required torque of 20 mNm, the pitch radius of a sample pulley of 3.41 mm, string wrapped 2.5 turns around pulley, and assuming μ_s to be 0.22, we can estimate the minimum T_1 to transfer torque without slippage.

$$\begin{gathered} \beta = 2.5 \times (2\pi) = 15.7 rad \\ T_1 = \frac{20}{3.41 \times (e^{0.22 \times 15.7} - 1)} = 0.19N \end{gathered} \tag{3.6.3}$$

In practice the frictions on the slider and piston and also the positive pressure in the cylinders makes T_I>> 0.3 N.

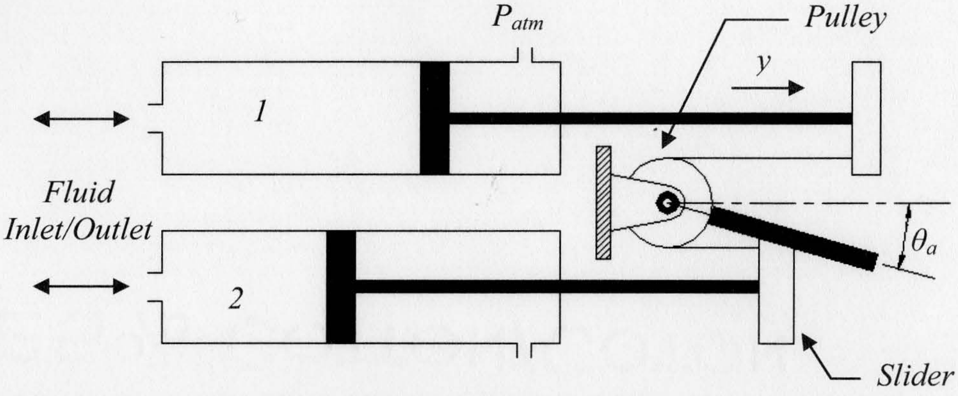

Figure 3.6.1: Slider-pulley rotary joint

Two prototypes of this rotary joint were made. Both prototypes have a pulley with a pitch diameter of 6.82 mm. The relation between y and θ_a (Figure 3.6.1) is given by:

$$\theta_a = \left(\frac{360^\circ}{6.82\times\pi}\right)y = 16.8y \tag{3.6.4}$$

The first prototype shown in Figure 3.6.2 has an overall dimension of (L x W x H) 80 x 12.5 x 13 mm. The brass slider blocks slide over steel machined shafts with a diameter of 4 mm. The critical element in this design is the precision between the hole in the slider block and the shaft. If the tolerance is too tight then friction rises. Also, a loose tolerance can cause a biting effect to happen between the shaft and block when the direction of movement changes. The wear in the brass slider block increases the tolerance and biting effect with the lapse of time.

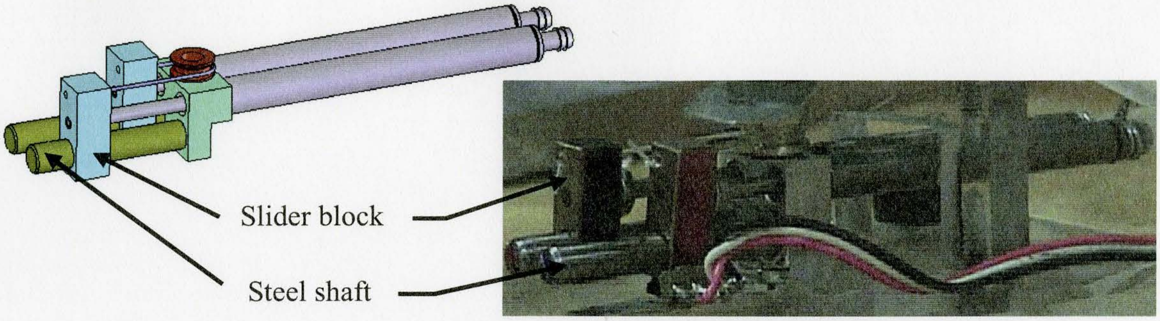

Figure 3.6.2: First prototype of slider-pulley rotary joint

The second prototype (Figure 3.6.3) was made to address this problem, using aluminium sliders with Polyacetal oil free bushings. The available bushings for 4 mm shafts have an external diameter of 6 mm, which significantly increases the size slider blocks and as a result the overall size of the joint (80 x 16 x 18 mm).

3.7 Position Sensors

In order to measure the angular output of the rotary joint a contactless magnetic rotary encoder is used, which is assembled above the centre of the pulley. A two-pole disk magnet is glued into a shoulder in the center of the pulley. The encoder has a 10 bit digital output providing a resolution of 1024 pulse/revolution or 0.35°/rev. No noise and nonlinearity is involved with the encoder and further the output is directly measured. Although this encoder is not a proper choice for miniaturization purposes, to increase the precision of the experiments and to study the performance of other elements of the system, this encoder is employed as the output measurement element.

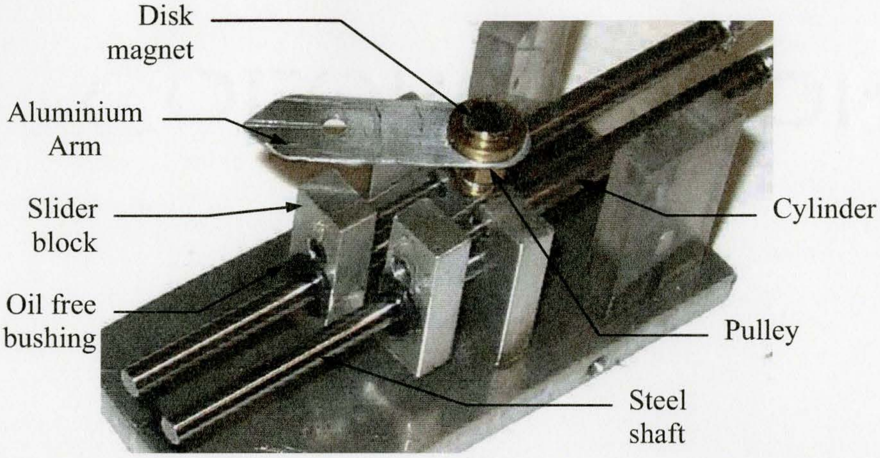

Figure 3.6.3: Second prototype of slider-pulley rotary joint

3.8 Motor-Cylinder Pump

Very few studies have been conducted in the field of low pressure water hydraulics and all of them have used valves (proportional or on/off) to control the hydraulic resistance against pressure supply and to control the position of the actuator. The throttling action in valves leads to losses in the form of heat in the working fluid and a reduction to the efficiency of the system. Proportional valves for small flow rates are not commercially available and small on/off valves are more difficult to control and vulnerable to chatter when controlled by the PWM method.

Another method in controlling hydraulic drives is to directly control the amount of fluid supplied into the actuator. In industrial applications this is done through controlling the swash plate of an in-line-axial piston pump. This method has higher efficiency when compared to the previously mentioned method, as no loss is induced by restricting working fluid flow. In this project, a novel system is proposed based on this method.

The control pump consists of a servo motor, which precisely controls the position of a linear guide through a lead screw. The linear guide is attached to a pair of small driving cylinders, which deliver the required amount of water to the driven cylinders on the rotary joint. This pump also acts as the water supply source to the joint cylinders.

Two pumps were fabricated. The first one consists of a lead screw with a lead of 1 mm/rev driving a bulky linear guide and pusher plate (Figure 3.8.1). The moving parts had a mass of 500 g in total. The pusher plate drives two cylinders with a bore of 4 mm in opposite fashion, when one cylinder is pushed the other one is pulled. The relation between the volume of water pumped and pump motor angle is (note that the lead screw is a ball screw type so the backlash may be neglected):

$$\frac{\Delta V}{\Delta\theta}=\left(\frac{\pi\times 4^{2}}{4}\right)/360^{\circ}=0.03491\,{}^{mm^{3}}\!/_{\deg} \tag{3.8.1}$$

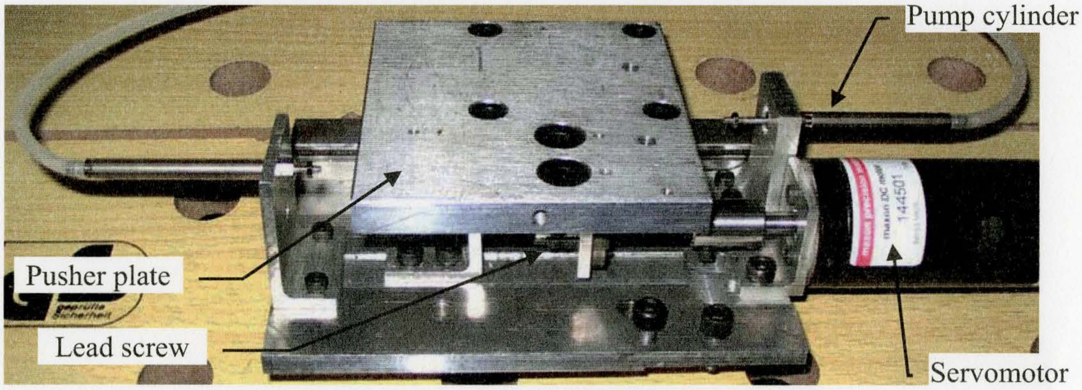

Figure 3.8.1: First prototype of motor-cylinder pump

In the second pump (Figure 3.8.2) the bulky linear guide and plate is replaced with a much lighter setup weighing 50 g. The pump cylinders are also replaced with another pair having a bore diameter of 6.35 mm. The volume of water pumped in this pump is more than 2.5 times that of the previous pump for the same pump motor rotation.

$$\frac{\Delta V}{\Delta\theta}=\left(\frac{\pi\times 6.35^{2}}{4}\right)/360^{\circ}=0.08797\,{}^{mm^{3}}\!/_{\deg} \tag{3.8.2}$$

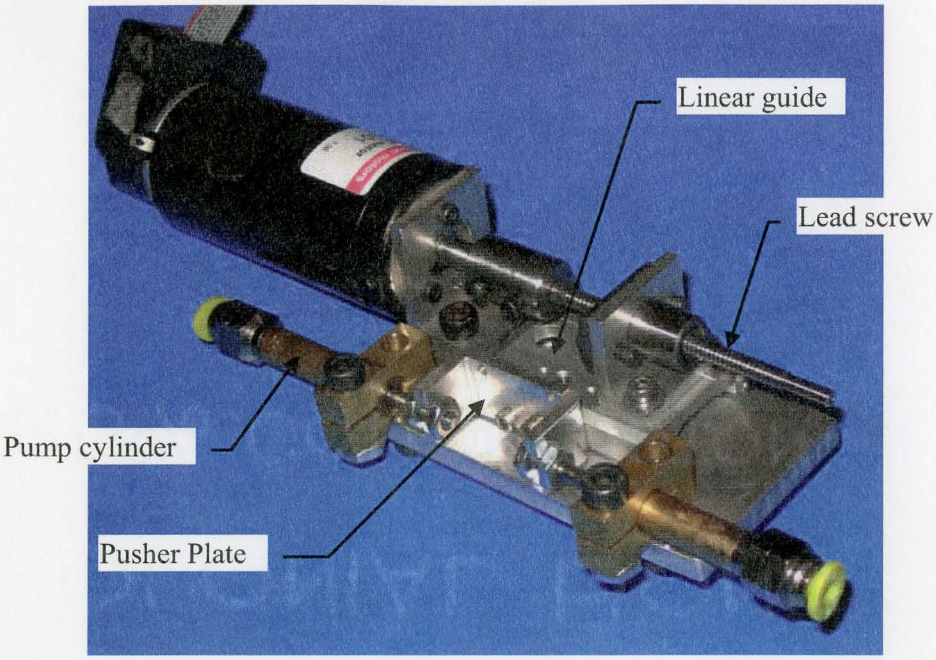

Figure 3.8.2: Second prototype of motor-cylinder pump

3.9 The Final Apparatus

The final apparatus includes a motor-cylinder pump as the controller mechanism and the water supply source, connecting tubes, slider-pulley rotary joint, and a preload mechanism (Figure 3.9.1). The setup is a closed-circuit system, meaning the water is not supplied in or drained out of the system during normal operation.

This system is analogous to a belt power transmission system (Figure 3.9.2). In a belt system, a drive pulley transfers the power to a driven pulley through a stretched belt. A tensioner maintains the tension in the belt. The tensioner is an important element of a belt-power transmission system in order to guarantee the proper torque transmission without any slippage between the belt and pulley. It also reduces the vibration issues by increasing the stiffness of the belt. In our closed-circuit system these elements are replaced by:

- Driver pulley → Pump mechanism
- Driven pulley → Output rotary joint
- Belt → Water and tubing
- Tensioner → Preload mechanism

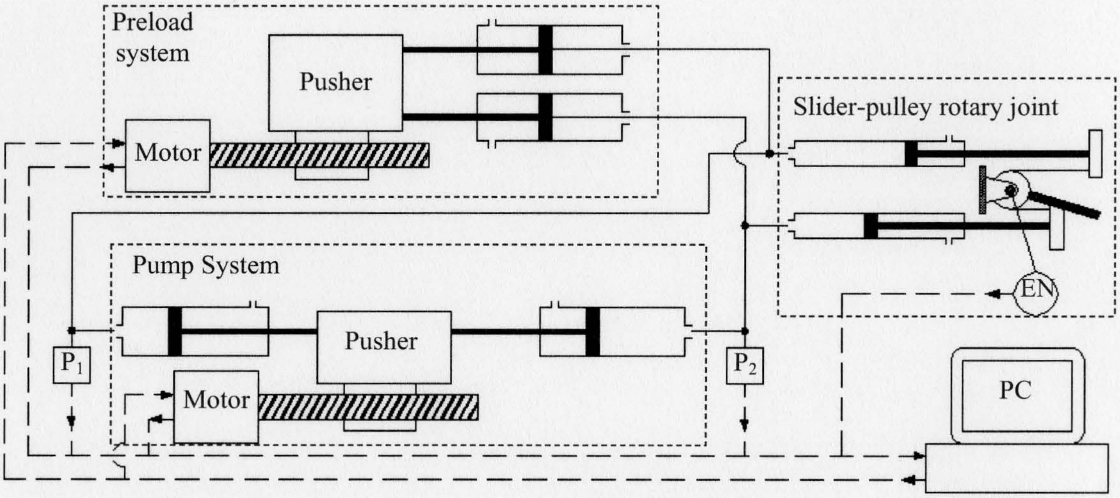

Figure 3.9.1: System hardware layout

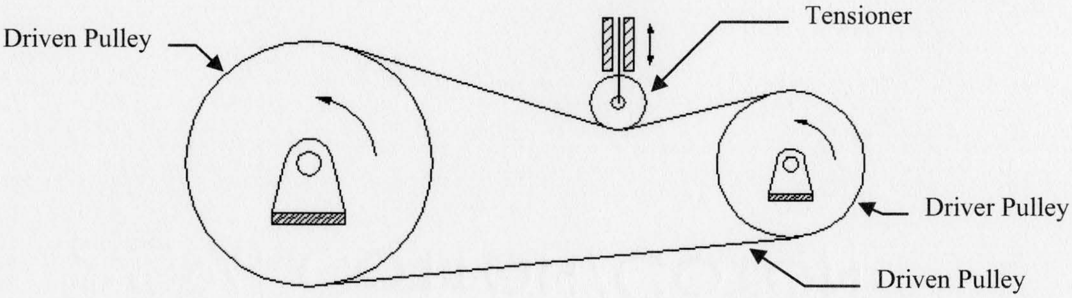

Figure 3.9.2: Belt power transmision system

The preload mechanism has the same structure as the pump except the cylinders act in the same direction. The preload mechanism is an important part of the mechanism having many functions:

- Providing a positive pressure to reduce the air flow inside the closed-circuit;
- Increasing the stiffness of the system, and;
- Acting as a reservoir to compensate for water leakage.

The system will be controlled by a program written in C and run in LabWindows environment. The program will communicate with the motors, encoders, and pressure sensors through National Instruments DAQmx I/O boards. A sampling rate of 1000 Hz will be used.

The pressure in each line is transferred to the computer through a pressure sensor (P_1 and P_2 in Figure 3.9.1) having a maximum range of 100 psig. The measured pressure is used to regulate the initial pressure in the system. Figure 3.9.3 shows the entire apparatus including pump and preload systems, rotary joint, hydraulic lines, pressure sensors, and rotary encoder.

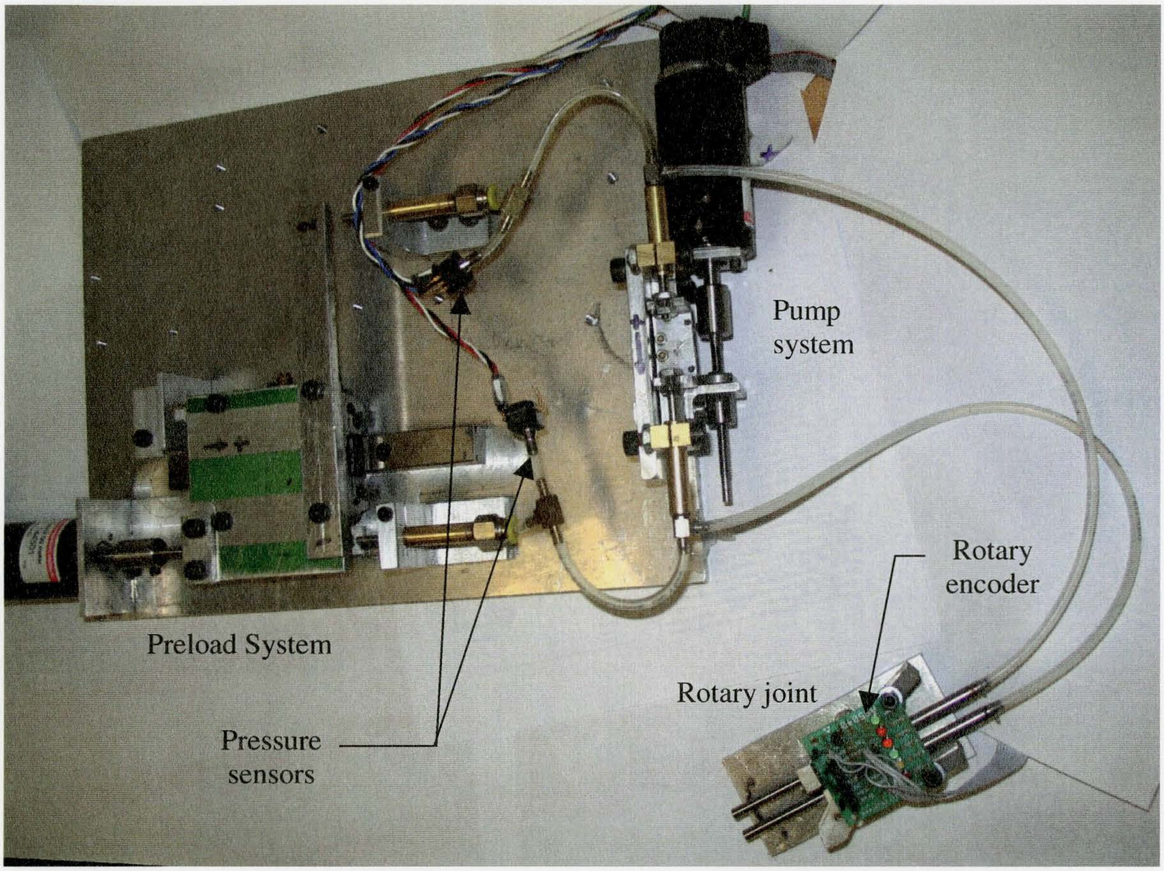

Figure 3.9.3: The entire apparatus

CHAPTER 4

SYSTEM MODELING

4.1 Introduction

There are two main advantages to performing a simulation. First, simulations save in time and expenses. Second, a simulation can provide detailed information about internal parameters that are not experimentally easy to measure and can be used in studying behaviour of the system. To perform a simulation, the system should mathematically be modelled. Modelling also is the core requirement of model based controllers.

In this chapter, the system is first divided into three main subsystems. Then the most important and also the negligible parameters in each subsystem are identified and discussed. The dynamics of the subsystems and the relationship between their inputs and outputs are mathematically derived. Finally, after combining the subsystem models together, an open-loop test is performed and compared to the output of the simulated system model.

4.2 System Modeling

From the modeling point of view, the system may be broken into the three main subsystems as shown in Figure 4.2.1. These subsystems are:

- Motor-cylinder pump
- Water power transmission
- Rotary joint

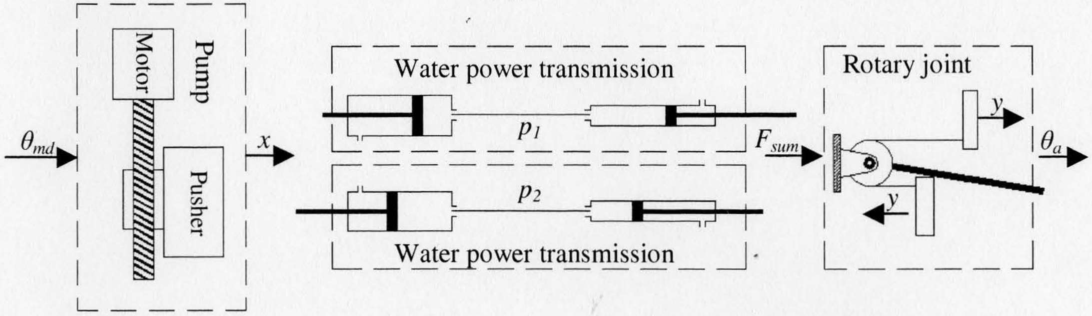

Figure 4.2.1: System modeling, input and output of each subsystem

4.3 Motor-Cylinder Pump

The motor-cylinder pump system discussed in section 3.8 is controlled through a closed-loop PID controller as shown in Figure 4.3.1. In the modelling of the system, the whole pump and its closed-loop controller is replaced by a single transfer function. The mass and friction of the pump cylinders which are a part of pump system is included in this transfer function:

$$G_p(s) = \frac{x(s)}{\theta_{md}(s)} \tag{4.3.1}$$

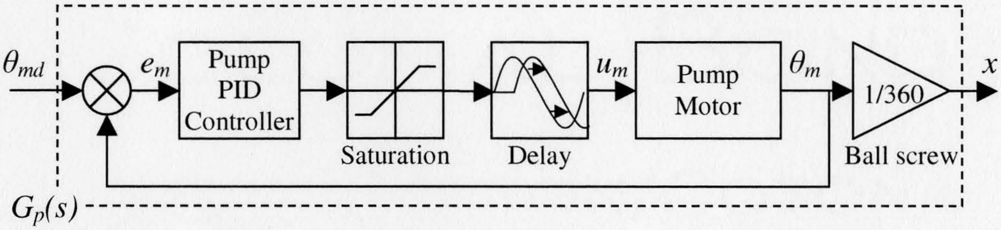

Figure 4.3.1: Block diagram of the pump and its internal controller

To estimate the transfer function, the pump motor is excited by a step input with amplitude of 360° as θ_{md} and the output is measured by the shaft encoder of the motor. The rigid coupling between motor and lead-screw, and negligible play in lead screw enables us to directly estimate the pump cylinder displacement from the encoder output knowing that the lead of the screw is 1 mm/rev. The Akaike final prediction error (FPE) is used as the criterion to evaluate the suitable order of the pump transfer function. As one may observe from Figure 4.3.2, while the error drops significantly by increasing the order of the transfer function to 3, the higher orders does not have remarkable affect on reducing the error. Therefore, a transfer function of the 3rd order is utilized for the pump.

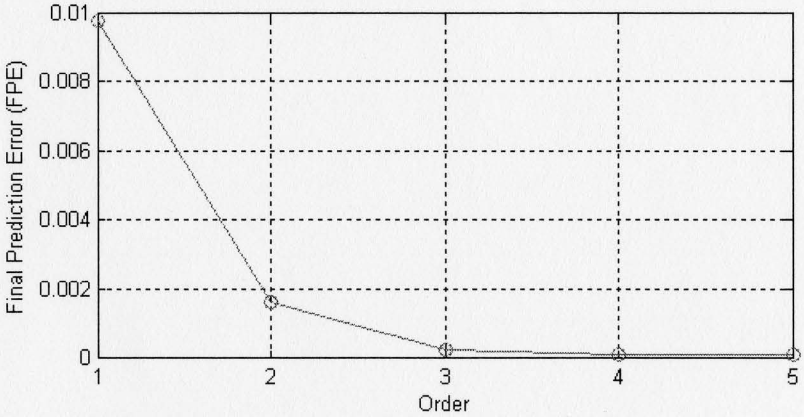

Figure 4.3.2: FPE vs. order of the transfer function

Figure 4.3.3 shows the result for the first pump prototype shown in Figure 3.8.1 in previous section. The estimated transfer function is found to be:

$$G_P(s) = \frac{x(s)}{\theta_{md}(s)} = \frac{86.1e^{-0.005s}}{s^3 + 66.3s^2 + 2279.2s + 31000} \tag{4.3.2}$$

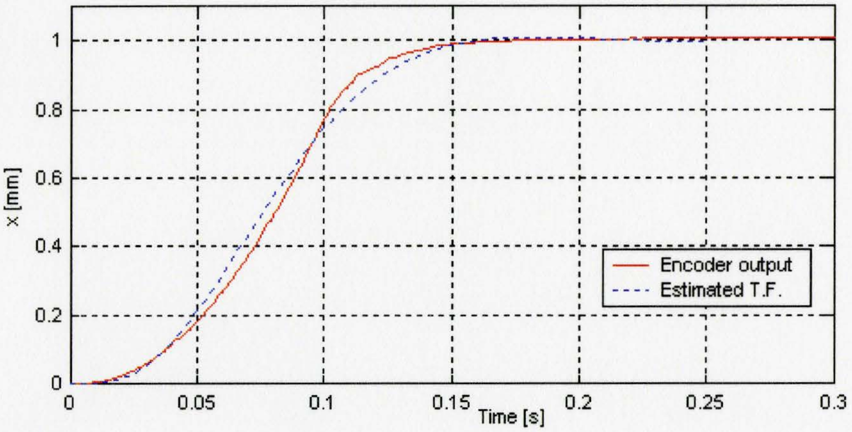

Figure 4.3.3: Step response of the first pump prototype and its estimated transfer function

The same test is repeated for the second pump prototype shown in Figure 3.8.2 and the result is depicted in Figure 4.3.4. The estimated transfer function is found to be:

$$G_P(s) = \frac{x(s)}{\theta_{md}(s)} = \frac{1357.1e^{-0.005s}}{s^3 + 160s^2 + 13956s + 488560} \tag{4.3.3}$$

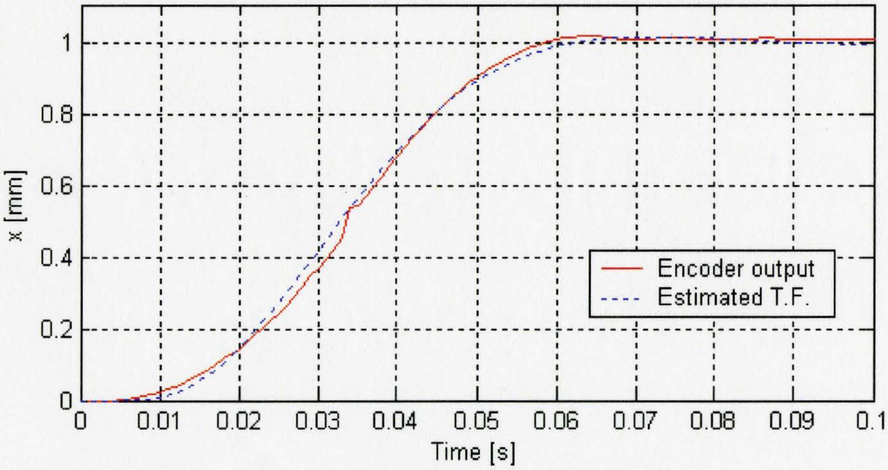

Figure 4.3.4: Step response of the second pump prototype and its estimated transfer function

The driving voltage applied to the pump motor in the previous tests was through a low gain amplifier. The second pump prototype was also attached to a high gain amplifier and the output is recorded as depicted in Figure 4.3.5. The estimated transfer function for this configuration is:

$$G_P(s) = \frac{x(s)}{\theta_{md}(s)} = \frac{6125e^{-0.002s}}{s^3 + 245s^2 + 35700s + 2205000} \tag{4.3.4}$$

The rise time (the time required for the output to rise from 10% to 90% of its final value) for each of these three configurations are 87, 32, and 17 ms respectively. Comparing the results in Figure 4.3.3 to Figure 4.3.5, one can see that the dynamic response of the pump is significantly improved when a high gain amplifier and the lighter mechanical hardware are used.

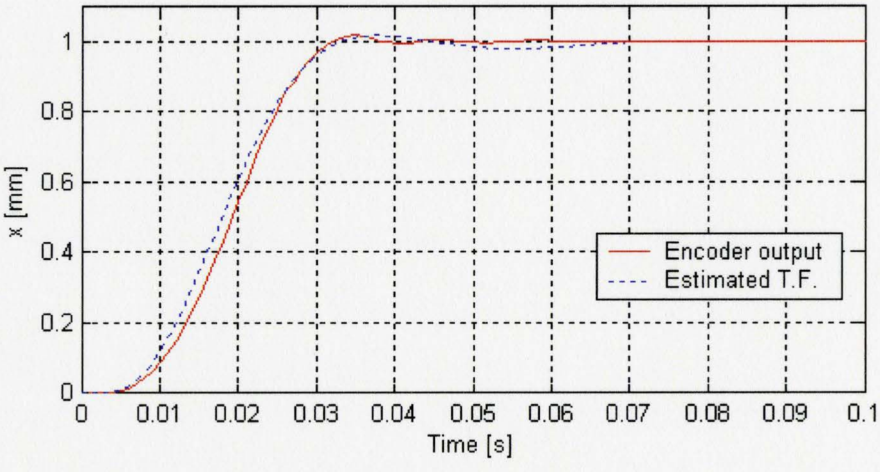

Figure 4.3.5: Step response of the second pump prototype with high gain amplifier and its estimated transfer function

Based on several experiments, the maximum speed and acceleration of the pump motor are 60 RPM and 125 rev/s^2 respectively. Considering that the lead of the ball screw is 1 mm/rev, the maximum theoretical outputs of the pump that will be used in the following section are:

$$\begin{cases} \dot{x}_{\max} = 60mm/s \\ \ddot{x}_{\max} = 125mm/s^2 \end{cases} \tag{4.3.5}$$

These values will also be used as the saturation thresholds in the simulation program.

4.4 Water Power Transmission

The displacements of the pump cylinders are transferred to the rotary joint cylinders through the connecting tubing. The water transmission system as shown in Figure 4.4.1 is modelled in this section by including the following three elements:

- Hydraulic resistance
- Hydraulic Inertance
- Elastic energy storage (compliance)

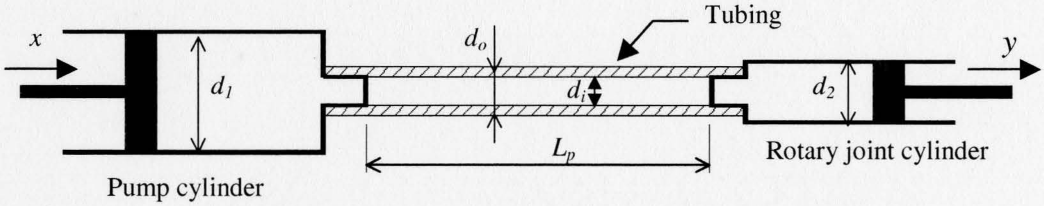

Figure 4.4.1: The water power transmission line

4.4.1 Hydraulic Resistance

When a viscous fluid flows through a long capillary passage a distributed friction over the length of the passage appears. Also a pressure drop is generated where fluid flow experiences a sudden change in passage area as in valves and fittings. These two effects become the source of hydraulic resistance in our system. Knowing the dimensions of the tubing and cylinders, and properties of water we can estimate the hydraulic resistance.

$$\begin{cases} d_1 = 6.35mm \Rightarrow A_1 = 31.7mm^2 \text{ (bore area of the pump cylinder)} \\ d_2 = 4mm \Rightarrow A_2 = 12.6mm^2 \text{ (bore area of the rotary joint cylinder)} \\ d_i = 2.69mm \text{ (inner diameter of tubing)} \\ d_o = 3.99mm \text{ (outer diameter of tubing)} \\ L_p = 300mm \text{ (length of the tubing)} \\ \rho = 1000kg/m^3 \text{ (water density)} \\ \mu = 1.002\times10^{-3} Ns/m^2 \text{ (dynamic viscosity of water at } 20^\circ\text{C)} \end{cases}$$

Using (4.3.5) the maximum water velocity in the tubing will be:

$$v_{\max} = \frac{\text{Area of pump cylinder}}{\text{Inner area of tubing}} \times \dot{x}_{\max} = \frac{d_1^2}{d_i^2} \times \dot{x}_{\max} = 334mm/s \qquad (4.4.1.1)$$

Reynolds number is used as the criterion for flow regime, laminar or turbulent flow. Laminar flow occurs at low Reynolds number (less than 2000) where the viscous forces are dominant [45]. This number for a circular pipe is given by:

$$Re = \frac{\rho v d_i}{\mu} = \frac{1000\times(334\times10^{-3})\times(2.69\times10^{-3})}{1.002\times10^{-3}} = 897 \qquad (4.4.1.2)$$

For a laminar flow in a straight circular smooth pipe, the Hagen-Poiseuille formula applies for the pressure drop due to friction between the viscous fluid and tubing [45]:

$$\begin{cases} \Delta p_r = \dfrac{128\mu L_p}{\pi d_i^4} Q \\ Q_{\max} = v_{\max} \times \dfrac{\pi d_i^2}{4} \end{cases} \Rightarrow \Delta p_{r(\max)} = \frac{32\mu L_p v_{\max}}{d_i^2} \tag{4.4.1.2}$$

$$\Delta p_{r(\max)} = \frac{32\times\left(1.002\times10^{-3}\right)\times\left(300\times10^{-3}\right)\times\left(334\times10^{-3}\right)}{(2.69\times10^{-3})^2} = 4.44\times10^{-4}\,MPa$$

Usually the pressure drop due to sudden change in passage area is negligible for laminar flow [46]; therefore the maximum pressure drop due to hydraulic resistance is less than 5x10^{-4} MPa. Under normal operating conditions the pressure ranges from 0.2 MPa to 0.8Mpa. Therefore this pressure drop is about 0.25% of the minimum pressure in the tubing and will be neglected in the model.

4.4.2 Hydraulic Inertance

Hydraulic inertance is a form of energy stored in the hydraulic system due to accelerating mass of working fluid in long tubing. The general analysis of the inertance in a compressible and viscous fluid is complicated. For simplicity we neglect the distribution of the compliance along the tubing. Using (4.3.5) the maximum acceleration of the fluid in tubing is:

$$a_{\max} = \frac{\text{Area of pump cylinder}}{\text{Inner area of tubing}} \times \ddot{x}_{\max} = \frac{d_1^2}{d_i^2} \times \ddot{x}_{\max} = 697\,mm/s^2 \tag{4.4.2.1}$$

The pressure drop due to the accelerating mass in tubing having an inner cross section of A_i could be found from the following equation [46]:

$$\begin{cases} \Delta p_i = \dfrac{\rho L_p}{A_i}\dfrac{dQ}{dt} \\ \left(\dfrac{dQ}{dt}\right)_{\max} = \dfrac{d(v_{\max}A_i)}{dt} = A_i \times a_{\max} \end{cases} \Rightarrow \Delta p_{i(\max)} = \rho L_p a_{\max} \tag{4.4.2.1}$$

$$\Delta p_{i(\max)} = 1000 \times \left(300 \times 10^{-3}\right) \times \left(697 \times 10^{-3}\right) = 2.09 \times 10^{-4} MPa$$

The pressure drop due to hydraulic inertance is about 0.1% of the minimum pressure in the tubing, which will be neglected in this modelling.

4.4.3 Elastic Energy Storage (Compliance) and Force Output

All hydraulic systems demonstrate some level of compliance which affects the dynamic performance of the system. Three elements of compliance in a water power transmission line are: water compressibility, air bubbles entrained in water, and elasticity of tubing.

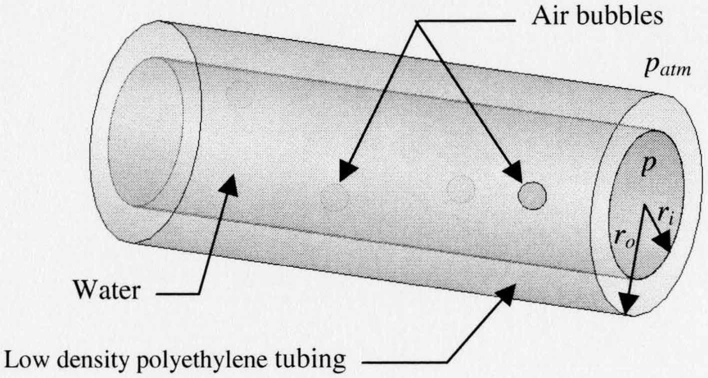

Figure 4.4.2: Elements of compliance in a water power transmission line

When pressure in the tubing rises, the volume of air (V_a) and water (V_w) will reduce while the tubing expands. Usually the air content of the working fluid is a small percentage of the total volume so the initial total volume (V) and tubing volume (V_p) are almost equal to the volume of water:

$$V = V_p = V_w + V_a \approx V_w \tag{4.4.3.1}$$

When the pressure is applied in the tubing, water and air are compressed but the tubing expands:

$$\Delta V = -\Delta V_w - \Delta V_a + \Delta V_p \tag{4.4.3.2}$$

The bulk modulus, also called the modulus of compressibility, is a measure that shows the compressibility of a fluid. It is the ratio of the hydrostatic pressure change required to change the initial volume V_w by ΔV_w [47]:

$$\beta_w = -\frac{\Delta p}{\Delta V_w / V_w} \tag{4.4.3.3}$$

where β_w is the bulk modulus of water and Δp is the pressure change. Compressibility has inverse relation with bulk modulus so the higher the bulk modulus the less compressible the material will be. Typically water has a bulk modulus of 2150 MPa which shows it is relatively incompressible. To reduce the volume of water by 0.1%, a pressure change of more than 2.1 MPa is required. For hydraulic oils this value is much higher (typically more than 300 times less compressible than water).

No matter how well a hydraulic system is designed and implemented, some level of suspended air in fluid is inevitable. The presence of air dramatically reduces the bulk modulus of the working fluid (i.e. it increases the compressibility) especially at lower pressures, which has a significant effect on system performance. The same concept of bulk modulus of fluid may be applied to air bubbles:

$$\beta_a = -\frac{\Delta p}{\Delta V_a / V_a} \tag{4.4.3.4}$$

where β_a is the bulk modulus of air and ΔV_a and V_a are the volume change and initial volume of air entrained in water. The air content suspended in the fluid can be given as a percentage of the total volume of fluid:

$$V_a = S \times V_w = S \times V \tag{4.4.3.5}$$

If the tubing is filled with special caution (i.e. immersed in water while filling) and the system is properly sealed, S will be a very small value ($S<<1$). If the temperature in the system remains constant then β_a indicates isothermal compressibility and in this condition [47]:

$$\beta_a = p \tag{4.4.3.6}$$

where p is the absolute pressure in the line.

The tubing in a hydraulic system may be treated as an open-end pressure vessel if the ends are not blocked (i.e. when they are connected to cylinders and the pistons are free to move). When the ratio of inside radius (r_i) to the wall thickness (t_p) of tubing is less than 10 then the thick-walled formulations can be used [48].

$$\frac{r_i}{t_p} \leq 10 \Rightarrow \text{Thick - walled vessel} \tag{4.4.3.7}$$

Equation (4.4.3.7) for the tubing used in this research leads to a value of 4.2. Therefore the thick-walled formula could be utilized to estimate the volume change in the tubing due to the pressure change. The radial expansion in tubing having modulus of elasticity of E and Poisson's ratio of ν is found to be [48]:

$$\Delta r = \frac{1-\upsilon}{E}\left(\frac{p_i r_i^2 - p_o r_o^2}{r_o^2 - r_i^2}\right) r + \frac{(1+\upsilon)}{E}\frac{(p_i - p_o) r_i^2 r_o^2}{r_o^2 - r_i^2}\frac{1}{r} \tag{4.4.3.8}$$

p_i and p_o are inner and outer gauge pressures and r is any radius such that $r_i < r < r_o$. If the tubing is surrounded by atmospheric pressure ($p_o = p_{atm} = 0$) then (4.4.3.8) simplifies into the following equation for the radial expansion of the inside diameter:

$$\Delta r_i = \frac{r_i \Delta p}{(r_o^2 - r_i^2)E}\left[(1-\upsilon) r_i^2 + (1+\upsilon) r_o^2\right] \tag{4.4.3.9}$$

The bulk modulus for the tubing elasticity (β_p) can be defined which relates the pressure change to the volume change of the tubing:

$$\begin{cases} \beta_p = \dfrac{\Delta p}{\Delta V_p / V_p} \\ \Delta V_p = 2\pi r_i \Delta r_i \Rightarrow \beta_p = \dfrac{r_i \Delta p}{2\Delta r_i} \\ V_p = \pi r_i^2 \end{cases} \tag{4.4.3.10}$$

Substituting Δr_i from (4.4.3.9) into (4.4.3.10), the relationship between bulk modulus of tubing with the dimensions and mechanical properties of the tubing can be written as:

$$\beta_p = \frac{(r_o^2 - r_i^2)E}{2\left[(1-\upsilon) r_i^2 + (1+\upsilon) r_o^2\right]} \tag{4.4.3.11}$$

Incorporating the specifications of the low density polyethylene tubing used in our study, the bulk modulus of the tubing is:

$$\begin{cases} E = 300MPa \\ \upsilon = 0.4 \\ r_i = \dfrac{2.69}{2} = 1.345mm \Rightarrow \beta_p = 48.9MPa \\ r_o = \dfrac{3.99}{2} = 1.995mm \end{cases} \tag{4.4.3.12}$$

Combining the three elements of compliance, an effective bulk modulus can be defined by the following equation:

$$\beta_e = \frac{\Delta p}{\Delta V / V} \tag{4.4.3.13}$$

Substituting (4.4.3.3), (4.4.3.4) and (4.4.3.10) into (4.4.3.2) and comparing with (4.4.3.13) relates the effective compressibility of the line to the individual compressibility of its elements:

$$\begin{gathered} \Delta V_t = \Delta p\left(\frac{V}{\beta_w} + \frac{SV}{\beta_a} + \frac{V}{\beta_p}\right) \\ \frac{\Delta V}{V\Delta p} = \frac{1}{\beta_e} = \frac{1}{\beta_w} + \frac{S}{\beta_a} + \frac{1}{\beta_p} \end{gathered} \tag{4.4.3.14}$$

Each term in (4.4.3.14) shows the effect of the corresponding source of compliance on the total compressibility of the system. Assuming that the air content of the water ranges between 0.1% to 1%, and the absolute pressure in the tubing ranges between 0.2 to 0.8 MPa, then the numerical values for the compressibility for each of the elements in (4.4.3.14) can be found as follows:

$$\begin{cases} \dfrac{1}{\beta_w} = \dfrac{1}{2150} = 0.465\times10^{-3}\,/\,MPa \text{ (compresibility of water)} \\ \dfrac{S}{\beta_a} = \dfrac{S}{p} = \dfrac{(0.1\%...1\%)}{(0.2...0.8)} = (1.25...50)\times10^{-3}\,/\,MPa \text{ (compresibility of air content)} \\ \dfrac{1}{\beta_p} = \dfrac{1}{48.9} = 20.4\times10^{-3}\,/\,MPa \text{ (compresibility of tubing)} \end{cases}$$

Comparing compressibility values calculated above, the followings can be concluded:

- Compressibility of water does not play a significant role compared to tubing (more than 40 times less compressible).
- The effect of air bubbles is most significant at low pressures.
- Tubing elasticity is the dominant factor when air percentage is low and the pressure in the hydraulic lines is high.

Figure 4.4.3 shows the effect of tubing length and air percentage in the pressure-volume relationship. As one can see in Figure 4.4.3, $\Delta p/\Delta V$ could be considered to be linear for pressures higher than 0.1 MPa (particularly when S<0.5%).

$\Delta p/\Delta V$ is an important parameter in our modeling and is measured by experiment. To directly extract $\Delta p/\Delta V$ from experiment without affecting the air content of the water in tubing, the cylinder in rotary joint is fixed while the pump cylinder is moved. The ball screw in the preload system provides a built-in lock which also prevents the preload cylinder from moving when the preload motor is not working. Figure 4.4.4 shows the part of the total system (already shown in Figure 3.9.1) that is used in this experiment. A displacement of Δx in the pump cylinder causes a change in volume of $\Delta V = A_1\Delta x$.

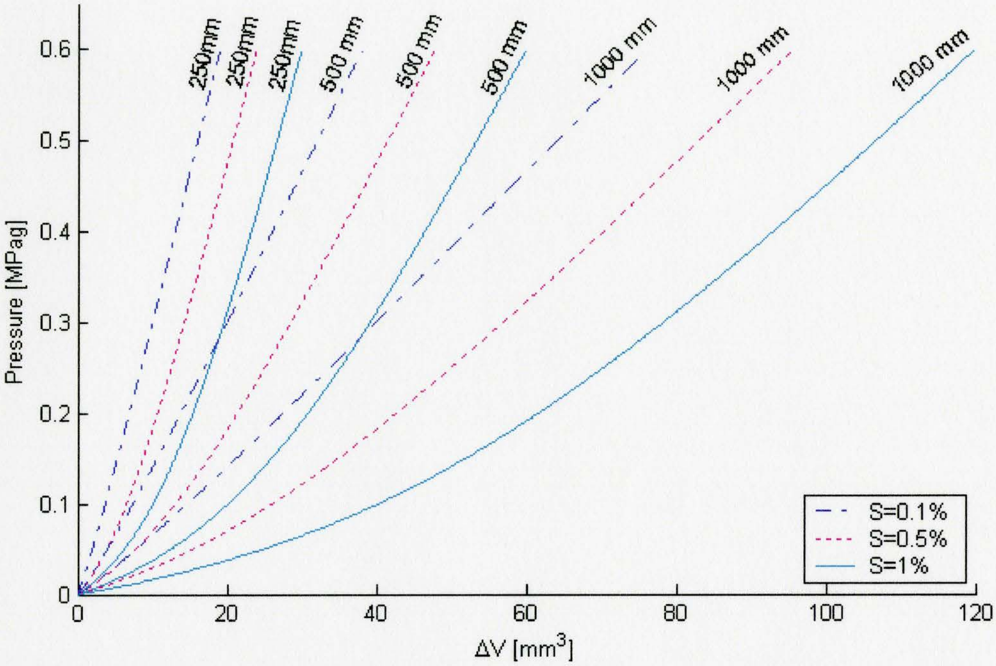

Figure 4.4.3: Pressure vs. volume change for various tubing lengths and air percentages

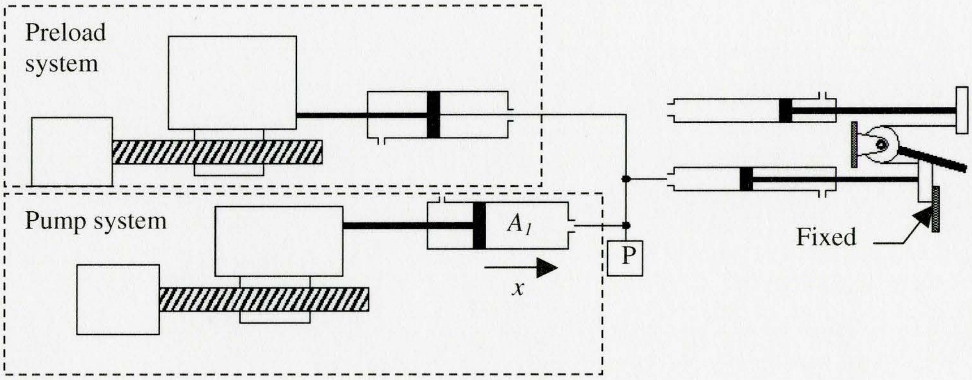

Figure 4.4.4: Compliance test setup

A value of $\Delta p/\Delta V$=0.0257 MPa/mm^3 is extracted from Figure 4.4.5 which shows the result of this test.

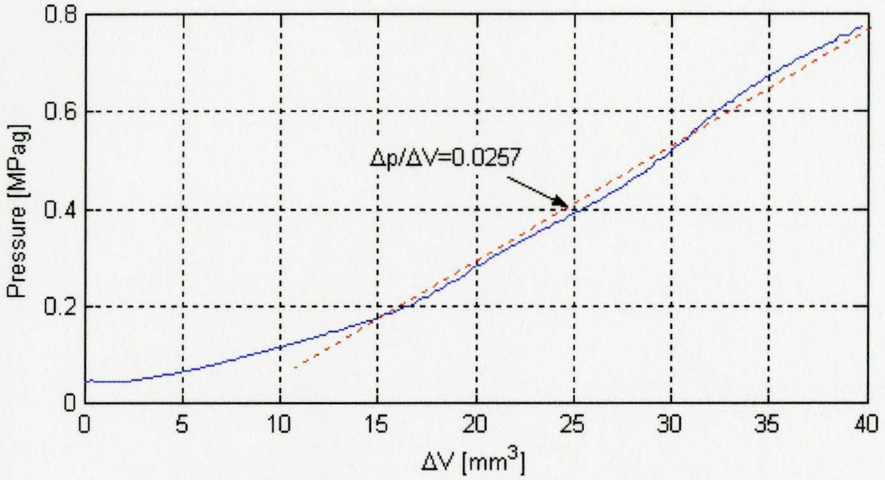

Figure 4.4.5: Compliance test result

Note that by neglecting the hydraulic resistance and inertance in the water power transmission line, the water pressure will be uniform throughout the system and Δp represents the pressure change due to the change in the volume in the whole line from the pump cylinder to the joint cylinder.

Referring to Figure 4.2.1, if a displacement of Δx in the piston of the pump cylinder generates a displacement of Δy in the piston of the joint cylinder, the change in volume in line 1 will be:

$$\Delta V = A_1 \Delta x - A_2 \Delta y \tag{4.4.3.15}$$

The change in volume in line 2 will be equal to that in line 1 but with negative sign. The pressure in each line and output force transmitted to the rotary joint (F_{sum}) can be written as follows:

$$
\begin{aligned}
p_{1j} &= p_{1(j-1)} + \frac{\Delta p}{\Delta V}\left(A_1 \times \Delta x - A_2 \times \Delta y\right) \\
p_{2j} &= p_{2(j-1)} - \frac{\Delta p}{\Delta V}\left(A_1 \times \Delta x - A_2 \times \Delta y\right) \\
F_{sum} &= F_1 - F_2 = (p_{1j} - p_{2j})A_2
\end{aligned}
\tag{4.4.3.16}
$$

where p_{1j} and p_{2j} are the current pressures in line 1 and 2, and $p_{1(j-1)}$ and $p_{2(j-1)}$ are the pressures in the last sampling period.

4.4.4 Leakage

The force that water can transfer from pump to the rotary joint is determined with the pressures in the lines as shown in (4.4.3.16). The performance of the system and the model is directly affected with the unexpected pressure loss due to leakage in the system. The major source of the leakage is the fittings where tubing attaches to cylinders and pressure sensors. Replacing quick connectors with the barb type of fittings had a significant effect in reducing the leakage.

To estimate this effect, both lines are pressurized while the pump and rotary joint cylinders are fixed and the pressures are recorded for 15 s. The result of this test is depicted in Figure 4.4.6. The following may be concluded by analyzing this graph:

- The pressure loss due to leakage is more significant at higher pressures.
- The pressure drop at 0.62 MPag is about 0.03 MPa/s (≈5%/s), while at 0.6 Mpag the pressure drop reduces to less than 0.01 MPa/s (≈1.5%/s). At pressures below 0.58 MPag the pressure drop due to leakage is very small (less than 0.5%/s)

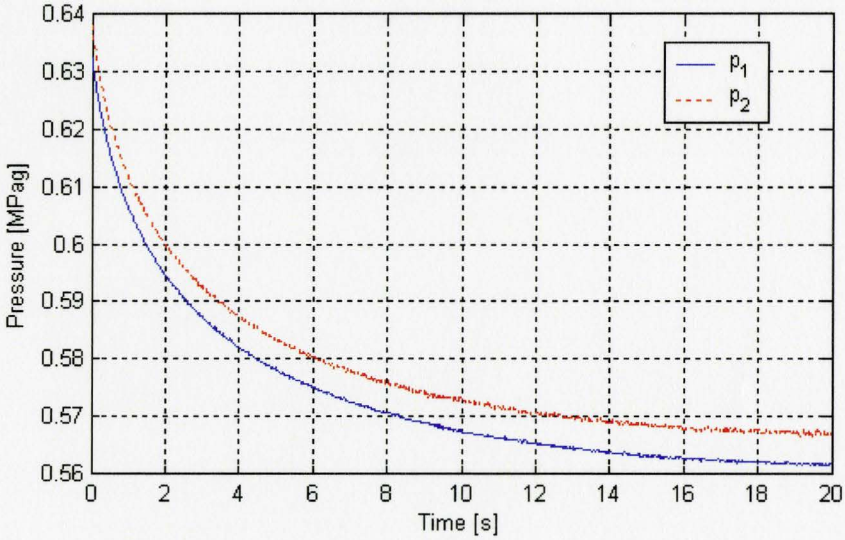

Figure 4.4.6: Pressure drop due to leakage

Usually, the pressures in the water transmission lines are working below 0.55 MPag. The only time that the pressure exceeds this number is when the system overcomes the static friction which happens in a short time period. Also the duration of the tests are usually very small as compared to the time needed to experience a significant pressure loss due to leakage. Therefore in this research the effect of leakage is neglected in the system modeling.

4.5 Rotary Joint

The output force from the water power transmission system is the input to the rotary joint subsystem. The string is low stretch Nylon, therefore having negligible elasticity. Two major elements are considered in modelling this subsystem:

- Friction of the moving parts in the rotary joint
- Inertia due to the mass of the moving parts

4.5.1 Friction in Rotary Joint

Friction in the rotary joint appears at the pistons of the joint cylinders, pulley, and sliders. To estimate the friction a series of tests are conducted actuating the pump motor with ramp inputs at different speeds. Pressures in lines 1 and 2 are recorded through pressure sensors as shown in Figure 3.9.1. The pressure difference between the two lines times the bore area of the joint cylinders is calculated as the total friction in the system. A typical output is shown in Figure 4.5.1. Using (3.6.4) the relation between the speed of the sliders and rotation speed of output arm is given by:

$$\begin{aligned} \dot{y} &= \frac{\dot{\theta}_a}{16.8} \\ \ddot{y} &= \frac{\ddot{\theta}_a}{16.8} \end{aligned} \qquad (4.5.1.1)$$

θ_a is measured through the rotary encoder as explained in section 3.7 and $d\theta_a/dt$ is calculated by backwards differencing of θ_a.

The friction model in this research includes three parameters as depicted in Figure 4.5.2:

- Stick-slip friction (F_s): opposes the direction of motion when the sliding velocity is zero. The value of this friction rises as the applied force increases. When the force reaches to a threshold referred to as static friction, the sliding motion starts.
- Coulomb friction (F_c): opposes the direction of motion with a constant value referred to as sliding friction. As soon as the motion starts, the value of friction drops from static to sliding friction.

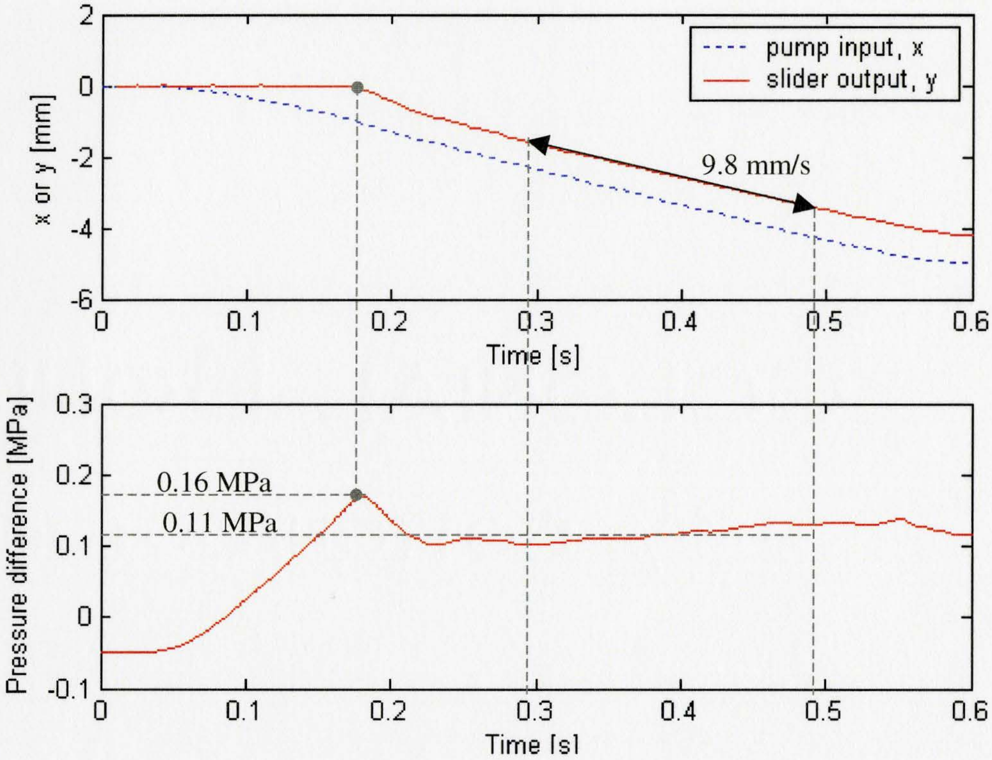

Figure 4.5.1: Displacement and pressure difference vs. time for friction estimation

- Viscous friction: is a velocity dependant friction which opposes the motion. The higher the speed, the more opposing viscous friction will be added to the Coulomb friction. This friction can be calculated by multiplying velocity by the viscous friction coefficient (C_v). The diagram in Figure 4.5.2 shows these parameters.

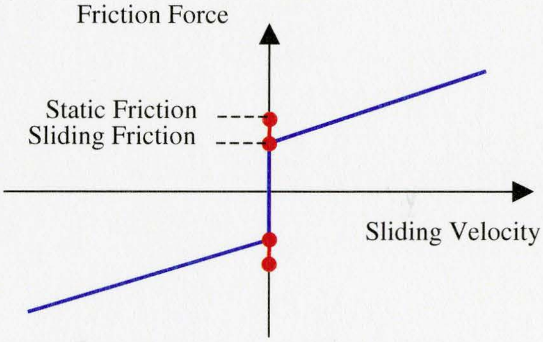

Figure 4.5.2: Three elements of friction in this study

The friction model can be mathematically described by the following equations:

$$\begin{cases} f = F_{sum} & \dot{y} = 0 \,\&\, |F_{sum}| < F_s \\ f = sign(F_{sum}) \times F_s & \dot{y} = 0 \,\&\, |F_{sum}| \geq F_s \\ f = sign(\dot{y}) \times (F_c + C_v|\dot{y}|) & \dot{y} \neq 0 \end{cases} \qquad (4.5.1.2)$$

where f is the friction force. F_s can be easily extracted from the test results (e.g. from Figure 4.5.1) by recording the maximum pressure difference before any output slider displacement is recorded. The pressure difference times the bore area of the joint cylinder is the estimated static friction (0.16 MPa x 12.6 mm^2 = 2.02 N in Figure 4.5.1). The average of the estimated static frictions over different tests is used as F_s in our model.

F_c and C_v can be estimated by noting that during a constant velocity motion of the output slider, the pressure difference is almost constant (see Figure 4.5.1). Using the constant velocity segments of different tests, the average of the pressure differences are used to estimate the total of the sliding and viscous friction for that velocity (0.11 MPa x 12.6 mm^2 = 1.42 N at output slider velocity of 9.8 mm/s in Figure 4.5.1). These values for different tests can be drawn in a graph similar to the one shown in Figure 4.5.3.

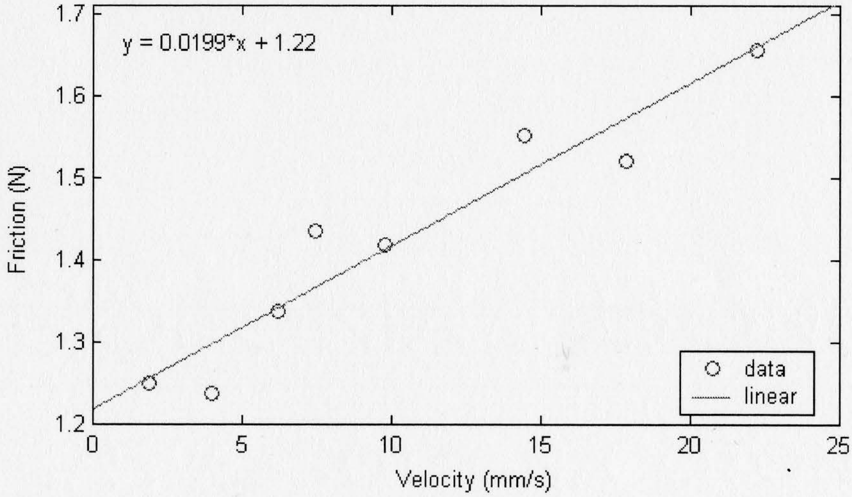

Figure 4.5.3: Coulomb and viscous friction vs. slider velocity

Using linear curve fitting over the recorded data, F_c and C_v can be estimated (F_c=1.22 N and C_v=0.0199 Ns/mm in Figure 4.5.3).

Due to a lack of precision in manufacturing and tolerance problems, two issues regarding friction have arisen. The friction forces in the positive and negative directions are different, and the friction forces have been increased significantly over time. The estimated friction values used in the model based controller to be explained in the next chapter are given in (4.5.1.3) for negative direction and (4.5.1.4) for positive direction[1]:

$$\text{Negative direction}: \begin{cases} F_s = 4.03N \\ F_c = 2.97N \\ C_v = 0.0172Ns/mm \end{cases} \tag{4.5.1.3}$$

$$\text{Positive direction}: \begin{cases} F_s = 7.20N \\ F_c = 5.27N \\ C_v = 0.0235Ns/mm \end{cases} \tag{4.5.1.4}$$

4.5.2 Inertia in Rotary Joint

The effect of accelerating masses in the rotary joint is modelled in this section. The mass of the water in the tubing in both lines are also included in this model. The moving parts may have rotary or linear displacement. The masses of translating parts can be directly used while for rotating parts the effective mass is calculated using the moment of inertia of that part and the effective radius (r_p) of the pulley. r_p is the radius at which the linear force from the sliders applies to the pulley (Figure 4.5.4). If the moment of inertia of a rotating body is given by J, then its effective mass (m_e) can be calculated by:

---

[1] The data used to obtain these values is provided in appendix A.

$$m_e = \frac{J}{r_p^2} \tag{4.5.2.1}$$

In our rotary joint r_p=3.4 mm and the masses of the translating parts and effective mass of the rotary parts depicted in Figure 4.5.4 are as follows:

- Linear displacement (mass)
  - Aluminium sliders (m_{slider} x 2): 5.2 g
  - Rotary joint cylinders' pistons (m_{piston} x 2): 4.0 g
  - Water in tubing and cylinders (m_{water} x 2): 4.0 g
- Rotary displacement (moment of inertia, effective mass)
  - Brass pulley (J_{pulley}, m_{pulley} x 1): 9.1 gmm^2, 0.8 g
  - Aluminium arm (J_{arm}, m_{arm} x 1): 51.6 gmm^2, 4.5 g

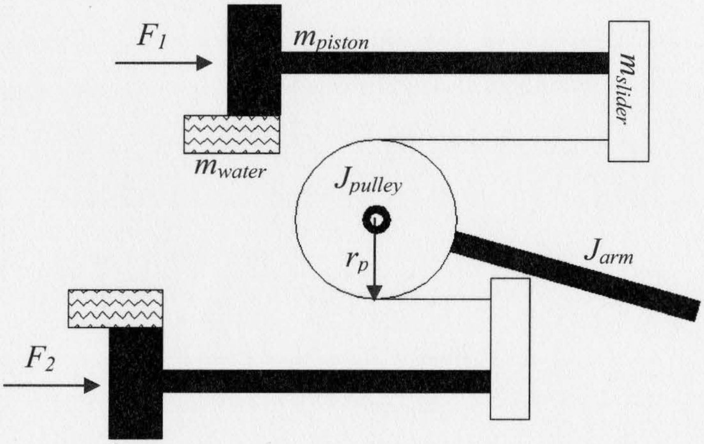

Figure 4.5.4: Rotary joint's parts

Adding up the masses above, the total effective mass (m) in the rotary joint becomes 18.5 g. The relationship between the total effective mass and the acceleration of the output sliders can be found using the Newton's second law:

$$\sum F = m\ddot{y} \Rightarrow \ddot{y} = (F_{sum} - f)/m \tag{4.5.2.2}$$

Using (4.5.1.2) we can expand (4.5.2.2) in the following form:

$$\begin{cases} \ddot{y} = 0 & \dot{y} = 0 \,\&\, |F_{sum}| < F_s \\ \ddot{y} = [F_{sum} - sign(F_{sum}) \times F_s]/m & \dot{y} = 0 \,\&\, |F_{sum}| \geq F_s \\ \ddot{y} = [F_{sum} - sign(\dot{y}) \times (F_c + C_v|\dot{y}|)]/m & \dot{y} \neq 0 \end{cases} \tag{4.5.2.3}$$

4.6 Model validation

An open-loop test has been conducted to validate the precision and performance of the system modeling. A sinusoidal input has been chosen to subject the system to the friction difference between the positive and negative directions.

Since the input to the open-loop system is θ_{md} and the output is θ_a, it is useful to find the approximate scaling factor relating these two quantities. This scaling factor will allow θ_{md} to be scaled to not exceed the range of θ_a which is ±120°. Ideally, if no motor transfer function in the pump and no compliance in the water power transmission line were involved, then the input and outputs to each subsystem in Figure 4.2.1 would have been as depicted in Figure 4.6.1. Replacing A_1 and A_2 the relation between θ_{md} and θ_a can be written as:

$$\theta_a = 16.8(\frac{A_1}{A_2})(\frac{1}{360})\theta_{md} = 0.1176\theta_{md} \Rightarrow \theta_{md} = 8.5\theta_a \tag{4.6.1}$$

The sinusoidal input chosen for open-loop validation has a frequency of 2 Hz and is given by:

$$\theta_{md} = 8.5 \times 120 \sin(4\pi t) \tag{4.6.2}$$

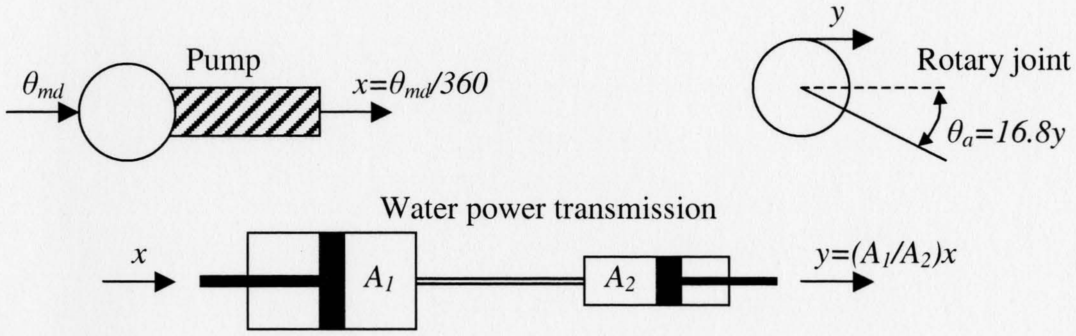

Figure 4.6.1: Subsystems simplified relationship

A simulation program written in Matlab is used to compare the results from the system modelling with the experimental results. Figure 4.6.2 shows the flowchart of the program. The results from simulation and experiment for the input given in (4.6.2) are shown in Figures 4.6.3 and 4.6.4. The initial pressures in lines 1 and 2 (p_{10} and p_{20}) are recorded to be 0.32 and 0.14 MPa respectively which are also used in the simulation. Figure 4.6.4 shows the measured pressures for this test. The arm starts moving as soon as the pressure difference between line 1 and 2 overcomes the static friction in the positive direction. When the direction of the input reverses, the arm stops moving and the pressure in line 2 increases while in line 1 it decreases. When pressure difference between lines 2 and 1 overcomes the static friction in the negative direction, the arm starts rotating in the opposite direction.

The experimental results and simulation outputs are in good agreement, and the system model employed in this simulation will be used to design the model based controller in the next chapter.

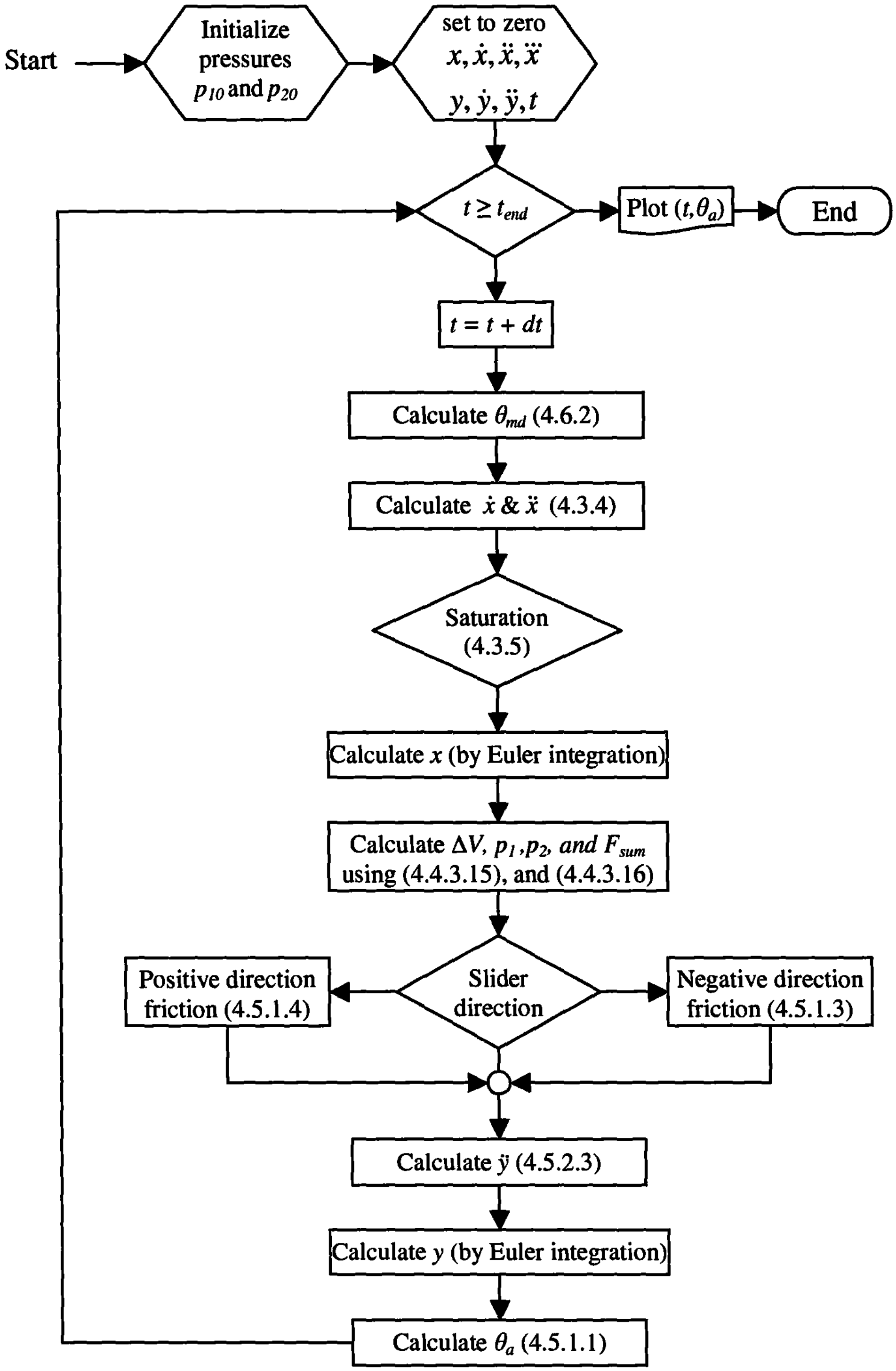

Figure 4.6.2: Open-loop simulation program flowchart

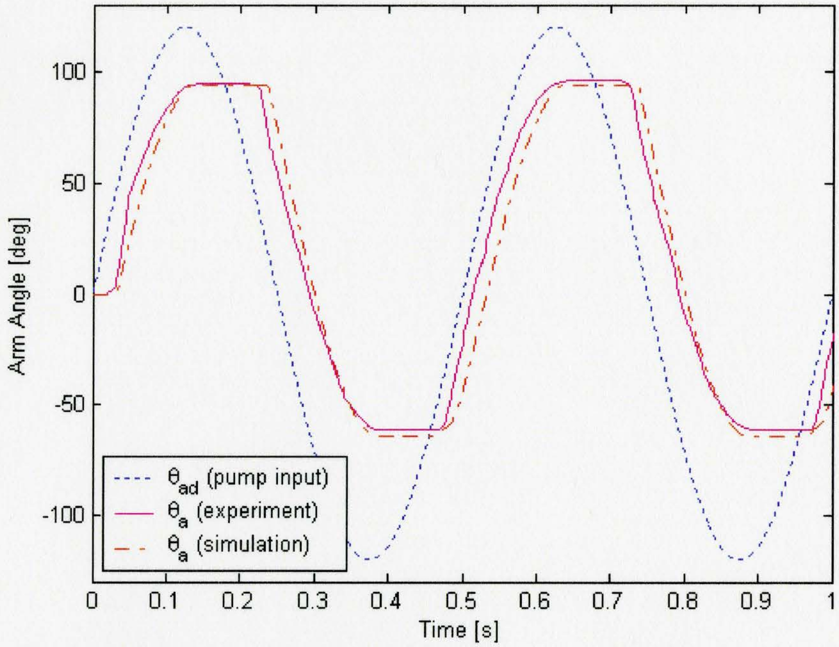

Figure 4.6.3: Experimental and simulation results to a sinusoidal input

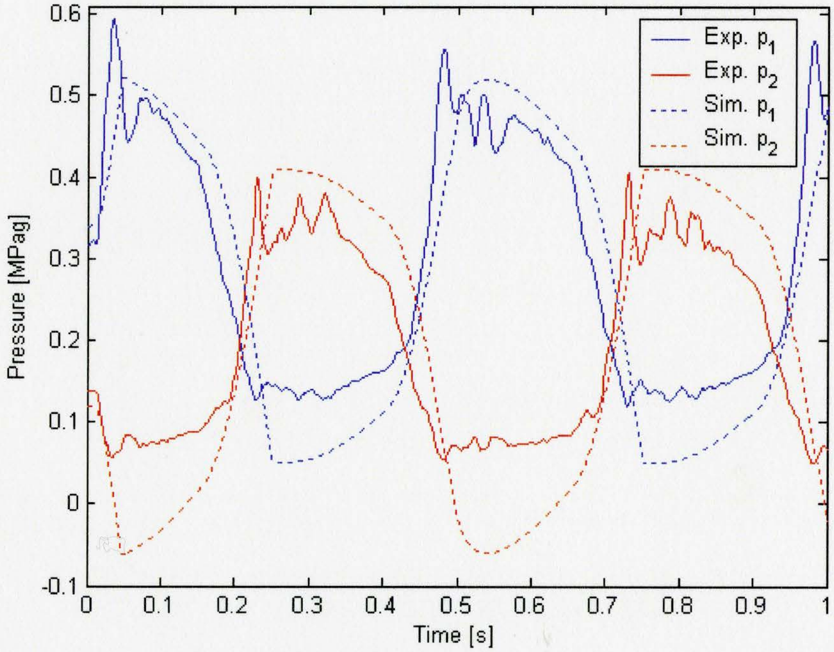

Figure 4.6.4: Experimental and simulation pressures for the sinusoidal input test

4.7 Conclusion

The apparatus developed for this research was modelled in this chapter. The model was based on three subsystems. The factors to be considered in each subsystem were studied and the effective parameters were identified. A single transfer function modelled the whole pump hardware and its PID closed-loop controller. The compliance of the water transmission line was analytically proven to be the major player in the performance of this subsystem. Experimental results were used to model this subsystem. The rotary joint was modelled by an effective mass that reflects the total translational and rotational elements in this subsystem. Friction was also included in the model for this subsystem having three elements of static, sliding and viscous friction. A simulation program was written based on the derived system model and a validation test has verified the performance of the model.

CHAPTER 5

SYSTEM CONTROL AND EXPERIMENTS

5.1 Introduction

This chapter is dedicated to the system controller design and results of the experiments based on the controlled system. Although a PID controller does not guarantee optimal control of the system, in many applications involving actuator control it is sufficient. The PID controller will be enhanced by adding a high frequency dither signal, control signal smoothing and initial pressure adjustment to improve its performance. Next a simulation will be performed based on a model based feedforward controller together with the PID controller. The experimental results for the PID controller with and without the feedforward term will be compared. To check the robustness of the controller, un-modeled disturbances will be generated and the results of tests will be compared. Finally the potential improvements in the system performance are evaluated through additional simulations.

5.2 PID Controller

One of the advantages of the current apparatus is that it is easier to control than the previous version presented in [36]. The desired arm angle (position control) is being achieved by controlling the servomotor in the motor-cylinder pump. The systems employing servo-motors are usually easier to control than the ones performing through solenoid valves as in [36]. A conventional PID controller will be the first method implemented for these reasons.

5.2.1 PID Controller Design

Figure 5.2.1 presents the structure of the system with a PID controller. Note that a PID controller for the pump has already been included in the pump transfer function as explained in section 4.3.

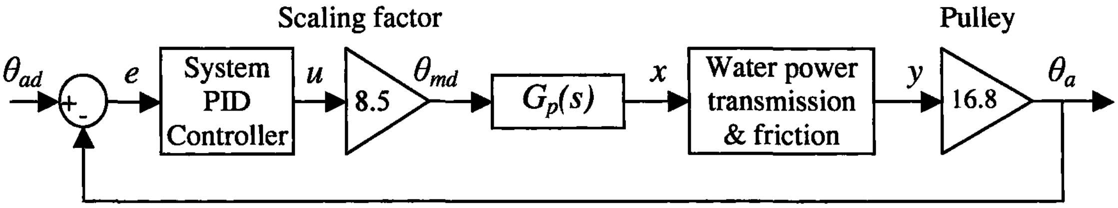

Figure 5.2.1: System block diagram with PID controller

A PID controller output, *u(t)* is calculated using the error *e(t)* between the setpoint and the real output of the system and can be shown in the following form:

$$u(t) = K_p e(t) + K_i \int e(t)dt + K_d \dot{e}(t) \tag{5.2.1.1}$$

Where K_p, K_i, and K_d are the proportional, integral and derivative gains of the PID controller. Considering a sampling period of t_s, the derivative and integral of e can be approximated by the following equations relating the values for the *i*th and *i-1*th samples:

$$\begin{aligned} \dot{e}_i &= \frac{e_i - e_{i-1}}{t_s} \\ \int e_i &= \int e_{i-1} + e_i t_s \end{aligned} \tag{5.2.1.2}$$

The initial values for the PID controller gains were estimated by employing Ziegler–Nichols stability method. K_i and K_d were set to zero and K_p was increased to a critical gain K_c at which the output starts oscillating for a step input. The oscillation period P_c was also recorded and the gains then are set based on the following:

$$\begin{cases} K_p = 0.6K_c \\ K_i = 2K_p/P_c \\ K_d = K_p P_c/8 \end{cases} \tag{5.2.1.3}$$

Finally a manual fine tuning was performed for the best performance of the controller. Figure 5.2.2 presents the output of the system to a ramp input of -80° in 1 s. A significant initial delay occurs before static friction is overcome, and repeated stiction while the arm is rotating may be observed in Figure 5.2.2.

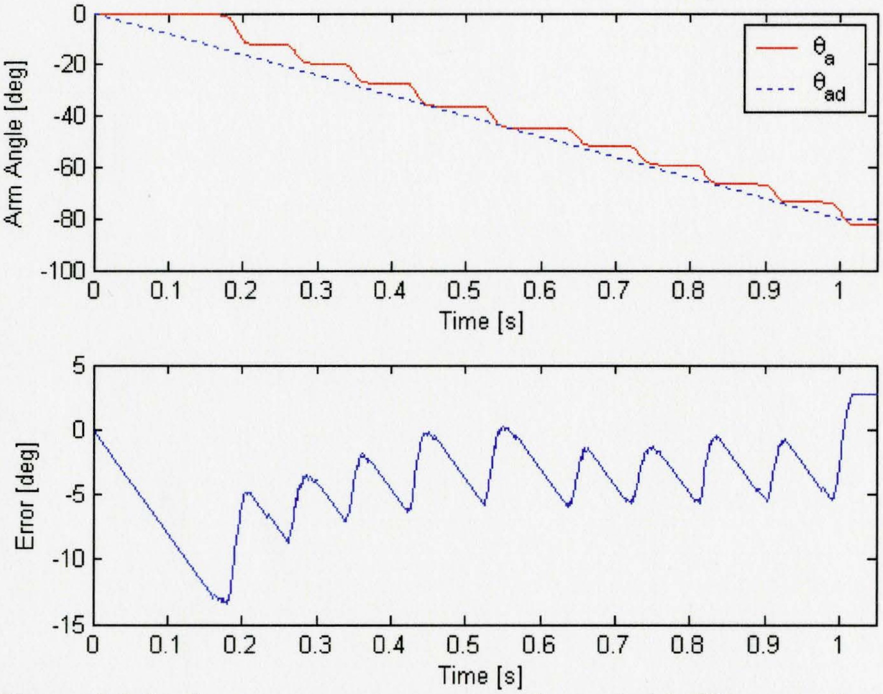

Figure 5.2.2: System response to a ramp input (with PID controller)

The following subjects are studied to address these issues:

- Adding high frequency signals (known as dither)
- Smoothing the derivative of the error

- Reducing the initial stick-slip phase

5.2.2 High Frequency Excitation (Dither)

Dither is a high frequency square wave signal that is added to the control signal. An appropriate dither may reduce the stick-slip friction problem. A series of tests were conducted to find the right amplitude and frequency of the dither signal for our system. Since the sampling period is 1 ms, the maximum frequency was 500 Hz. Figure 5.2.3 presents the response for the same input as in Figure 5.2.2 when a dither with a frequency of 250 Hz and amplitude of ±1 V is directly added to the control signal for the pump motor, u_m. The maximum magnitude of the input to the pump motor is 10V, so this correspond to a dither of ±10% of max(u_m). The initial stick-slip phase is slightly reduced while the arm motion is significantly smoother than the un-dithered condition.

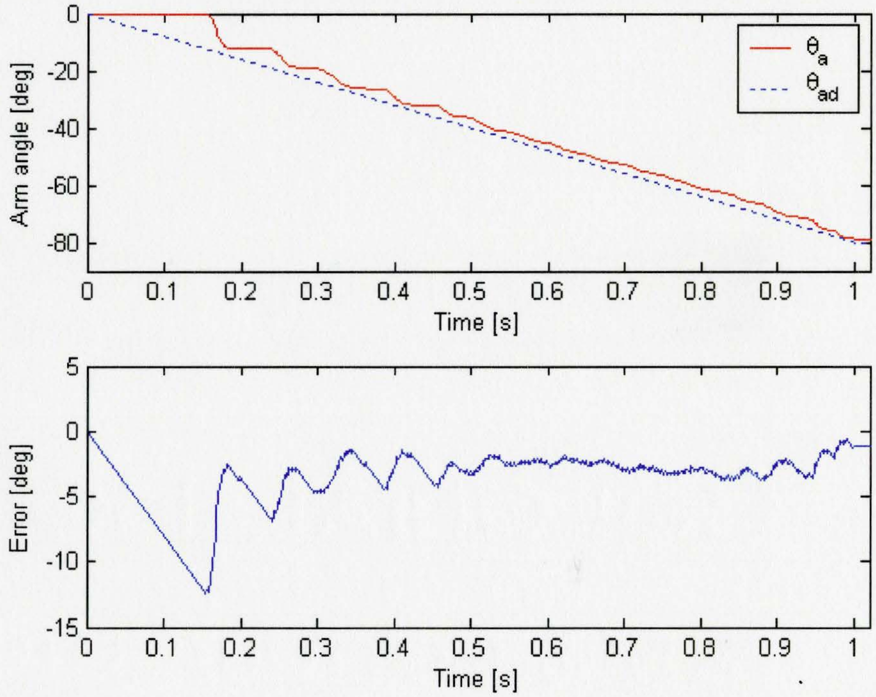

Figure 5.2.3: System response to a ramp input (PID + Dither 1V, 250Hz)

Dither may affect certain characteristics of the systems such as natural frequencies, stiffness, and equilibrium states [38], therefore it is important to retune the PID controller for a better result after dither is implemented.

5.2.3 Smoothing the Error Derivative

In the PID controller, the rate of change of error is calculated by first derivative of error with respect to time. The differentiation of a signal is a major source of high frequency noise amplification; therefore the derivative part of the PID controller is very sensitive to noise. The system can become very oscillatory if the noise and the derivative gain are large. The large changes in the error when the static friction overcomes can act as a noise causing an aggressive output in the control signal. Figure 5.2.4.a illustrates the controller signal for the test shown in Figure 5.2.3. The spikes in the control signal are a result of the amplification of the sudden change of the error.

To reduce this effect, the derivative part is calculated over certain number of consecutive sampling period. This can be shown mathematically by the following equation:

$$\dot{e}_j = \frac{e_j - e_{j-n}}{n \times t_s} \tag{5.2.3.1}$$

Where n is the number of sampling periods, e_j and e_{j-n} are the errors for the jth and $(j-n)$th samples. Equation (5.2.3.1) provides low pass filtering of e_j when n>1. Selecting a suitable value of n is important. A large n makes the control signal smoother but causes more delay between error and generated control signal which may cause more tracking error. Figures 5.2.4.b and 5.2.4.c show the simulated filtered PID control signals when the filtering is performed over 5 and 10 sampling periods, respectively. The real control signal may be different from the ones shown in 5.2.4.b and 5.2.4.c as the real output and consequently the error will be different. The control signal is significantly smoother and less noisy while the overall trend of the control signal may be intact.

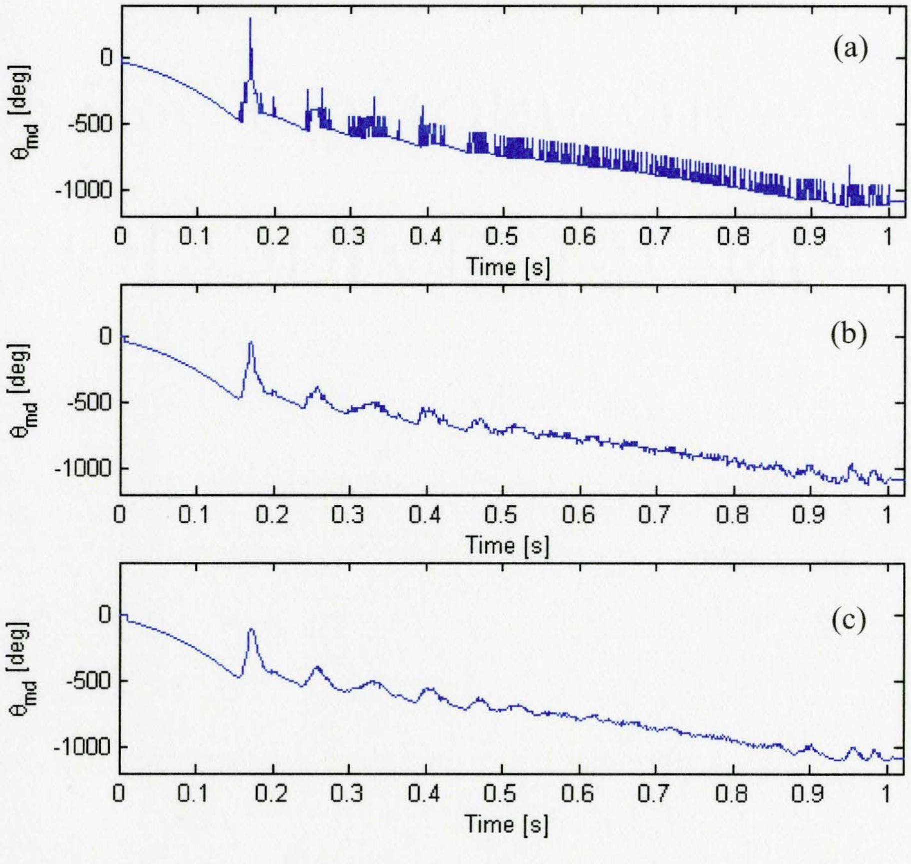

Figure 5.2.4: Simulated control signal for (a) no filtering, (b) *n*=5, and (c) *n*=10

5.2.4 Reducing Initial Stick-Slip Phase

A closer look at the initial response to the ramp input in Figure 5.2.3 reveals that the initial stick-slip phase may be a source of the tracking error. Due to the system compliance, the displacement of the pump cylinder does not generate any output in the rotary joint cylinder and the initial error increases. The large error at the end of the initial sick-slip phase generates a forceful control signal to compensate the error. The powerful fluctuations of the control signal cause a frequent change in friction modes from static to sliding and vice versa that become visible in the arm rotation as a series of steps. Although the procedure of smoothening error derivative explained in section 5.2.2 may improve the situation, it is not sufficient for the initial stick-slip phase.

Figure 5.2.5 shows the pressure changes in line 1 and 2 of the system for the ramp input depicted in Figure 5.2.3. To overcome the initial stick-slip friction, the pressure difference between line 2 and 1 should reach a value that exceeds the static friction.

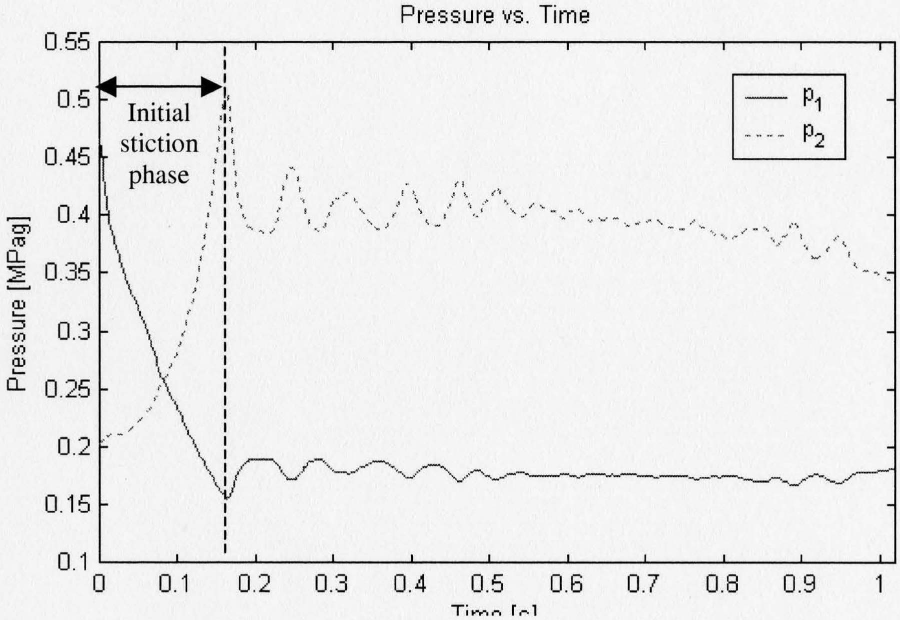

Figure 5.2.5: Pressure change for ramp input for the test shown in Figure 4.2.3

To reduce the time to overcome the initial stiction phase, the pressure difference is changed by advancing the pump cylinder before the control loop starts. The pump is commanded to feed in appropriate direction until the pressure difference meets the following condition:

$$\begin{cases} p_2 - p_1 = 0.1MPa \text{ (Negative direction)} \\ p_1 - p_2 = 0.2MPa \text{ (Positive direction)} \end{cases} \tag{5.2.4.1}$$

The difference between negative and positive direction is from the fact that the friction in positive direction is higher than the negative direction as shown in (4.5.1.3) and (4.5.1.4). The initial pressure differences are set to assure that no output motion will initiated before the control loop starts. Figure 5.2.6 illustrates the system response to a ramp input of -80° in 1 s using a PID controller with a 1V, 250 Hz dither, error derivative filtering and this initial pressure adjustment. The initial stick-slip phase is significantly reduced which has a significant effect on the subsequent performance of the system.

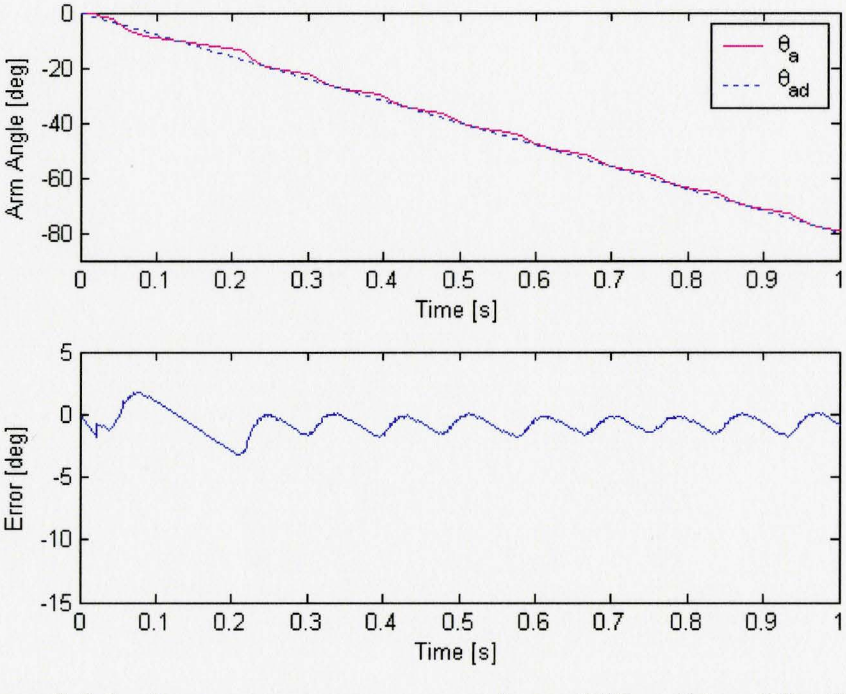

Figure 5.2.6: System response to a ramp input (PID + dither 1V, 250Hz + error derivative filtering + initial pressure adjustment)

5.2.5 Testing Procedure

Numerous tests will be conducted to evaluate the performance of the PID controller. These will be based on the seven trajectories as shown below:

a. Ramp input (120° in 1s, total test time 1s)

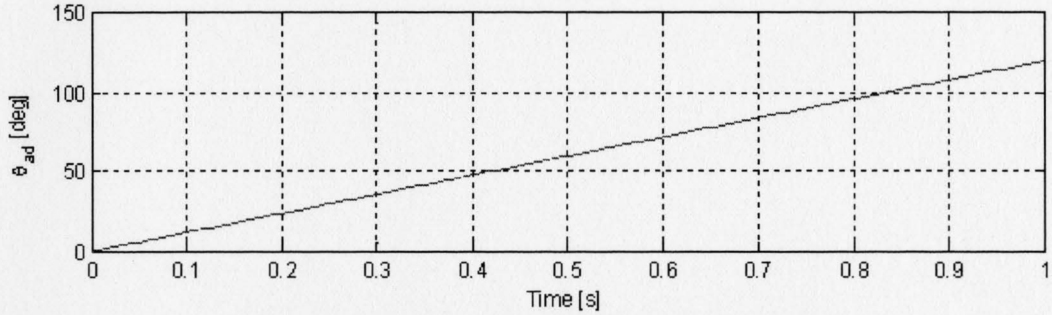

Figure 5.2.7: Positive direction ramp input

b. Ramp input (-120° in 1s, total test time 1s)

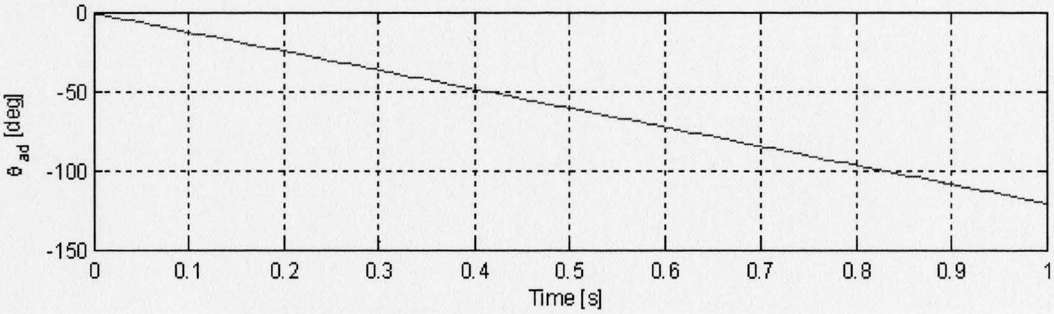

Figure 5.2.8: Negative direction ramp input

c. Sinusoidal input (±60°, 0.5Hz, total test time 4s)

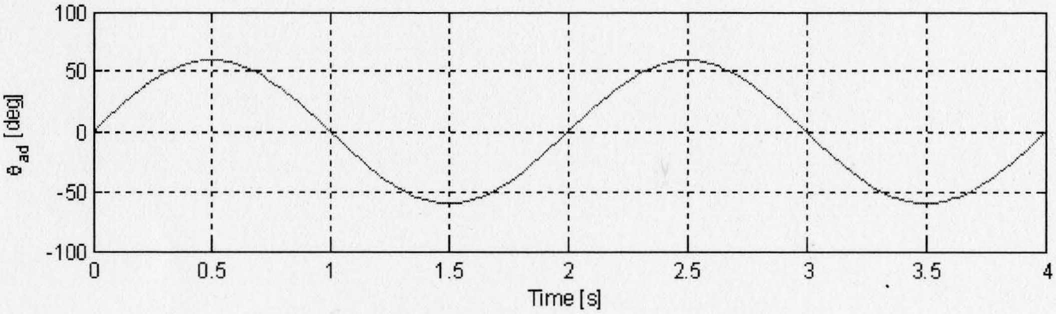

Figure 5.2.9: Sinusoidal input ($60\sin\pi t$)

d. Sinusoidal input (±60°, 1Hz, total test time 2s)

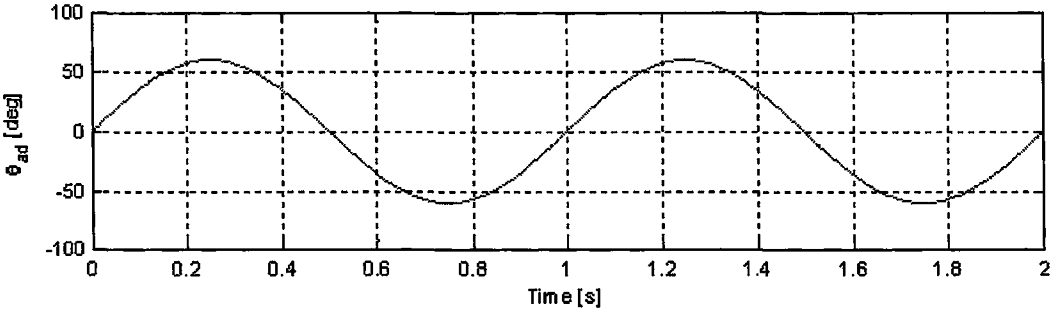

Figure 5.2.10: Sinusoidal input (60sin$2\pi t$)

e. Cycloidal input (120° in 1s, total test time 2s). See [37] for the equations defining a cycloidal input.

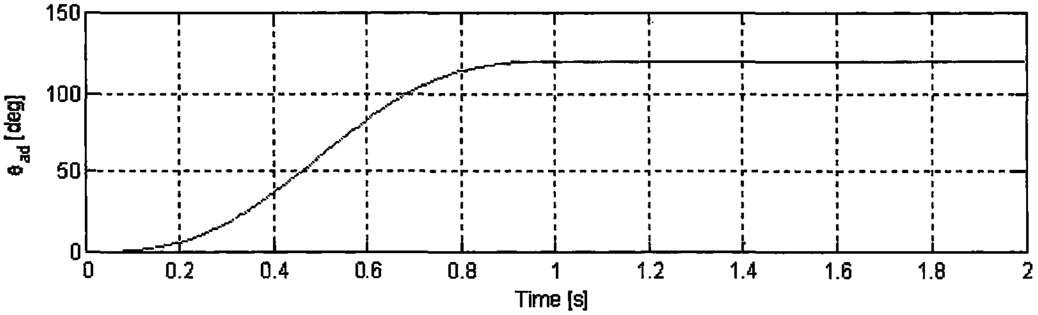

Figure 5.2.11: Positive direction cycloidal input

f. Cycloidal input (-120° in 1s, total test time 2s)

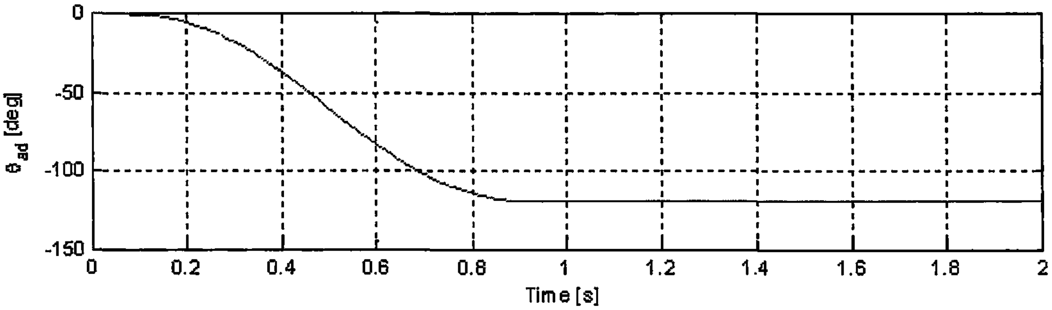

Figure 5.2.12: Negative direction cycloidal input

g. Mixed input (cycloidal 120° in 1s, rest 1s, cycloidal -120° in 1s, rest 0.5s, cycloidal 60° in 0.5s, rest 0.5s, cycloidal -60° in 0.5s, rest 1s, total test time 6s)

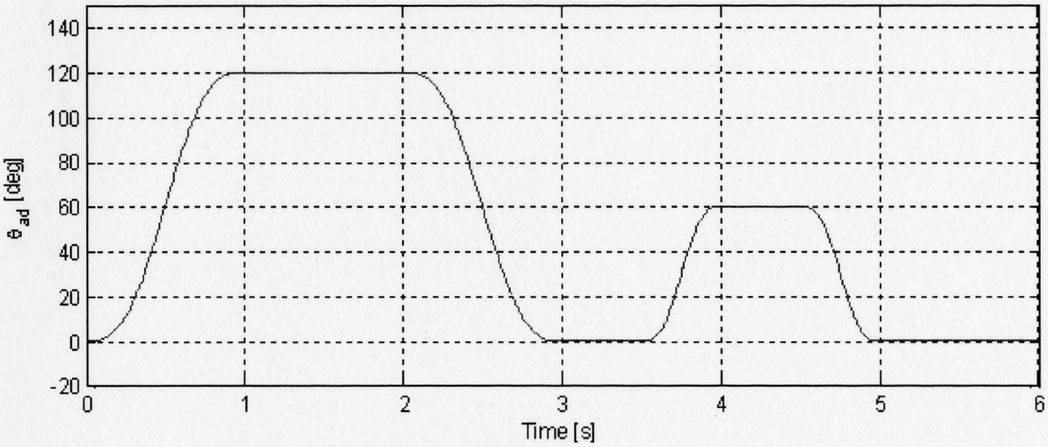

Figure 5.2.13: Mixed input

The ramp and cycloidal input tests are performed in both positive and negative directions as the performance of the system may be different due to the large difference in the friction in these two directions.

To obtain comparable and reliable results, the tests are performed with the following procedure:

- **Initial preload phase:** The preload cylinders move until the pressures in line 1 and 2 exceed 0.26 MPag. The preload pressure increases the stiffness of the system and assures that the pressure in the lines never drops below the 0.1 MPag where the effect of air bubbles in the tubing becomes significant.
- **Initial pressure adjustment phase:** The pump cylinders are fed according the trajectory starting direction to reduce the initial stick-slip phase as explained in section 5.2.4. This phase is followed by a 200 ms rest time.

- **Command and control phase:** the commanded input and control loops are included in this phase. The PID controller parameters are separately retuned for negative and positive directions, which in practice demonstrate better performance than a single set of PID parameters for both directions. Table 5.2.1 lists the PID parameters for positive and negative directions. The controller switches to the appropriate sets of parameters according to the direction of the rotation.

  Table 5.2.1: The PID controller parameters

	K_p	K_i	K_d
Negative	1.4	90	0.018
Positive	1.05	70	0.015

  A dither of ±1.2V, 250 Hz is added to the pump motor input, and error derivative filtering over 5 sampling periods[1] is included in the control loop of the program.

- **Final preload phase:** After the controlled motion completes, the preload cylinders move until the pressures in line 1 and line 2 drop bellow 0.06 MPag. This phase is for reducing the leakage effect when the system is not in use and at the same time maintains a positive pressure in the lines in order to prevent air from entering them.

Three numerical indicators are used to evaluate the performance of the system:

- **Steady state error (SSE):** which is the mean of residual error after transient period is finished, and is calculated for cycloidal inputs as an average of recorded data 200ms after cycloid period is finished, until the remainder of the test.

---

[1] Note that this corresponds to a low-pass filter cutoff frequency of 89 Hz. Since the closed-loop bandwidth will be approximately 5 Hz the delay from this filter will not produce significant performance degradation.

- **Root of the mean square error (RMSE):** which is defined as:

$$RMSE = \sqrt{\frac{1}{n}\sum_{i=1}^{n} e_i^{\,2}} \tag{5.2.5.1}$$

Where n is the number of data points, and e_i is the ith error calculated as the difference between desired and output arm angles. This indicator is calculated over the entire trajectory as *RMSE1*, and over the entire trajectory except for the first 0.25s as *RMSE2* (to exclude the effect of the initial stick-slip phase).

- **Maximum Error:** The maximum error expressed by the following equation is calculated over the entire test samples:

$$e_{\max} = \pm\max\left|(e_i)_{i=1}^{n}\right| \tag{5.2.5.2}$$

Each test is repeated 7 times to verify the repeatability of the results. The complete test results for all controllers are presented in section 5.4 to compare the performance of different controllers.

5.2.6 Experimental Results with PID Controller

The results of one test from the seven tests performed for each trajectory with the PID controller are plotted in Figures 5.2.14 to 5.2.20.

The mean RMSE1 and RMSE2 for the 7 tests conducted with ramp trajectory are 1.7° and 1.3° respectively for the positive ramp while for negative direction these indicators are 1.3° and 0.9° respectively. This may be explained by lower friction in negative direction. The mean maximum errors are ±5.1° and ±3.9° for positive and negative ramps respectively.

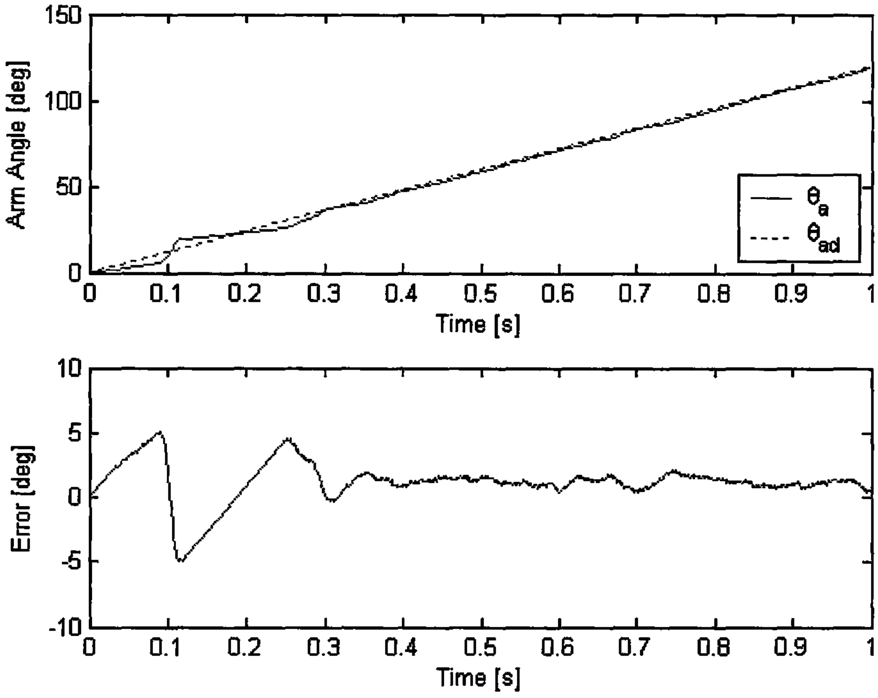

Figure 5.2.14: Positive direction ramp input (PID)

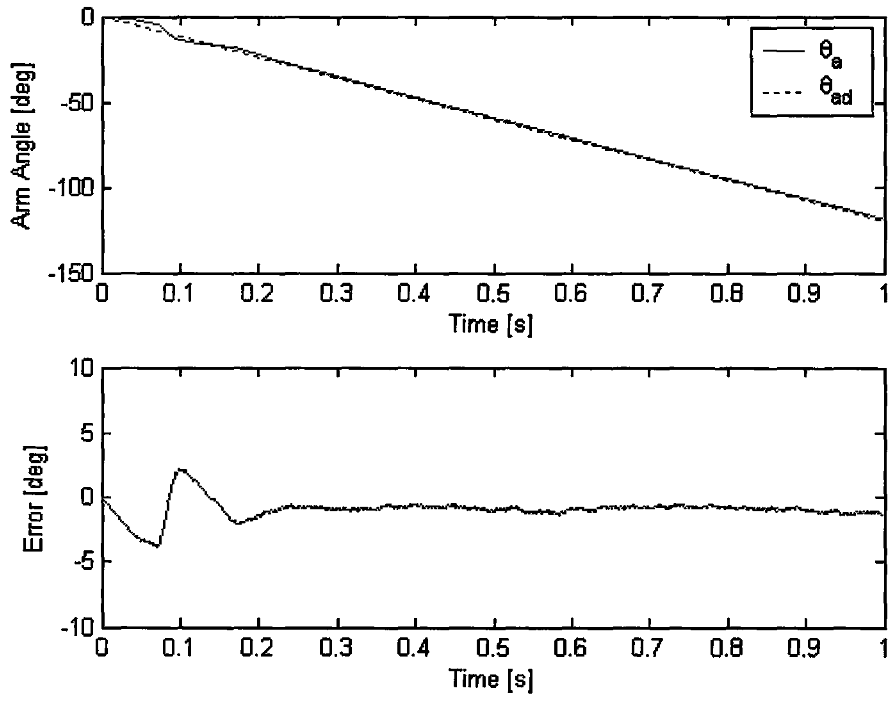

Figure 5.2.15: Negative direction ramp input (PID)

For sinusoidal trajectories, a large error may be observed in Figure 5.2.16 and 5.2.17 when the direction is changed. This may be explained in the same fashion as the initial pressure difference that was discussed in section 5.2.4. When the rotation direction is reversed, the friction is switched from sliding to static and the pressure difference should increase again to a certain threshold to overcome the static friction. Also the tracking error increases with the increase of sinusoidal input frequency. The mean RMSE1 and RMSE2 for the 7 tests conducted with sinusoidal trajectory are 2.3° and 2.3° for 0.5° Hz, and 3.7° and 3.8 for 1 Hz inputs. The difference between RMSE1 and RMSE2 is not significant due to the changing direction which causes the stick-slip phase to appear periodically. The mean maximum errors are ±7.7° and ±10.3° for 0.5 and 1 Hz sinusoidal input respectively.

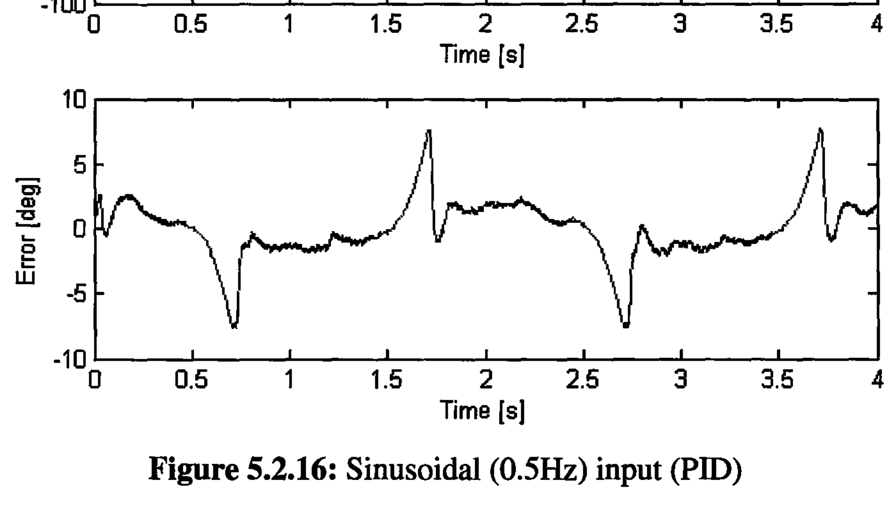

Figure 5.2.16: Sinusoidal (0.5Hz) input (PID)

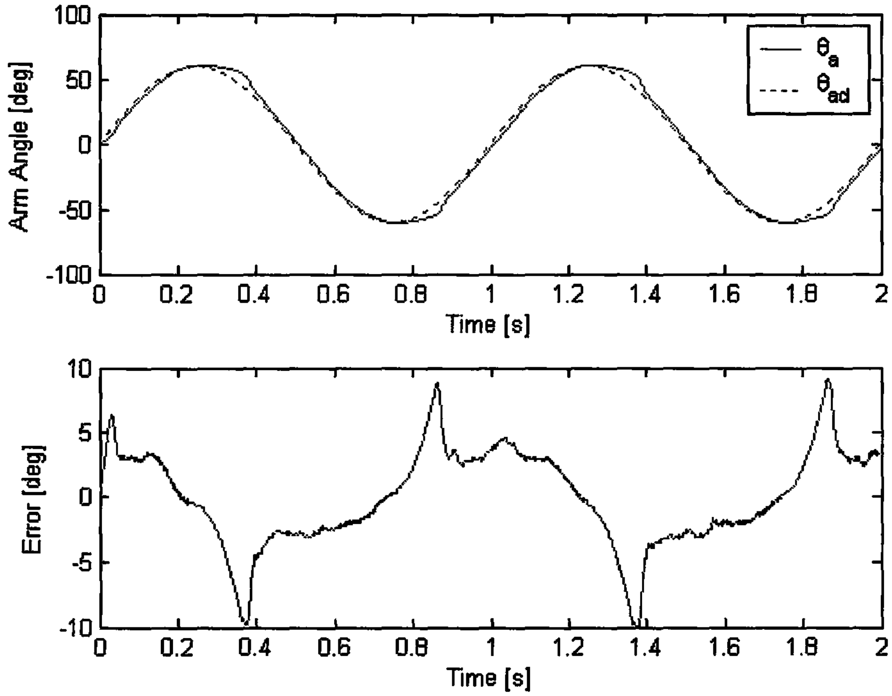

Figure 5.2.17: Sinusoidal (1 Hz) input (PID)

The cycloidal trajectories are used to evaluate the steady state error (SSE) of the system. The mean SSE for the 7 tests is ±0.2° and ±0.4° for positive and negative cycloidals respectively. The mean maximum errors are ±4.6° and ±3.5° for positive and negative directions which are about 10% lower than the corresponding ramp inputs due to the smoother start of the cycloidal.

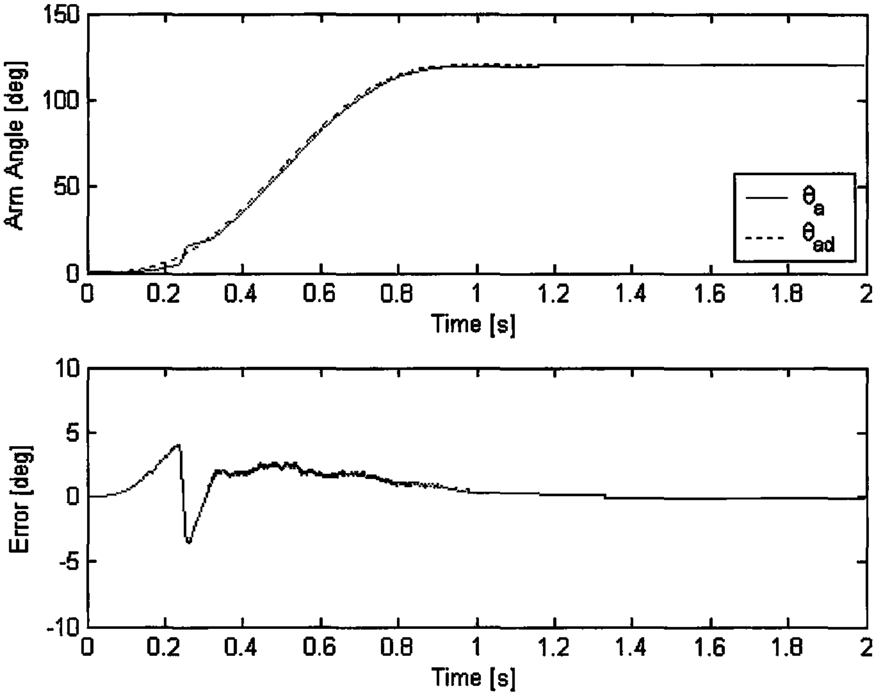

Figure 5.2.18: Positive direction cycloidal input (PID)

The mixed trajectory is used to evaluate the performance of the system to a changing amplitude and rest time in the input. As with the sinusoidal input, the difference between RMSE1 and RMSE2 (both are 1.7°) is not noticeable as a result of direction change which almost eliminates the effect of the initial 0.25 s of test compared to the entire test. The mean maximum error is 8.3°.

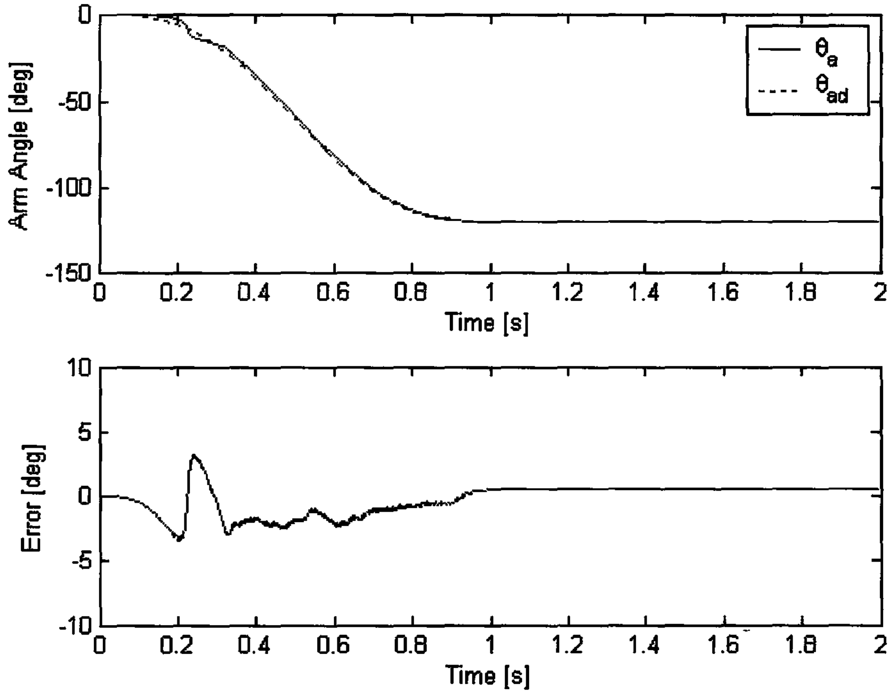

Figure 5.2.19: Negative direction cycloidal input (PID)

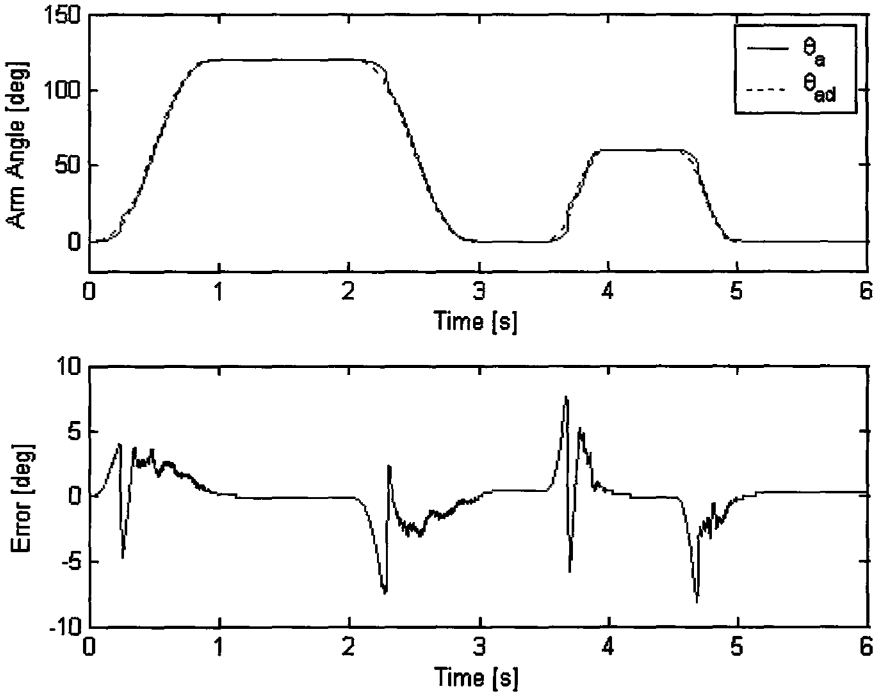

Figure 5.2.20: Mixed input (PID)

5.3 Model Based Feedforward (FFWD) + PID controller

The PID controller gains should be tuned so that the system does not overshoot and oscillate. This is more difficult in the presence of nonlinearities such as stick-slip friction. A solution to this problem may be adding a model based feedforward controller to the PID controller. Since the feedforward control output is calculated from the estimated model of the system, it is important that the model matches the dynamics of the system as closely as possible. The feedforward output should produce the major part of the controller signal to the pump motor while the PID controller should compensate for the residual error between the desired real arm angles.

5.3.1 Feedforward + PID Controller Design

Figure 5.3.1 illustrates the structure of the system with a FFWD + PID controller. The value of FFWD is calculated using the model parameters. This value shown as θ_f in Figure 5.3.1 is added to the scaled output of the PID controller.

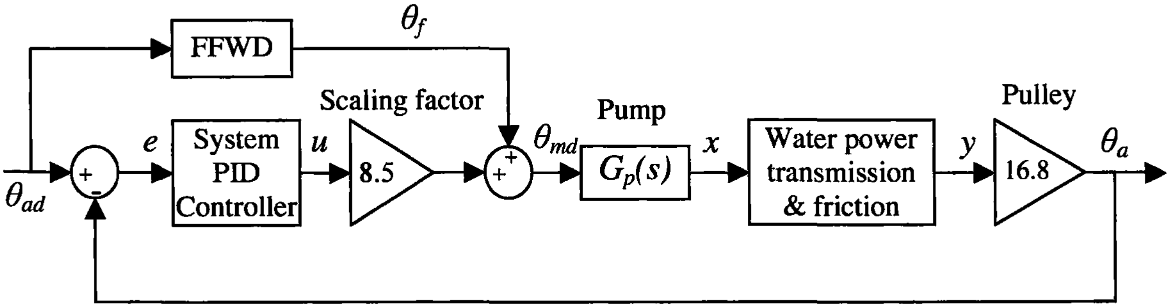

Figure 5.3.1: System block diagram with FFWD + PID controller

If θ_{ad} represent the desired arm angle of a known trajectory, then its first and second derivatives ($\dot{\theta}_{ad}$ and $\ddot{\theta}_{ad}$) are also known quantities. Using (3.6.4) and (4.5.1.1) the desired displacement of the joint cylinder piston (y) and its desired velocity and acceleration ($\dot{y}_d$ and $\ddot{y}_d$) are given by:

$$\begin{cases} y_d = \theta_{ad}/16.8 \\ \dot{y}_d = \dot{\theta}_{ad}/16.8 \\ \ddot{y}_d = \ddot{\theta}_{ad}/16.8 \end{cases} \tag{5.3.1.1}$$

Considering the direction of the desired trajectory the appropriate friction values may be substituted from (4.5.1.3) or (4.5.1.4) into (4.5.2.3) and the equations can be rearranged to calculate the desired output force from the rotary joint cylinders (F_{sumd}):

$$\begin{cases} F_{sumd} = sign(\theta_{ad}) \times F_S & \dot{y}_d = 0 \\ F_{sumd} = m\ddot{y}_d + sign(\dot{y}_d) \times (F_c + C_v|\dot{y}_d|) & \dot{y}_d \neq 0 \end{cases} \tag{5.3.1.2}$$

In section 4.4.3 the value of Δp/ΔV was experimentally derived and can be considered as a known parameter. Rearranging (4.4.3.16) and substituting ΔV from (4.4.3.15), the desired volume changes (ΔV_d) and desired pressures in line 1 and 2 (p_{1d} and p_{2d}) can be given by:

$$\begin{aligned} \Delta V_d &= \left(\frac{F_{sumd}}{A_2} - P_{1d(i-1)} + P_{2d(i-1)} \right) \Big/ \left(2\frac{\Delta P}{\Delta V} \right) \\ P_{1d(i)} &= P_{1d(i-1)} + \frac{\Delta P}{\Delta V} \times \Delta V_d \\ P_{2d(i)} &= P_{2d(i-1)} - \frac{\Delta P}{\Delta V} \times \Delta V_d \end{aligned} \tag{5.3.1.3}$$

Where indices *i* and *i-1* for desired pressures refers to the current and previous sampling periods respectively.

By letting $\Delta V = \Delta V_d$ in (4.4.3.15) and employing known values of y_d, the desired pump feed can be calculated:

$$\begin{cases} \Delta y_d = y_{d(i)} - y_{d(i-1)} \\ \Delta x_d = (\Delta V_d + \Delta y_d A_2)/A_1 \\ x_{d(i)} = x_{d(i-1)} + \Delta x_d \end{cases} \tag{5.3.1.4}$$

where x_d is the desired pump feed and indices i and i-1 indicate the current and previous samples.

Finally, the desired feedforward angle can be calculated from (4.3.1). Considering the input trajectories, the dynamic response of the pump motor is fast enough[1] to neglect the effect of the motor for the calculation of the FFWD value. Therefore, the FFWD angle (θ_f) is assumed to be directly estimated from the desired pump feed and the inverse of the pump ball screw lead which is 360°/mm, i.e.:

$$\theta_f = 360\, x_d \tag{5.3.1.5}$$

5.3.2 Feedforward + PID Controller Simulation

The FFWD+PID controller algorithm will be implemented in the simulation program introduced in section 4.6. The PID parameters are retuned in the simulation to the values listed in Table 5.3.1:

Table 5.3.1: The PID controller parameters used in the simulation

	K_p	K_i	K_d
Negative	1.14	55	0.018
Positive	1.03	47	0.015

---

[1] The bandwidth of the pump motor is 18 Hz. This is more than 10 times higher than the fastest input trajectory which is the 1 Hz sine wave.

The simulation result for a ramp input (trajectory "a") is depicted in Figure 5.3.2. The RMSE1 for this trajectory is 0.35° and the maximum error is ±2.24°. Comparing these values with the ones for the PID controller given in Figure 5.2.14 (RMSE1=1.7° and e_{max}=±5.1°), a major improvement can be predicted by employing a FFWD in addition to the PID controller.

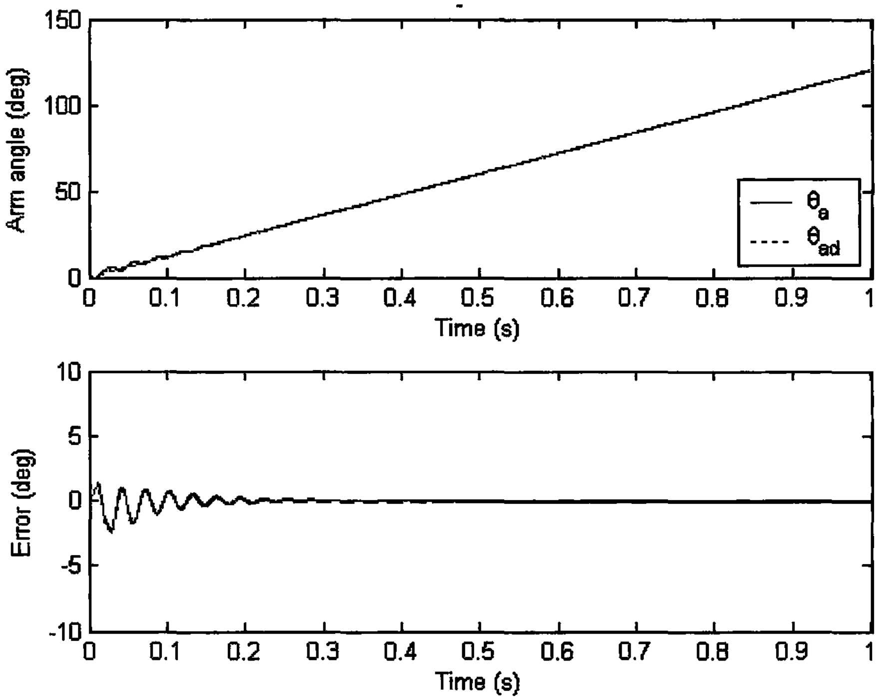

Figure 5.3.2: Positive direction ramp input simulation (FFWD+PID)

The simulation result for a sinusoidal input (trajectory "c") is plotted in Figure 5.3.3. The RMSE1 For this trajectory is 1.9° while the maximum error is ±7.6°. When compared to the experimental result with the PID controller given in Figure 5.2.17 (RMSE1=3.7°, and e_{max}=±10.3°), a promising improvement is expected when FFWD controller is added to the system control algorithm.

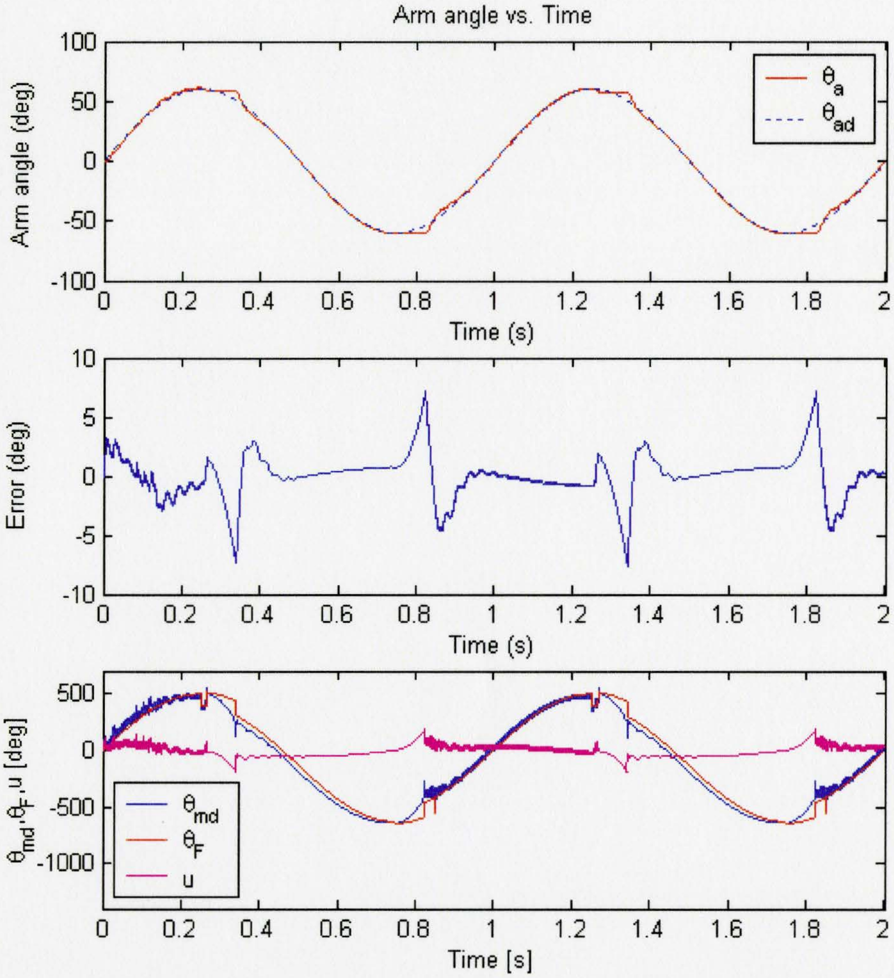

Figure 5.3.3: Sinusoidal (1 Hz) input simulation (FFWD+PID)

Studying the control signals it may be observed that the feedforward output, θ_f, contributes the major part of the controller signal, θ_{md}, and the PID controller only compensates for the remaining error between the desired and real arm angles.

5.3.3 Experimental Results with FFWD+PID Controller

The FFWD controller designed in section 5.3.1 has now been added to the system control program with the same PID gains tabulated in Table 5.2.1. The same trajectories for testing the PID controller are utilized for evaluating the performance of the

FFWD+PID controller. The results of one test from the seven tests performed for each trajectory with the FFWD+PID controller are plotted in Figures 5.3.4 to 5.3.10.

Figures 5.3.4 and 5.3.5 present the experimental results for positive and negative direction ramp trajectories. The mean RMSE1 and RMSE2 for the 7 tests conducted with ramp trajectory are 1.1° and 0.2° respectively for the positive ramp while for negative direction these indicators are 0.7° and 0.2° respectively. The mean maximum errors are ±4.3° and ±2.7° for positive and negative ramps respectively.

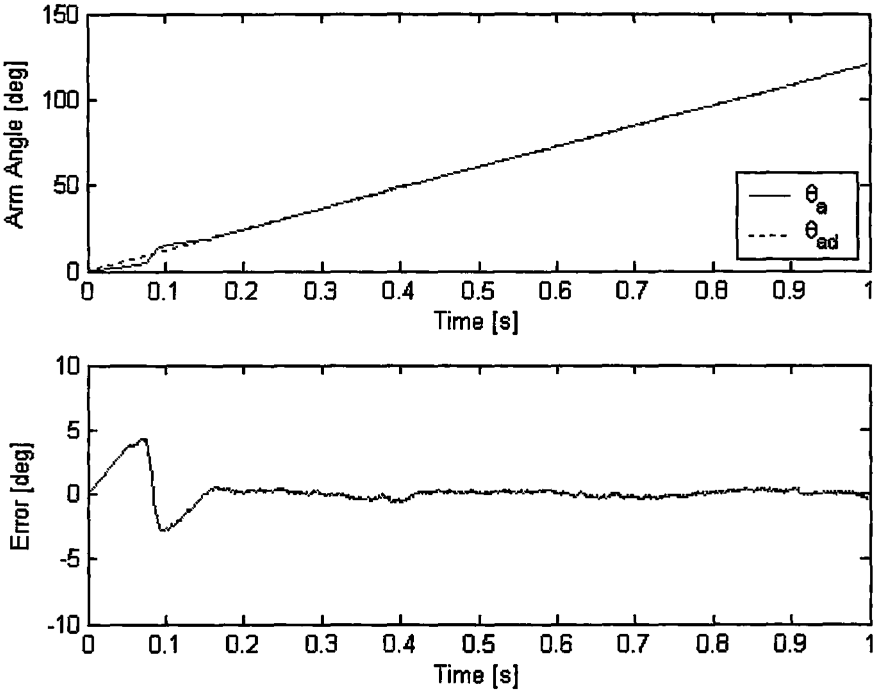

Figure 5.3.4: Positive direction ramp input (FFWD+PID)

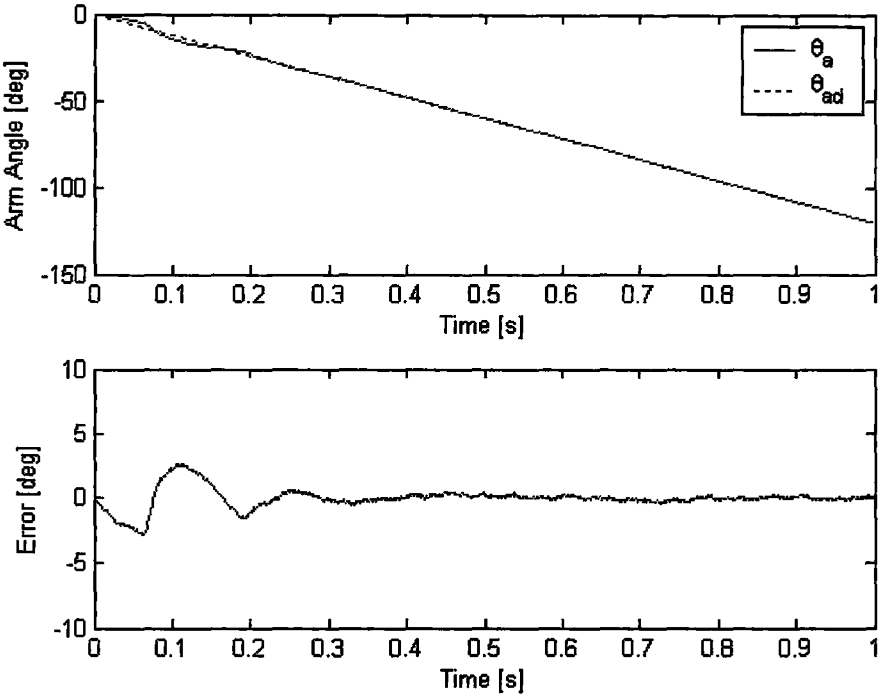

Figure 5.3.5: Negative direction ramp input (FFWD+PID)

Compared with the PID controller, the tracking error is significantly reduced which is particularly noticeable in the value of RMSE2 (85% and 78% improvement for positive and negative directions respectively). The maximum errors are also improved by 16% and 31% in both the positive and negative direction ramps.

Typical responses of the system to sinusoidal inputs of 0.5 Hz and 1 Hz are depicted in Figures 5.3.6 and 5.3.7 for the FFWD+PID controller. The RMSE1 and RMSE2 are reduced by 43% and 51% for 0.5 Hz and 1 Hz inputs. As with the PID controller there is almost no difference between RMSE1 and RMSE2 due to the repeated stiction. Compared with the PID controller, the maximum errors are improved by 26% and 33% for 0.5 and 1 Hz inputs accordingly.

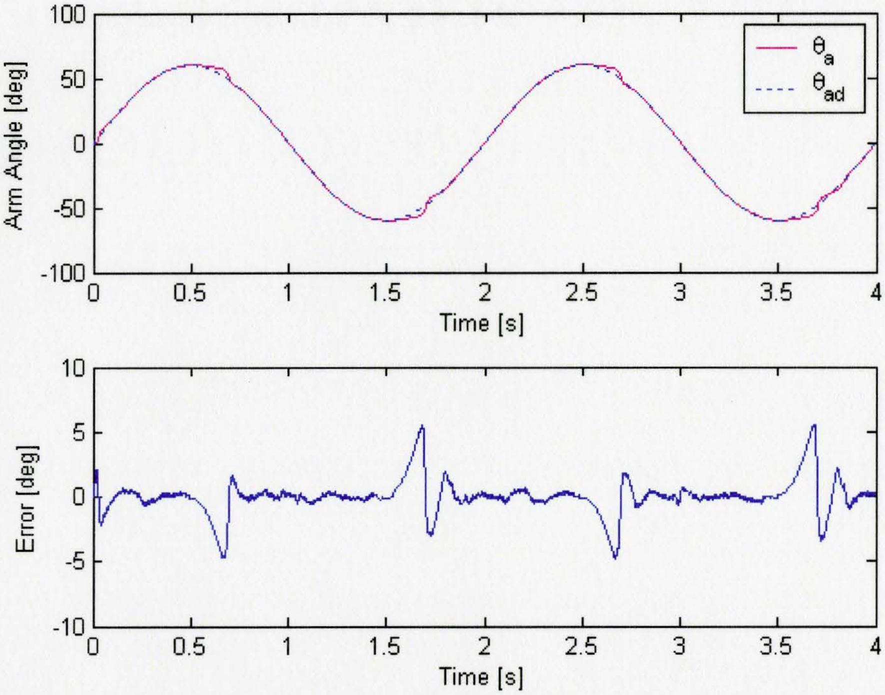

Figure 5.3.6: Sinusoidal (0.5Hz) input (FFWD+PID)

The feedforward signal is increased by 23% before adding to the PID signal. As one can see in Figure 5.3.7, again the feedforward term contributes in the major portion of the final control signal applied to the pump motor. Note that in calculating the feedforward term the static part of the friction in equation 5.3.1.2 is not included and only the positive direction values have been used for the sliding and viscous frictions.

Figures 5.3.8 and 5.3.9 demonstrate typical outputs for cycloidal trajectories in the positive and negative directions. The outputs are smoother in presence of FFWD+PID controller compared with the PID controller. The RMSE1 and RMSE2 are also improved 23% and 33% in positive direction and 45% and 60% in negative direction. The maximum error is not improved. In fact the mean of maximum error is increased by more than 20% in positive direction.

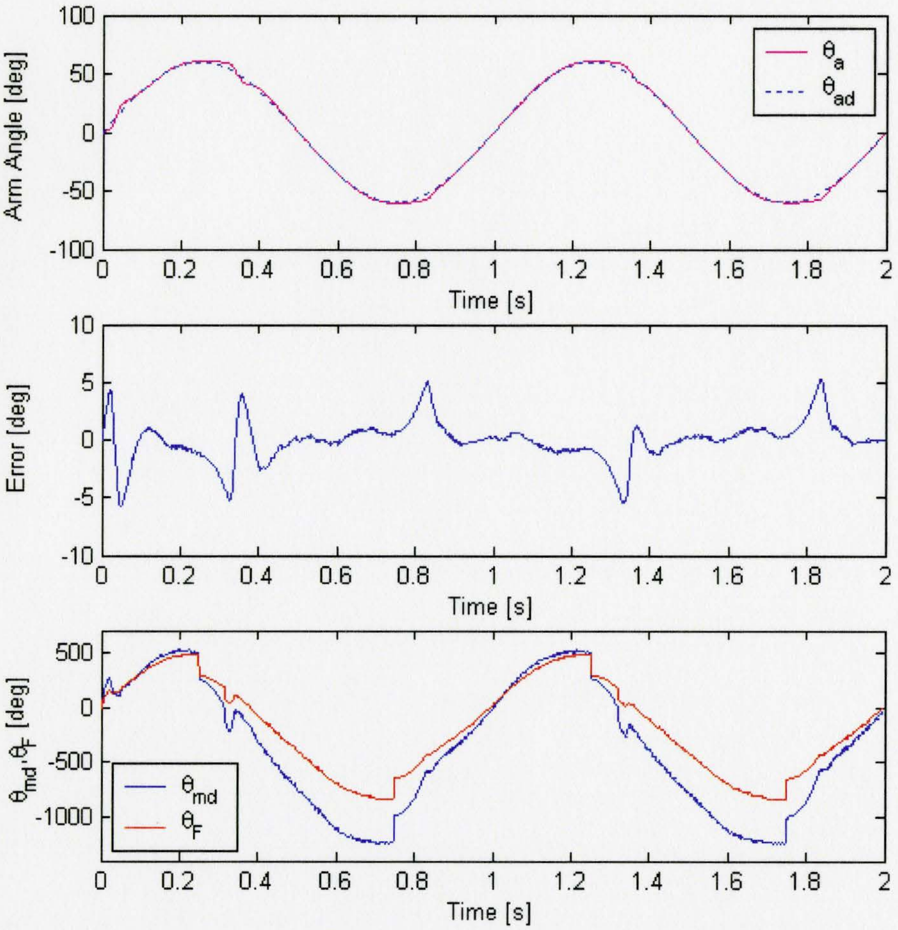

Figure 5.3.7: Sinusoidal (1Hz) input (FFWD+PID)

The SSE values have been already in a very good range with PID controller (±0.2° and ±0.4° in positive and negative directions), and no major change is observed in this indicator.

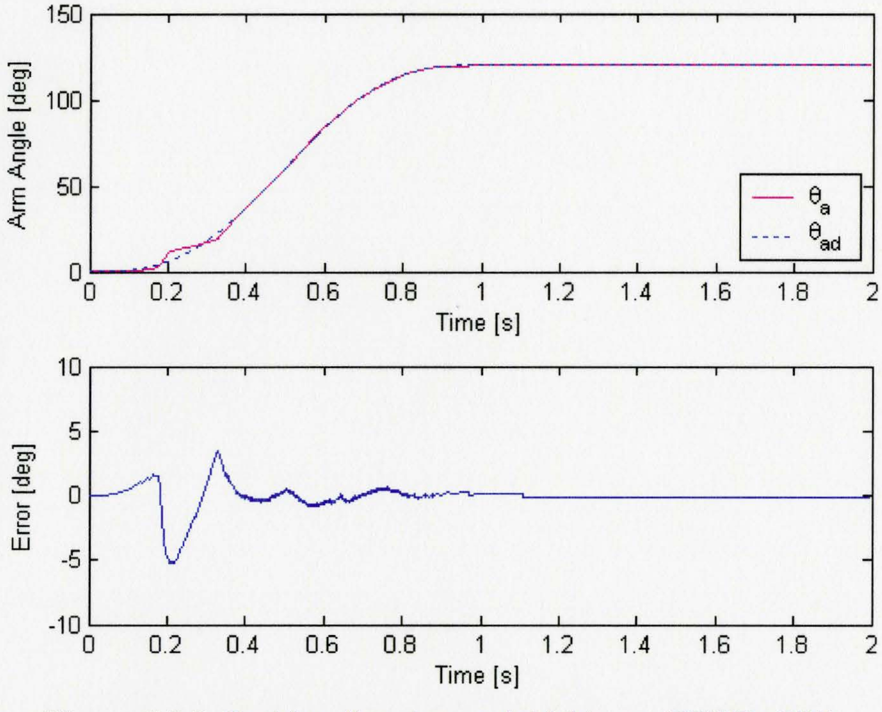

Figure 5.3.8: Positive direction cycloidal input (FFWD+PID)

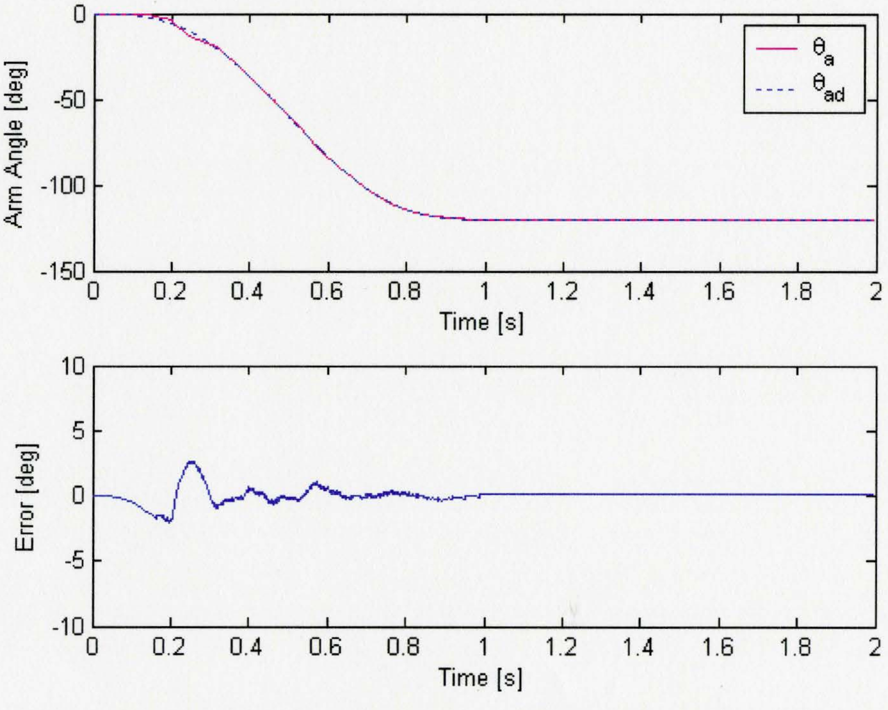

Figure 5.3.9: Negative direction cycloidal input (FFWD+PID)

A typical system response to a mixed input with the FFWD+PID controller is shown in Figure 5.3.10. The mean RMSE1 and RMSE2 are equal to 0.9° which demonstrate an improvement of 47% compared to the PID controller. The mean maximum error is also cut by 25%.

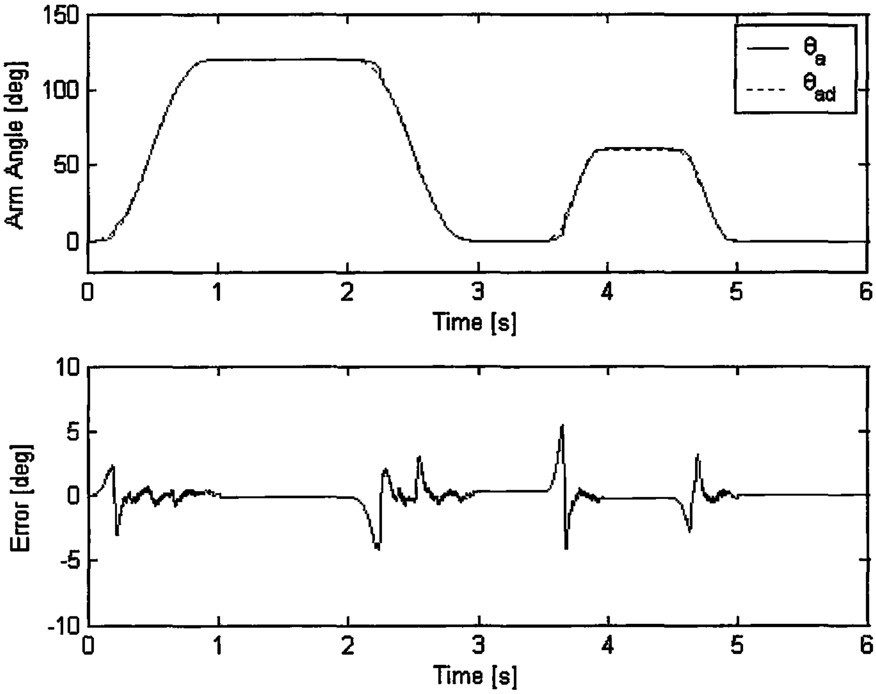

Figure 5.3.10: Mixed input (FFWD+PID)

5.4 Detailed Results for PID Controller vs. FFWD+PID Controller

Table 5.4.1 lists the values of RMSE1, RMSE2, and e_{max} for positive and negative cycloidal trajectories in presence of PID or FFWD+PID controllers. The mean value is the average of a numerical indicator and the standard deviation shows the level of the certainty of that indicator. Table 5.4.2 shows the SSE values for positive and negative direction cycloids with PID or FFWD+PID controllers.

Table 5.4.1: RMSE and e_{max} with PID or FFWD+PID controller

Trajectory		Controller		Test #1	Test #2	Test #3	Test #4	Test #5	Test #6	Test #7	Mean	Std. Dev.
		PID	FFWD+PID	RMSE1 RSME2 $\lvert e_{max}\rvert$	RMSE1 RSME2 $\lvert e_{max}\rvert$	RMSE1 RSME2 $\lvert e_{max}\rvert$	RMSE1 RSME2 $\lvert e_{max}\rvert$	RMSE1 RSME2 $\lvert e_{max}\rvert$	RMSE1 RSME2 $\lvert e_{max}\rvert$	RMSE1 RSME2 $\lvert e_{max}\rvert$	RMSE1 RSME2 $\lvert e_{max}\rvert$	RMSE1 RSME2 $\lvert e_{max}\rvert$
1	Ramp (+)	✓		1.5	1.4	2.0	1.7	1.8	1.7	1.7	1.7	0.17
				1.2	1.2	1.5	1.3	1.3	1.3	1.3	1.3	0.08
				4.9	4.3	5.1	5.4	5.4	5.3	5.1	5.1	0.34
			✓	1.1	0.8	1.0	1.1	1.1	1.2	1.1	1.1	0.11
				0.3	0.3	0.2	0.2	0.2	0.2	0.2	0.2	0.02
				4.7	3.8	4.3	4.1	4.1	4.6	4.4	4.3	0.28
2	Ramp (-)	✓		1.3	1.2	1.1	1.3	1.2	1.4	1.4	1.3	0.10
				1.0	0.9	0.8	0.9	0.9	0.9	0.9	0.9	0.05
				4.6	3.3	3.0	4.0	3.9	4.3	4.4	3.9	0.53
			✓	0.7	0.8	0.8	0.6	0.8	0.4	0.6	0.7	0.13
				0.2	0.2	0.2	0.2	0.2	0.2	0.2	0.2	0.03
				2.6	2.7	3.4	2.5	2.8	2.0	2.7	2.7	0.39
3	Sinusoidal (0.5Hz)	✓		2.3	2.3	2.3	2.2	2.2	2.2	2.2	2.3	0.03
				2.3	2.3	2.3	2.3	2.2	2.3	2.2	2.3	0.03
				7.8	7.9	7.7	7.8	7.5	7.6	7.5	7.7	0.16
			✓	1.2	1.1	1.3	1.2	1.6	1.5	1.3	1.3	0.15
				1.2	1.2	1.4	1.2	1.6	1.5	1.3	1.3	0.15
				5.3	4.8	5.5	4.9	6.6	5.5	5.6	5.5	0.54
4	Sinusoidal (1Hz)	✓		3.6	3.7	3.6	3.9	3.6	3.8	3.8	3.7	0.12
				3.7	3.9	3.7	4.1	3.7	3.9	3.9	3.8	0.12
				10.0	10.3	10.3	10.3	10.0	10.1	10.8	10.3	0.26
			✓	2.2	1.8	1.7	1.8	1.8	1.8	1.7	1.8	0.16
				1.9	1.7	1.6	1.8	2.0	1.8	1.6	1.8	0.12
				10.2	6.0	5.8	6.3	7.0	6.4	6.8	6.9	1.39
5	Cycloid (+)	✓		1.2	1.2	1.3	1.2	1.3	1.9	1.2	1.3	0.22
				1.1	1.1	1.2	1.1	1.2	1.9	1.2	1.2	0.25
				4.5	4.0	3.9	4.1	4.1	7.5	3.9	4.6	1.21
			✓	1.0	0.9	1.1	1.0	0.8	1.1	1.3	1.0	0.16
				0.8	0.6	0.9	0.6	0.6	0.8	1.3	0.8	0.24
				5.6	4.9	6.5	5.2	4.2	5.7	7.8	5.7	1.09
6	Cycloid (-)	✓		1.0	1.1	1.3	1.2	1.0	1.2	1.1	1.1	0.12
				1.0	1.0	1.2	1.1	0.9	1.1	1.0	1.0	0.11
				2.8	3.1	4.6	3.4	3.5	3.9	3.5	3.5	0.53
			✓	0.9	0.7	0.7	0.5	0.6	0.5	0.4	0.6	0.15
				0.6	0.6	0.5	0.4	0.5	0.4	0.2	0.4	0.13
				4.9	3.5	3.5	2.7	2.8	2.0	2.9	3.2	0.85
7	Mixed	✓		1.5	1.7	1.9	1.7	1.8	1.8	1.7	1.7	0.11
				1.5	1.7	1.9	1.7	1.7	1.7	1.7	1.7	0.11
				6.8	8.7	8.4	8.9	8.1	8.6	8.8	8.3	0.67
			✓	1.1	1.0	0.9	0.9	0.9	1.0	0.9	0.9	0.08
				1.0	1.0	0.8	0.9	0.8	0.9	0.8	0.9	0.08
				6.4	6.8	6.4	6.7	5.4	5.8	5.7	6.2	0.50

Table 5.4.2: SSE with PID or FFWD+PID controller

Trajectory		Controller		Test #1	Test #2	Test #3	Test #4	Test #5	Test #6	Test #7	Mean
		PID	FFWD+PID								
1	Cycloid (+)	✓		-0.1	-0.1	-0.3	-0.1	-0.4	-0.1	-0.1	-0.2
			✓	-0.1	-0.1	-0.1	-0.1	-0.1	-0.3	-0.1	-0.2
2	Cycloid (-)	✓		0.4	0.4	0.4	0.6	0.2	0.6	0.4	0.4
			✓	0.4	0.1	0.4	0.1	0.5	-0.1	0.1	0.2

Examination of the values of RMSE and e_{max} in Table 5.4.1 reveals that, in general, the addition of a model based FFWD controller has enhanced the performance of the system. The greatest effect may be observed in the tracking error after stiction phase is overcome. The maximum error which happens after stiction is overcome, although less than tracking error, is reduced in almost all cases by more than 20%.

The steady state error measured by SSE (Table 5.4.2) demonstrates similar range for both PID and FFWD+PID controllers with a mean value of less than ±0.5° (less than 0.4% of the total rotation of ±120° in cycloidal inputs).

5.5 Evaluation of the System Robustness

When a controller is designed based on the system model, there will be some level of uncertainty due to the differences between the true system and the nominal model used for design. The controller should be able to cope with initial differences and also unexpected changes during the system activity. To test and compare the robustness of PID and FFWD+PID controllers, a payload mass is added to the end of the arm. For horizontal rotation this payload adds a constant moment of inertia. The payload is a small piece of brass with a mass of $M_{load} = 8.5$ g located at a distance of 20 mm to the center of rotation. Compared to the distributed load of the arm having a mass of about 0.32 g, this mass can be considered as a point load acting at a distance from center of rotation (see Figure 5.5.1)

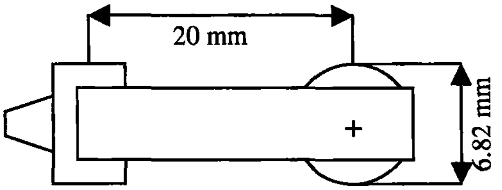

Figure 5.5.1: Position of the point load on the rotation arm

The mass moment of inertia of this payload about the center of the pulley (J_{load}) and consequently the effective mass of the added mass (m_{load}) from (4.5.2.1) will be:

$$\begin{aligned} J_{load} &= M_{load} \times 20^2 = 3400\, gmm^2 \\ m_{load} &= \frac{J_{load}}{r_p^{\ 2}} = \frac{3400}{(6.82/2)^2} = 292g \end{aligned} \qquad (5.5.1)$$

Comparing this effective mass with the one calculated in section 4.5.2 (18.5 g), the new mass represents significant change (i.e. an increase of about 1480%) which is not included in the system model. Figures 5.5.2 to 5.5.7 illustrate one of the results from the seven tests for each of the three trajectories (0.5 Hz sinusoidal, positive and negative cycloids) for the PID and FFWD+PID controllers. The results for all tests are listed in Table 5.5.1 for RMSE and e_{max}, and in Table 5.5.2 for SSE. The results with FFWD+PID controller compared to PID controller shows that the mean RMSEs are improved by 40%, 33%, and 50% for sinusoidal, positive and negative cycloidal inputs respectively. The mean e_{max} is also enhanced by 23% and 18% for sinusoidal and negative cycloidal input while for positive cycloidal input it is degraded by 35%.

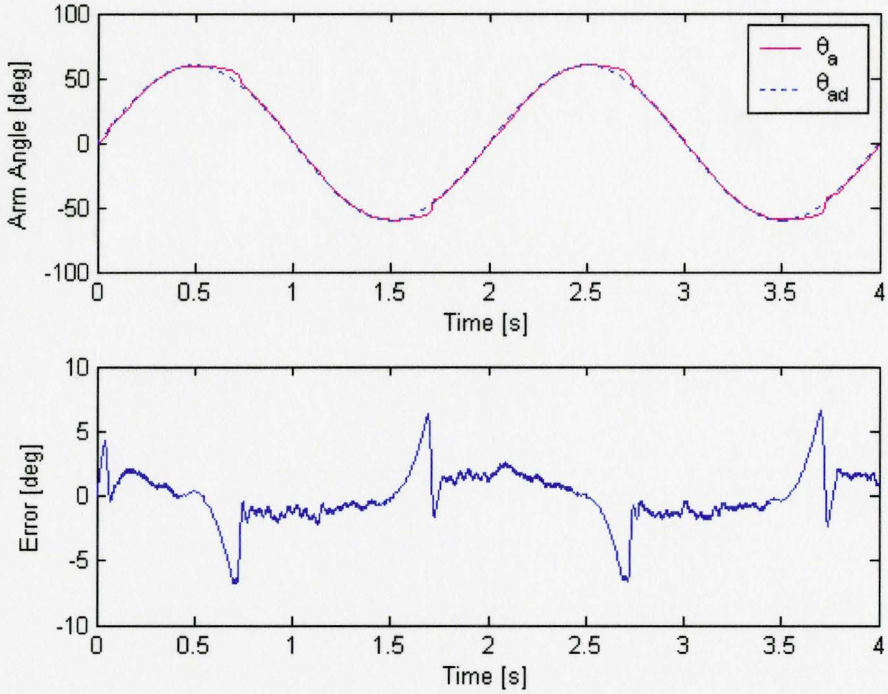

Figure 5.5.2: Sinusoidal (0.5Hz) input with extra load (PID)

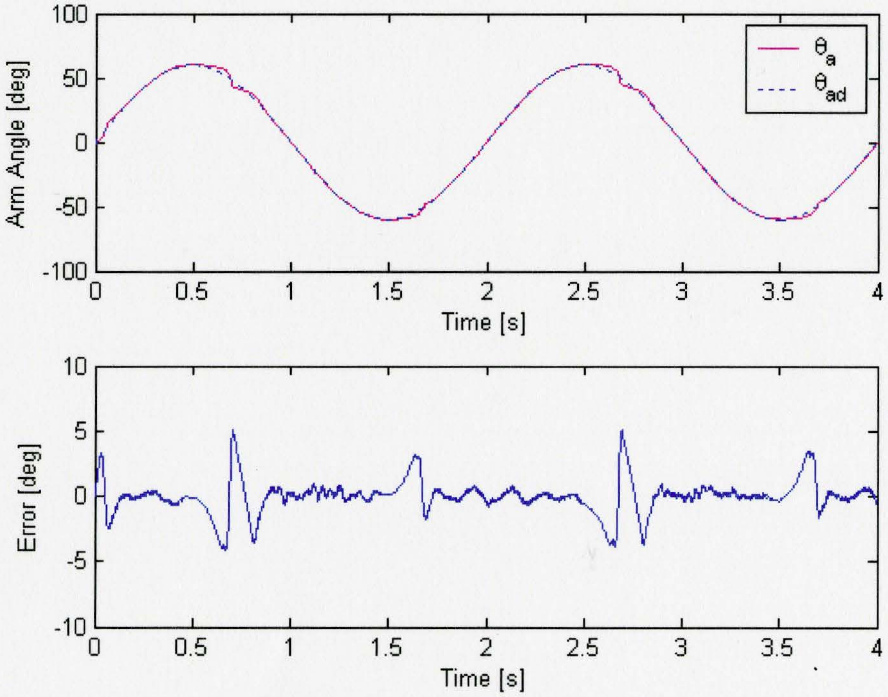

Figure 5.5.3: Sinusoidal (0.5Hz) input with extra load (FFWD+PID)

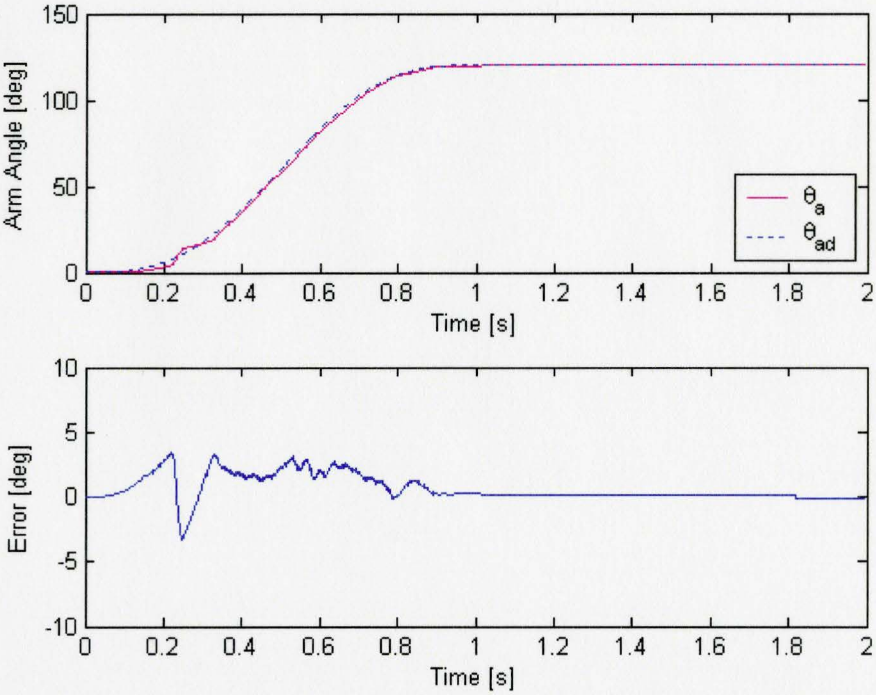

Figure 5.5.4: Positive direction cycloidal input with extra load (PID)

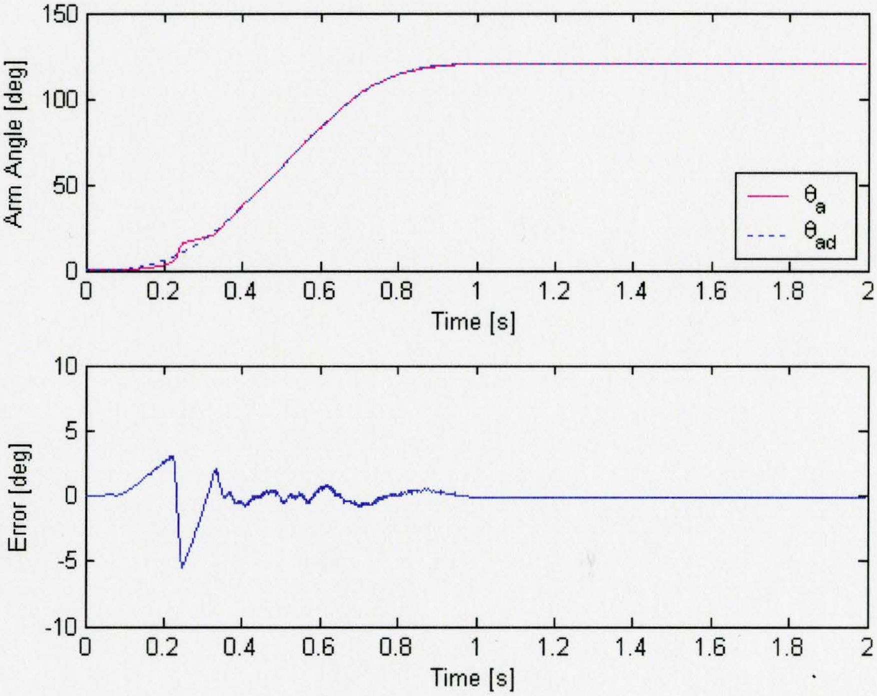

Figure 5.5.5: Positive direction cycloidal input with extra load (FFWD+PID)

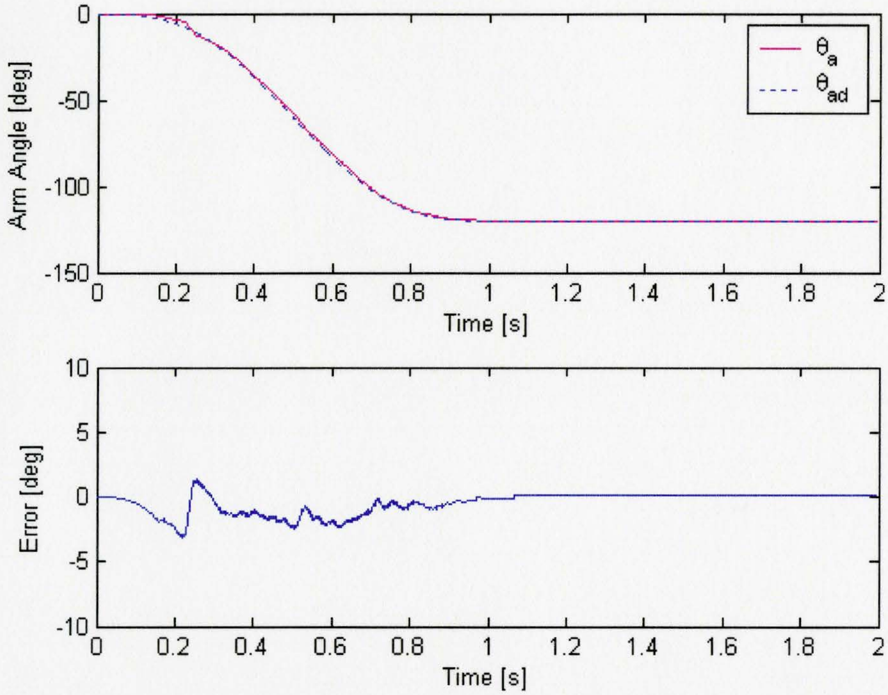

Figure 5.5.6: Negative direction cycloidal input with extra load (PID)

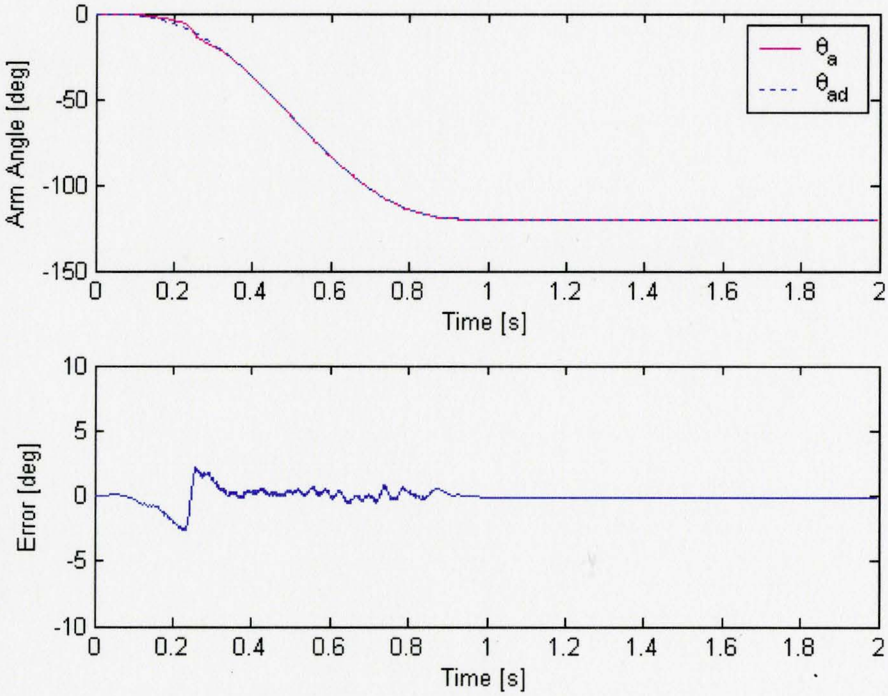

Figure 5.5.7: Negative direction cycloidal input with extra load (FFWD+PID)

In the horizontal position test, an extra load acts as a constant non-modelled inertia in the system. If the same setup is positioned vertically, then a changing extra force which is not included in the model will be applied on the system. Figure 5.5.8 shows the configuration of the vertically positioned rotary joint setup.

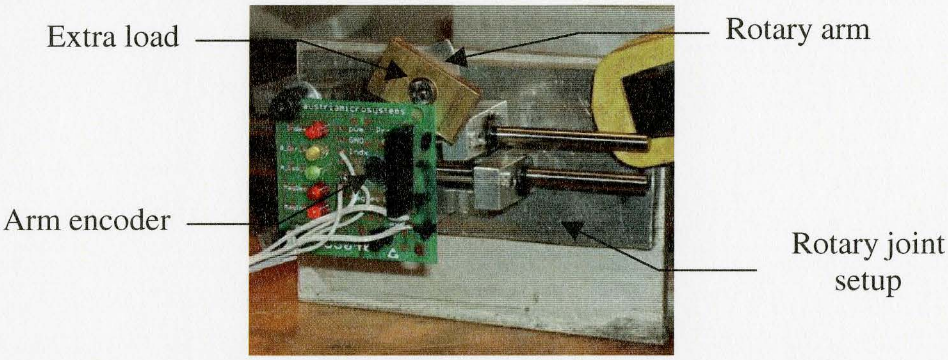

Figure 5.5.8: Vertically positioned rotary joint setup

The extra load generates a changing force on the rotary joint sliders as illustrated in Figure 5.5.9. This force may change from zero to about 0.49 N depending on the arm angle. If the maximum pressure difference between line 1 and 2 is considered to be 0.6 MPa, knowing that the rotary joint cylinder bore area (A_2) equals to $12.6\text{x}10^{-6}$ mm^2, the maximum force on the sliders will be 0.6 x 12.6 = 7.56 N. Therefore the extra load can exerts a disturbance of 0.49 N or 6.5% of the maximum force.

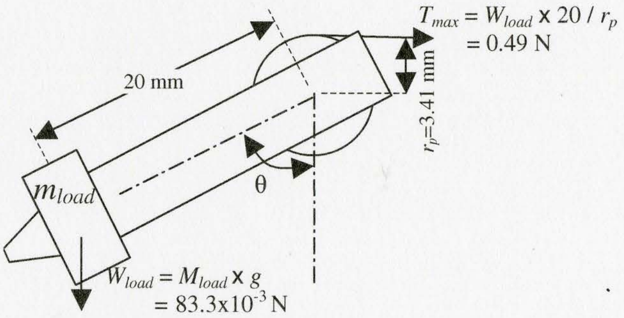

Figure 5.5.9: Changing load due to vertical positioning of rotary joint

Figures 5.5.10 to 5.5.17 illustrates one of the results from 7 tests for each of the four trajectories (0.5 Hz sinusoidal, positive and negative cycloidals, and mixed input) with the PID or FFWD+PID controller. The results for all tests are listed in Table 5.5.1 for RMSE and e_{max}, and in Table 5.5.2 for SSE. The results with FFWD+PID controller compared to the PID controller demonstrate that the mean RMSEs are improved by 50%, for all of the trajectories except for the sinusoidal input which has been improved by 22%. The mean e_{max} is enhanced by 18% and 35% for mixed and negative cycloidal input while for positive cycloidal and sinusoidal inputs it is degraded by 17.5% and 24%.

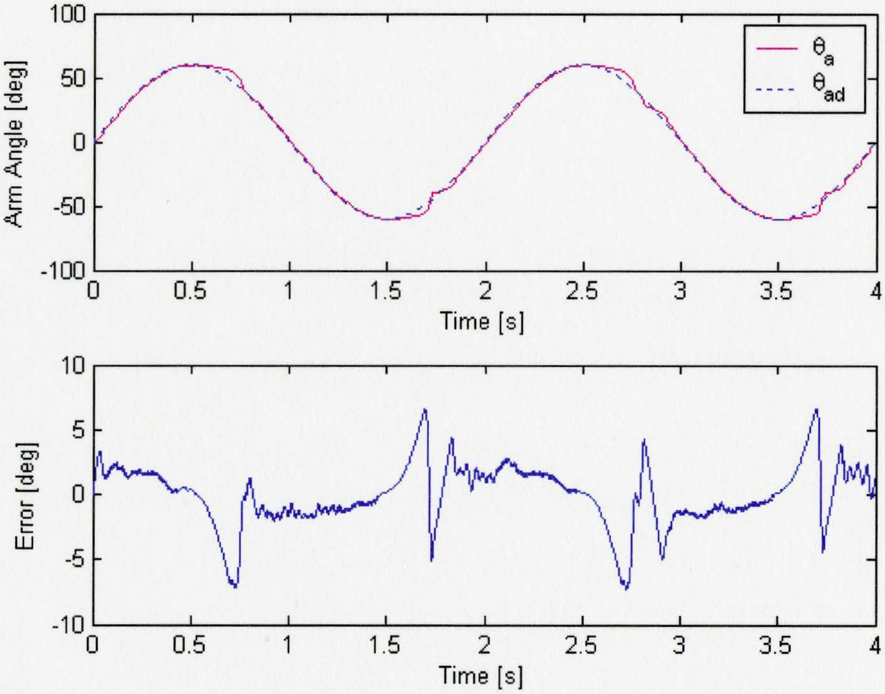

Figure 5.5.10: Sinusoidal (0.5Hz) input with extra load, vertically position (PID)

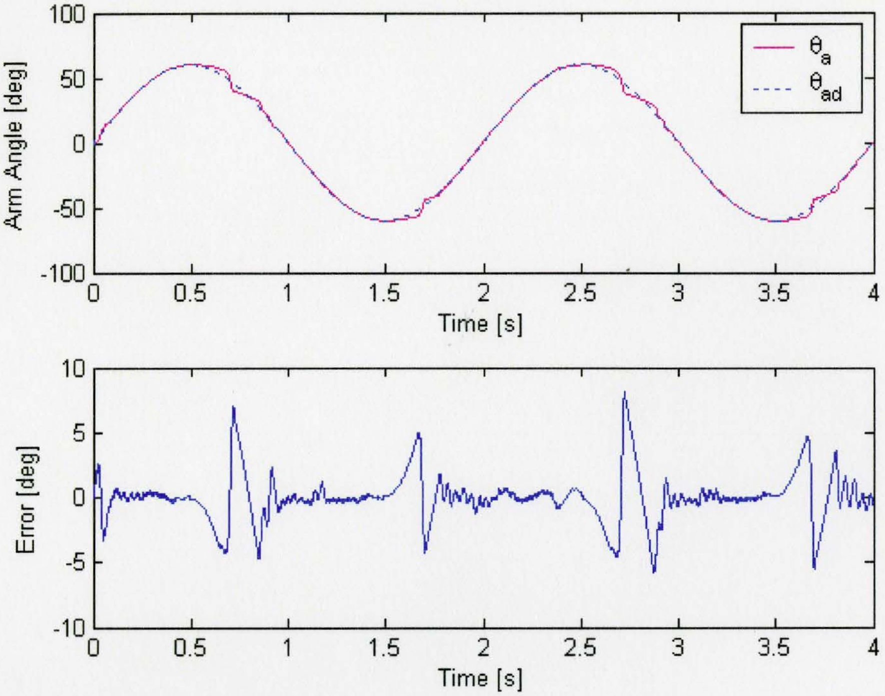

Figure 5.5.11: Sinusoidal (0.5Hz) input with extra load, vertically position (FFWD+PID)

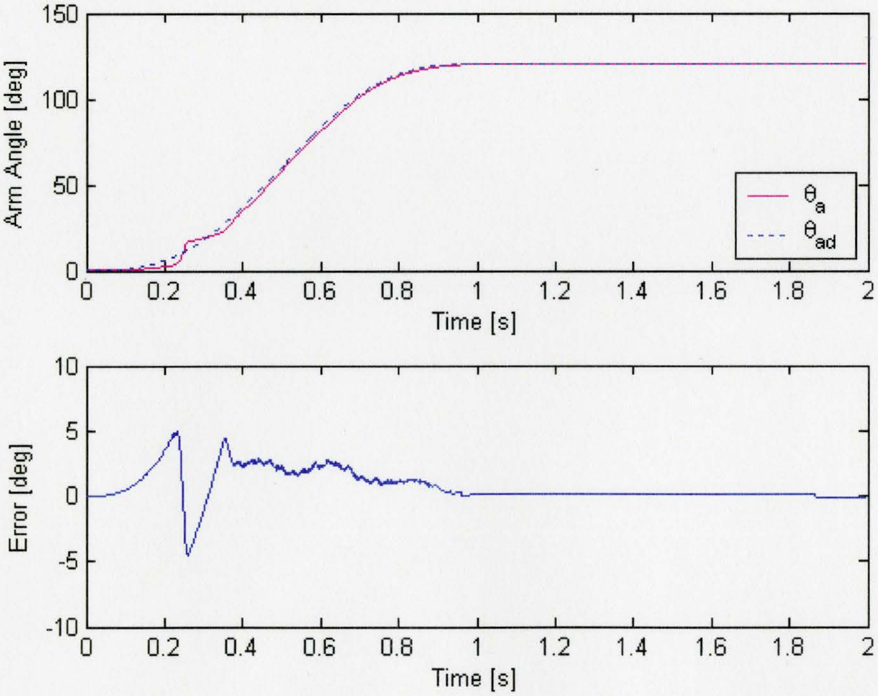

Figure 5.5.12: Positive direction cycloidal input with extra load, Vertical (PID)

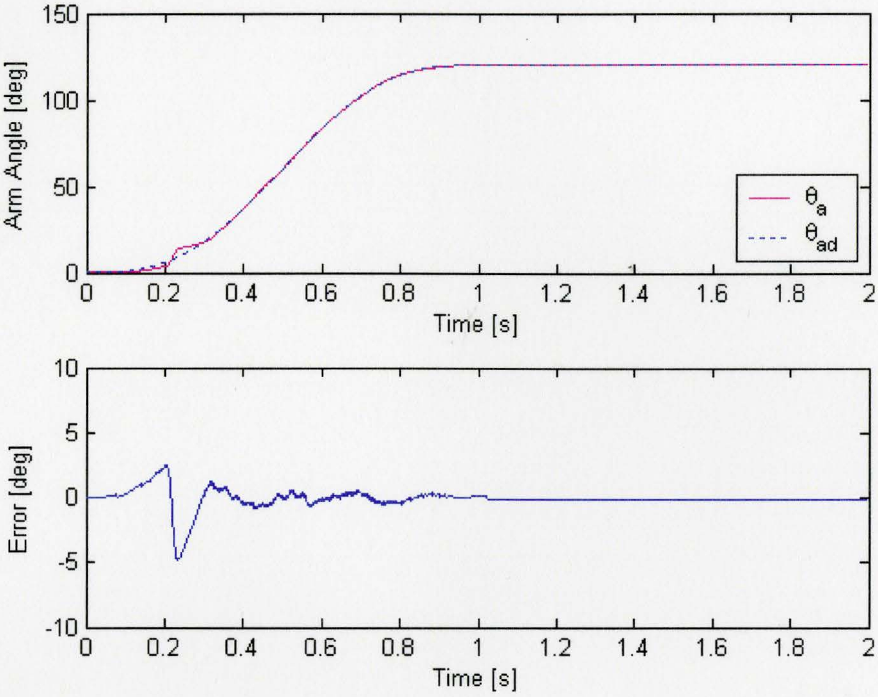

Figure 5.5.13: Positive direction cycloidal input with extra load, Vertical (FFWD+PID)

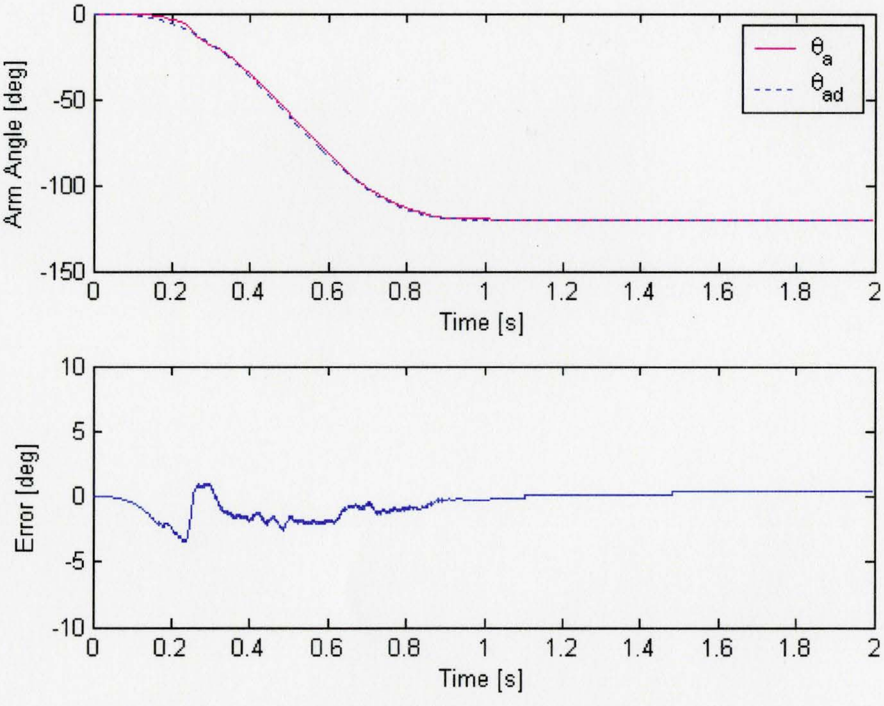

Figure 5.5.14: Negative direction cycloidal input with extra load, Vertical (PID)

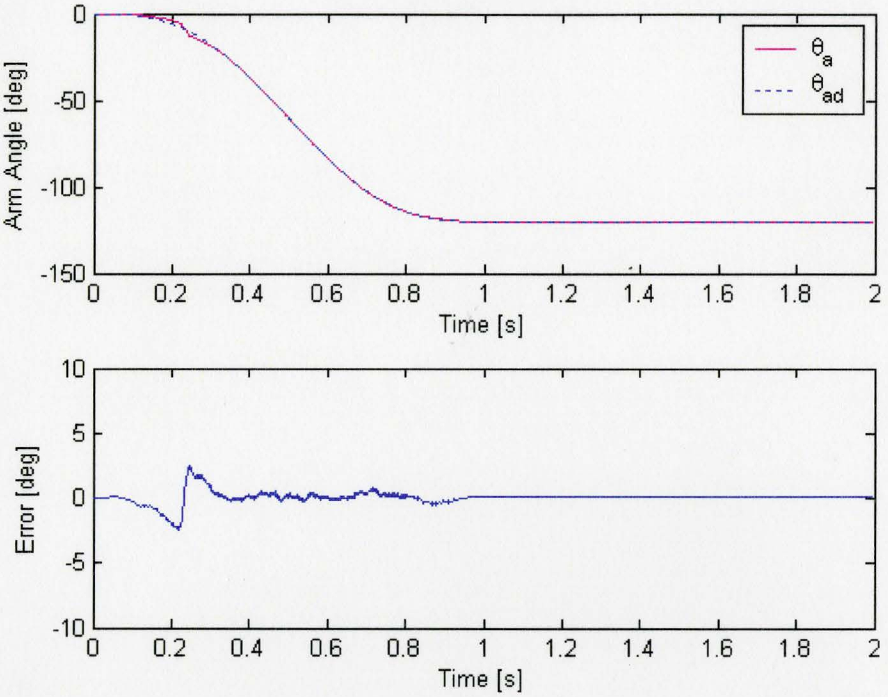

Figure 5.5.15: Negative direction cycloidal input with extra load, Vertical (FFWD+PID)

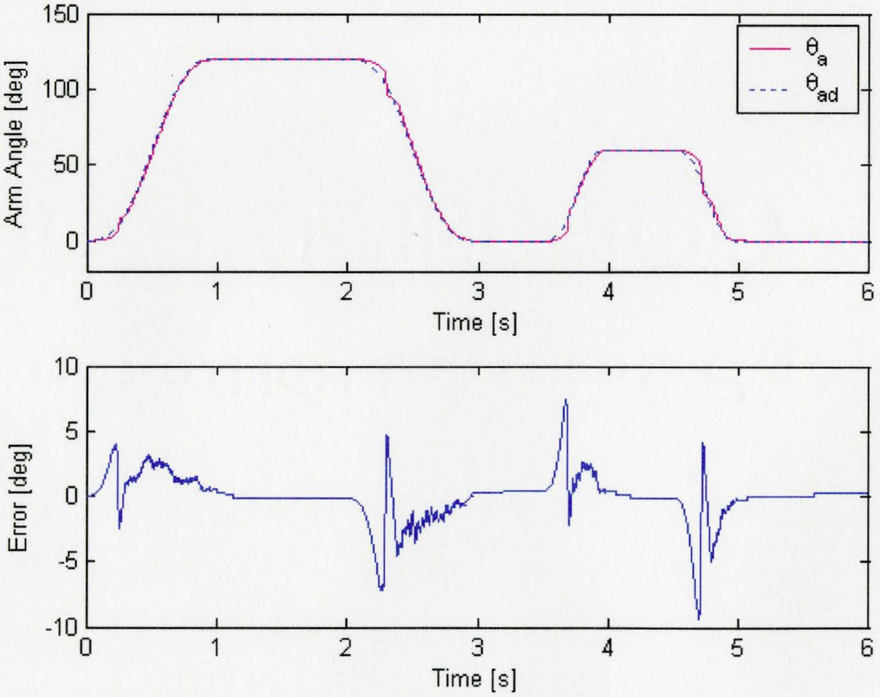

Figure 5.5.16: Mixed input with extra load, Vertical (PID)

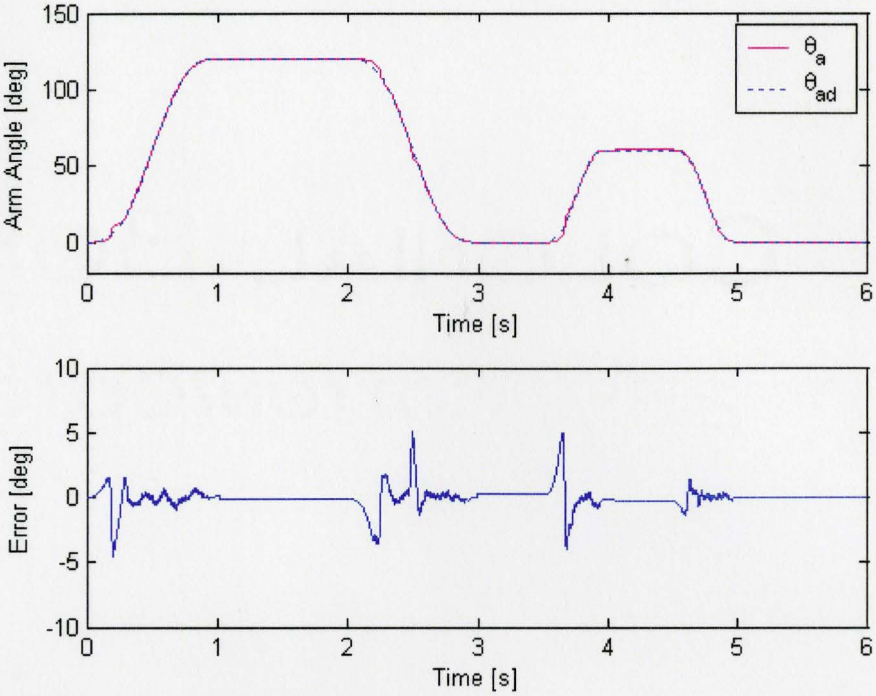

Figure 5.5.17: Mixed input with extra load, Vertical (FFWD+PID)

Table 5.5.3 summarizes the results of Table 5.4.1, 5.4.2, 5.5.1, and 5.5.2 for the mean values of RMSE1, RMSE2, e_{max}, and SSE. Analyzing data in this table one may conclude that:

- In general, addition of FFWD controller improved the system performance. The symbols ↓or ↑ beside the data in FFWD+PID rows indicate the trend of change for that category. The only significant exception to this trend is with $|e_{max}|$ for vertical position.
- In general, addition of extra load and/or positioning did not have remarkable effect on the performance of the controllers (PID or FFWD+PID). The controllers responded properly to the un-modeled extra inertia and force disturbance.

Table 5.5.1: RMSE and e_{max} with PID or FFWD+PID controller

Trajectory		Position		Controller		Test #1	Test #2	Test #3	Test #4	Test #5	Test #6	Test #7	Mean	Std. Dev.
		Horizontal	Vertical	PID	FFWD+PID	RMSE1 RSME2 |e_max|	RMSE1 RSME2 |e_max|	RMSE1 RSME2 |e_max|	RMSE1 RSME2 |e_max|	RMSE1 RSME2 |e_max|	RMSE1 RSME2 |e_max|	RMSE1 RSME2 |e_max|	RMSE1 RSME2 |e_max|	RMSE1 RSME2 |e_max|
1	Sinusoidal (0.5Hz)	✓		✓		2.1	2.1	2.1	2.0	1.9	2.0	2.1	2.0	0.08
						2.1	2.1	2.1	2.0	1.9	2.0	2.1	2.0	0.08
						6.9	7.0	7.0	6.8	6.4	6.7	7.2	6.9	0.25
		✓			✓	1.1	1.1	1.0	1.3	1.7	1.1	1.2	1.2	0.21
						1.1	1.1	1.0	1.3	1.7	1.1	1.2	1.2	0.22
						4.3	4.3	3.8	5.1	10.5	4.6	4.9	5.3	2.12
			✓	✓		2.4	2.5	2.2	2.3	2.3	2.3	2.1	2.3	0.13
						2.4	2.5	2.2	2.3	2.4	2.4	2.1	2.3	0.13
						7.8	7.8	7.3	7.4	7.3	7.3	6.9	7.4	0.30
			✓		✓	1.5	1.9	2.0	1.8	1.8	1.6	1.8	1.8	0.17
						1.5	1.9	2.0	1.9	1.9	1.6	1.8	1.8	0.18
						6.9	11.1	10.9	11.1	8.2	7.5	8.6	9.2	1.67
2	Cycloid (+)	✓		✓		1.4	1.3	1.2	1.2	1.1	1.3	1.3	1.2	0.09
						1.4	1.2	1.1	1.1	1.1	1.2	1.2	1.2	0.09
						5.2	4.8	3.4	3.5	3.1	4.0	3.9	4.0	0.71
		✓			✓	1.3	0.7	0.7	0.9	0.6	1.2	1.2	0.9	0.28
						1.2	0.4	0.4	0.7	0.3	0.8	1.1	0.7	0.33
						7.7	3.9	4.1	5.5	3.0	6.2	7.3	5.4	1.66
			✓	✓		1.4	1.1	1.2	1.6	1.2	1.3	1.3	1.3	0.16
						1.3	1.1	1.1	1.5	1.1	1.1	1.2	1.2	0.14
						5.0	3.1	3.2	6.2	3.2	3.5	4.1	4.0	1.07
			✓		✓	0.8	0.8	0.7	0.8	0.7	0.8	1.0	0.8	0.10
						0.5	0.5	0.3	0.4	0.4	0.5	0.7	0.5	0.11
						4.9	4.9	3.9	4.8	3.6	5.2	6.0	4.7	0.73
3	Cycloid (-)	✓		✓		1.0	1.0	1.0	1.0	0.9	0.9	1.0	1.0	0.04
						0.9	0.9	0.9	0.9	0.8	0.8	0.8	0.9	0.02
						3.3	3.5	3.4	3.4	3.2	3.1	3.3	3.3	0.12
		✓			✓	0.6	0.5	0.5	0.6	0.6	0.5	0.5	0.6	0.05
						0.4	0.4	0.4	0.6	0.5	0.4	0.3	0.4	0.09
						4.0	2.3	2.5	1.7	2.6	2.7	2.9	2.7	0.65
			✓	✓		0.9	1.0	1.0	1.0	1.0	1.0	1.0	1.0	0.04
						0.9	0.9	0.9	0.9	0.9	0.9	0.8	0.9	0.03
						2.5	3.3	3.7	3.5	3.4	3.3	3.3	3.3	0.36
			✓		✓	0.5	0.7	0.5	0.5	0.5	0.3	0.3	0.5	0.11
						0.3	0.5	0.3	0.3	0.3	0.2	0.2	0.3	0.10
						3.4	4.0	2.5	2.5	2.4	2.0	2.3	2.7	0.66
4	Mixed		✓	✓		1.8	1.8	1.8	1.8	1.7	1.7	1.8	1.8	0.04
						1.8	1.8	1.8	1.8	1.7	1.7	1.8	1.8	0.05
						9.8	9.3	9.1	9.5	9.1	8.8	9.4	9.3	0.32
			✓		✓	1.0	0.8	0.9	1.0	0.8	0.9	1.0	0.9	0.08
						0.9	0.8	0.9	0.9	0.7	0.9	1.0	0.9	0.08
						6.3	5.1	6.8	6.4	6.0	5.1	6.2	6.0	0.60

Table 5.5.2: SSE with PID or FFWD+PID controller

Trajectory		Position		Controller		Test #1	Test #2	Test #3	Test #4	Test #5	Test #6	Test #7	Mean
		Horizontal	Vertical	PID	FFWD+PID								
1	Cycloid (+)	✓		✓		-0.1	-0.1	-0.1	0.0	-0.1	-0.1	-0.4	-0.1
		✓			✓	-0.1	-0.1	-0.3	-0.1	-0.1	-0.6	0.0	-0.2
			✓	✓		0.0	-0.1	-0.4	-0.1	-0.1	-0.1	-0.1	-0.1
			✓		✓	-0.1	-0.1	-0.1	-0.1	-0.4	-0.1	-0.1	-0.2
2	Cycloid (-)	✓		✓		0.2	0.3	0.1	0.4	0.1	0.1	0.1	0.2
		✓			✓	0.1	0.4	-0.1	-0.1	0.3	-0.1	0.4	0.1
			✓	✓		0.4	0.4	0.3	0.3	0.4	0.4	0.1	0.3
			✓		✓	-0.1	0.4	0.1	0.1	-0.1	-0.1	0.1	0.1

Table 5.5.3: Mean RMSE1, RMSE2, $|e_{max}|$, and SSE for all tests

Trajectory		Controller		No mass Horizontal	Extra Mass Horizontal	Extra Mass Vertical
		PID	FFWD + PID			
Mean RMSE1						
1	Sinusoidal (0.5 Hz)	✓		2.3	2.0	2.3
			✓	1.3 ↓	1.2 ↓	1.8 ↓
2	Cycloid (+)	✓		1.3	1.2	1.3
			✓	1.0 ↓	0.9 ↓	0.8 ↓
3	Cycloid (-)	✓		1.1	1.0	1.0
			✓	0.6 ↓	0.6 ↓	0.5 ↓
Mean RMSE2						
1	Sinusoidal (0.5 Hz)	✓		2.3	2.0	2.3
			✓	1.3 ↓	1.2 ↓	1.8 ↓
2	Cycloid (+)	✓		1.2	1.2	1.2
			✓	0.8 ↓	0.7 ↓	0.5 ↓
3	Cycloid (-)	✓		1.0	0.9	0.9
			✓	0.4 ↓	0.4 ↓	0.3 ↓
Mean $|e_{max}|$						
1	Sinusoidal (0.5 Hz)	✓		7.7	6.9	7.4
			✓	5.5 ↓	5.3 ↓	9.2 ↑
2	Cycloid (+)	✓		4.6	4.0	4.0
			✓	5.7 ↑	5.4 ↑	4.7 ↑
3	Cycloid (-)	✓		3.5	3.3	3.3
			✓	3.2 ↓	2.7 ↓	2.7 ↓
Mean SSE						
1	Cycloid (+)	✓		±0.2	±0.1	±0.1
			✓	±0.2	±0.2	±0.2
2	Cycloid (-)	✓		±0.4	±0.2	±0.3
			✓	±0.2	±0.1	±0.1

5.6 The Effect of Friction and Compliance on Controlled System

In the previous sections it was shown that the addition of a model based feedforward term to the controller improves the system performance. Here, the effects of friction and compliance of the system are studied in presence of a FFWD+PID controller on the system by utilizing the simulation program.

The manufacturing precision has a remarkable effect on the friction of the system. The friction values were experimentally estimated and were given as two separate sets of friction parameters in (4.5.1.3) and (4.5.1.4). First we assume that the apparatus is made such that the friction parameters are unidirectional meaning these parameters are equal in both directions. The negative direction values from (4.5.1.3) are employed in the simulation. Figure 5.6.1 and 5.6.2 illustrate the system output to a ramp input (trajectory "a"), and a 0.5 Hz sinusoidal input (trajectory "c") respectively.

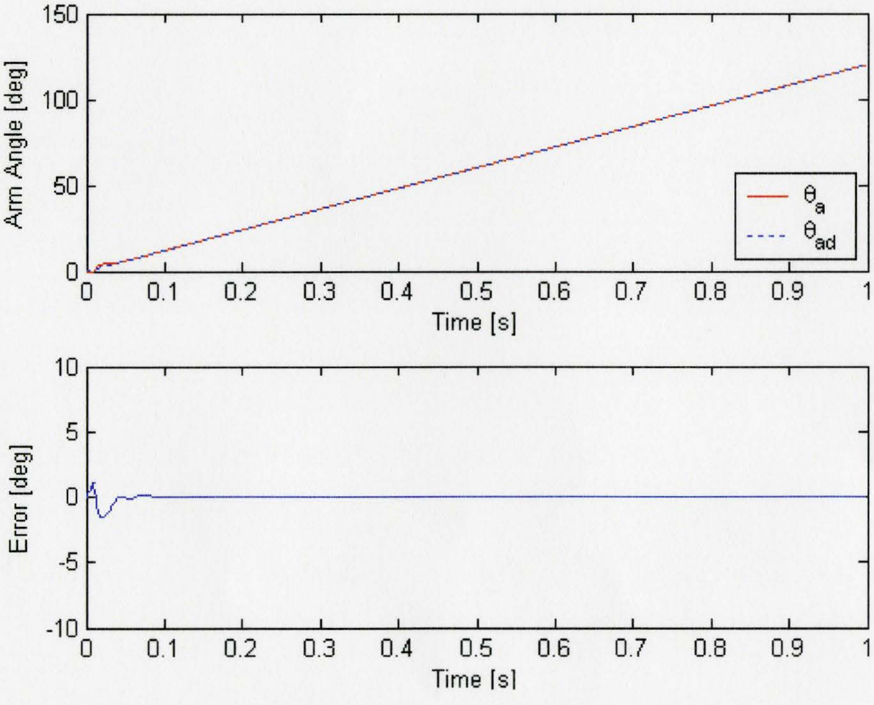

Figure 5.6.1: Positive direction ramp input simulation

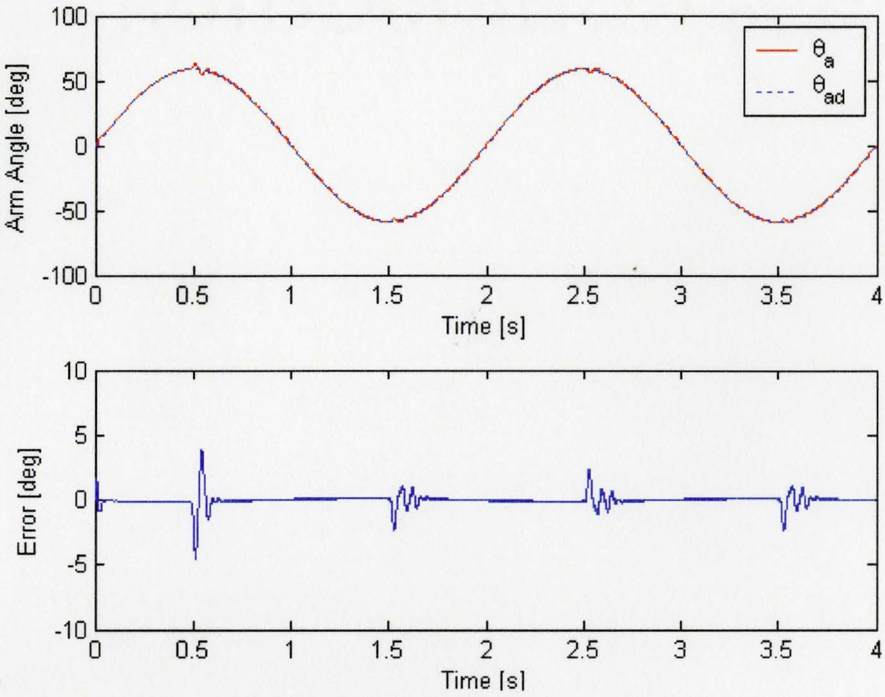

Figure 5.6.2: Sinusoidal (0.5 Hz) input simulation

Table 5.6.1 lists the RMSE1, RMSE2, and e_{max} for all of the simulation results for comparison. Friction is a dominant parameter in the behaviour of the system. To quantify this, the simulation will be repeated with reduced friction values. It is assumed that by proper manufacturing, and utilizing low friction bushings and cylinders, the friction parameters in (4.5.1.3) become one third of their current values:

$$\begin{cases} F_s = 1.35N \\ F_c = 1.00N \\ C_v = 0.0057 Ns/mm \end{cases} \tag{5.6.1}$$

The other parameters are unchanged except the PID parameters which are retuned. Figures 5.6.3 and 5.6.4 present the results for the trajectories "a" and "c" respectively and their numerical indicators are given in Table 5.6.1. e_{max} is significantly reduced in both of the trajectories.

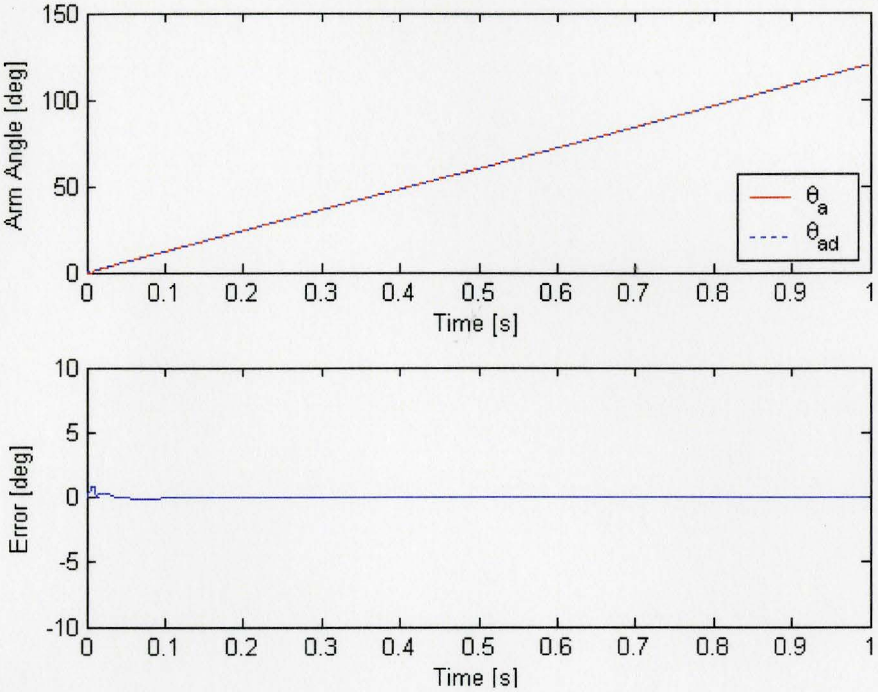

Figure 5.6.3: Positive direction ramp input simulation (reduced friction)

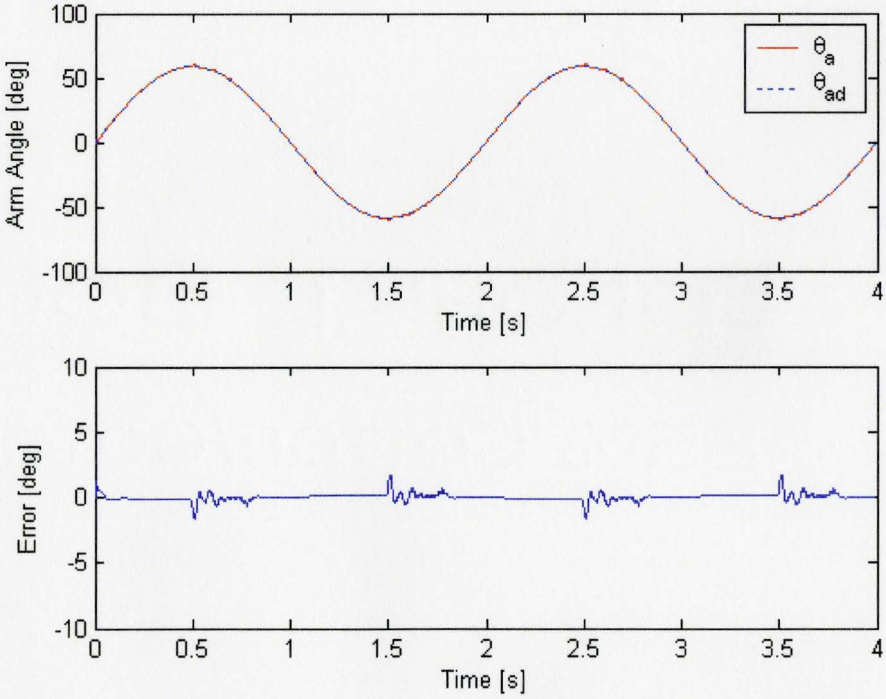

Figure 5.6.4: Sinusoidal (0.5 Hz) input simulation (reduced friction)

Compliance of the system is another element which has a remarkable influence on the duration of the stiction phase. The higher the compliance of the system, the more pump feed will be required to build up the necessary pressure difference in the two hydraulic lines to overcome the static friction and move the rotary arm. Recapping the compliance elements discussed in section 4.4.3, the major causes of the compliance were air bubbles and elasticity of the tubing. If the system is properly sealed then not only air does not penetrate inside the hydraulic lines but also the working pressure can be increased which results a less compressible water-air mixture. The effect of the elasticity of the tubing could also be lessened by using less flexible tubing such as high density polyethylene. Figure 5.6.5 depicts the pressure increase by the change in volume of the water using (4.4.3.11) to (4.4.3.14) and employing a value of *E*=2000 MPa for the modulus of elasticity and *S*=0.5% for the air content of the working fluid. The working pressure is assumed to be higher than 0.5 MPag. These assumptions lead to a value of $\Delta p/\Delta V$=0.15MPa/mm^3.

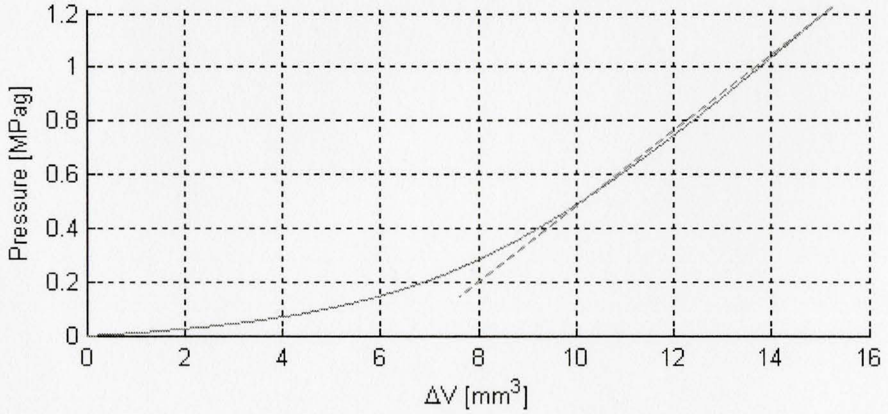

Figure 5.6.5: Pressure vs. volume change for high density polyethylene and *S*=0.5%

The simulation is repeated with the friction values in (5.6.1) but with the new value for $\Delta p/\Delta V$ and retuned PID parameters. Figures 5.6.6 and 5.6.7 illustrate the results for the trajectories "a" and "c" respectively and their numerical indicators are given in Table 5.6.1. Once again e_{max} is significantly reduced in both of the trajectories.

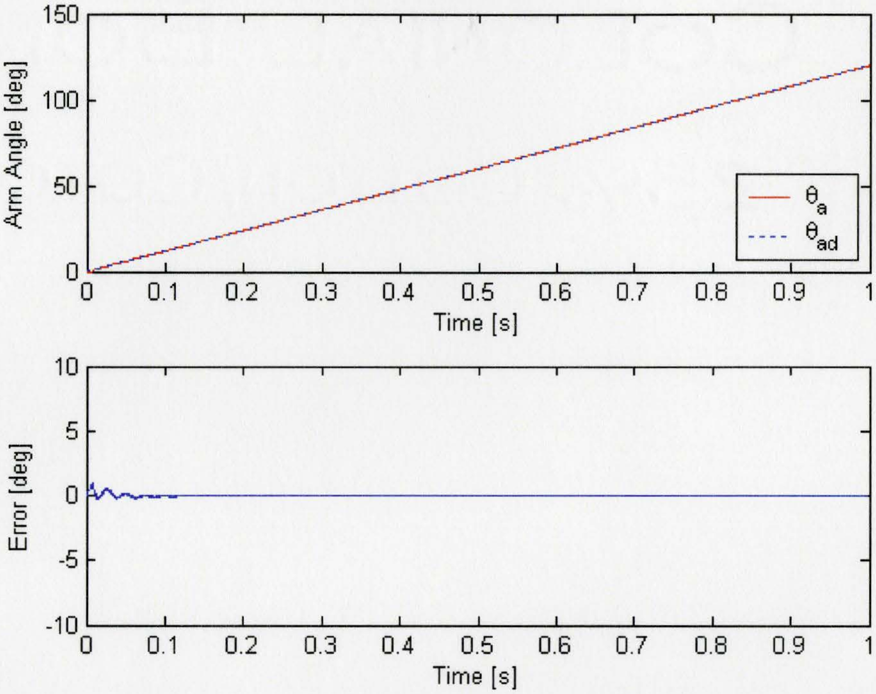

Figure 5.6.6: Positive direction ramp input simulation (reduced compliance)

Comparing the data for reduced friction and compliance with the condition where frictions are equal in both directions in Table 5.6.1, one can observe that the more significant reductions in e_{max} can be achieved by reducing friction or compliance. For sinusoidal input e_{max} has been reduced by 63% and 73% for reduced friction and compliance respectively while for ramp input these values are about 40%. The tracking errors which can be indicated with RMSE1 and RMSE2 are already below 0.5° and 0.2°

for sinusoidal and ramp trajectories without any reduction. However these values are also improved when lower friction or compliance is used in the simulation.

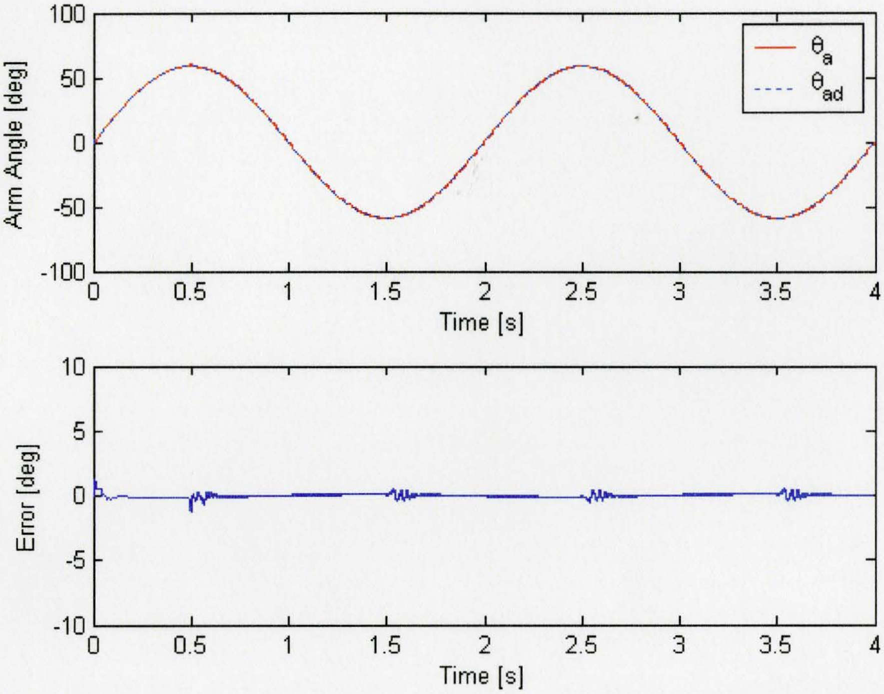

Figure 5.6.7: Sinusoidal (0.5 Hz) input simulation (reduced compliance)

Table 5.6.1: Simulation results for RMSEs and $|e_{max}|$

Trajectory	Indicator	Unidirectional Friction	Reduced Friction	Reduced Compliance
Cycloid (+)	*RMSE1*	0.20	0.08	0.09
	RMSE2	0.02	0.02	0.04
	|e_{max}|	1.58	0.97	0.94
Sinusoidal (0.5 Hz)	*RMSE1*	0.48	0.27	0.15
	RMSE2	0.47	0.26	0.12
	$\|e_{max}\|$	4.53	1.66	1.22

5.7 Conclusion

In this chapter a PID controller was designed and implemented to precisely control the position of the rotary arm. To reduce the effect of the stick-slip phase of motion, an experimentally tuned high frequency signal was added to the control signal to the pump motor. Also PID controller output was smoothed by low-pass filtering its derivative term. Additionally, initial pressure differences adjustment was included in the procedure of the test program before activating the control loop to reduce the initial stiction phase. Different trajectories were tested and output of the system and the errors were recorded.

Next, a model based feedforward term was added to the PID control signal. Overall, the feedforward term improved the performance of the system. The tracking error was reduced by at least 25% compared to a single PID controller while for some trajectories this reduction has been close to 80%. The maximum error was also reduced by at least 20%. The SSE was similar for both of the controllers.

The robustness of the controllers to an un-modelled extra mass and a force disturbance was checked by adding an extra mass to the rotating arm and conducting tests with different trajectories while the arm was rotating in horizontal or vertical directions. The additional mass significantly increased the effective mass of the system. In vertical test this mass added a variable force disturbanc. The results demonstrated notable robustness to both un-modelled inertia and shifting force.

Potential improvement with enhancing friction and compliance of the apparatus were studied through simulations. The results suggest that a considerable improvement in the tracking and maximum errors may be achieved by improving the manufacturing and assembly of future prototypes.

CHAPTER 6

CONCLUSIONS

6.1 Introduction

In this chapter, first a summary of the novel system hardware will be given. Next the controllers are briefly explained and the experimental results are compared with the previous work in our laboratory. Finally a few recommendations for future work are briefly discussed.

6.2 System Hardware

An innovative closed-circuit water hydraulics system was developed in this project including the following subsystems:

1. Pump mechanism: This subsystem was responsible for feeding a controlled volume of water via the precise displacement of two small cylinders (6.35 mm bore). The pump consisted of a servo motor coupled to a linear guide through a ball screw. The position of the linear guide and consequently the two was closed-loop controlled.
2. Rotary joint: A novel slider-pulley mechanism was designed and manufactured to transfer the controlled water feed to a precise rotation of the joint arm. This subsystem consisted of two small cylinders (4 mm bore) connected by hydraulic lines to the pump cylinders and each pushing a slider. The sliders pulled a low

stretch Nylon string wrapped around a pulley. The rotation of the pulley (and arm) was detected by a magnetic rotary encoder.

3. Preload mechanism: A subsystem similar to the pump was added to maintain a preload on the system, and also to compensate for the water lost through leakage in the system. The pressures inside the tubing were measured by two pressure sensors.

6.3 System Modelling and Control

The critical system parameters were identified and modelled. The system compliance due to tubing elasticity and air bubbles, together with the friction were identified as the dominant factors in the dynamics of the system.

A PID controller was first designed to control the arm rotation. A high frequency signal (dither) was added to the controller signal to overcome the transition period from static to sliding friction. Next, a model based feedforward term was added to the control algorithm to enhance the performance of the system. Comparison of the experimental results for both controllers revealed a notable improvement in the system performance when the feedforward term was included. Moreover, a significant improvement may be observed as compared to the results from the previous work undertaken in our laboratory by Sindrey [36]. Table 6.3.1 summarizes the results for the tests conducted in this project with those from the previous work.

Table 6.3.1: Comparison of test results between current and previous works

Trajectory		Current Project Results		Previous Work Results [36]		
		PID	FFWD + PID	PVA	FFWD + PVA	Sliding Mode
Mean RMSE1 (RMSE in [36])						
1	Ramp (+)	1.7	1.1	2.93	2.08	1.55
2	Sinusoidal (0.5 Hz)	2.3	1.3	3.00	2.09	1.69
3	Cycloid (+)	1.3	1.0	4.20	1.40	1.19
4	Mixed	1.7	0.9	–	1.95	1.82
Mean SSE						
1	Cycloid (+)	0.2	0.2	0.41	0.77	0.85

6.4 Recommendations for Future Work

1. Friction is the major problem in this system. In fact the transition period between static to sliding regime produces the largest tracking errors. The effect of reduced friction in reducing tracking and maximum errors was studied through simulations in section 5.6. Precision manufacturing and employing proper materials and components to produce the rotary joint may be the key to achieve a low friction system.
2. The system compliance is another barrier to reaching higher performance as discussed in section 5.6. To lessen this effect, the tubing should be replaced with less elastic ones such as high density polyethylene which also provide some degree of flexibility. Air bubbles are also the next effective element in system compliance which should be avoided so far as possible. In addition,

this effect decreases with an increase in working pressure in the hydraulic lines. The difficulty is that increasing pressure boosts the leakage which in closed-circuit system is not acceptable. Improved fittings should reduce the leakage.

3. In this thesis a preload mechanism roughly controlled the minimum pressures before and after each test. The pump mechanism adjusted the initial pressure differences before starting a test based on the direction of the rotation and static friction for that direction. Then the control loop was initiated and arm rotation was controlled by varying the pump feed. Another alternative is illustrated in Figure 6.4.1.

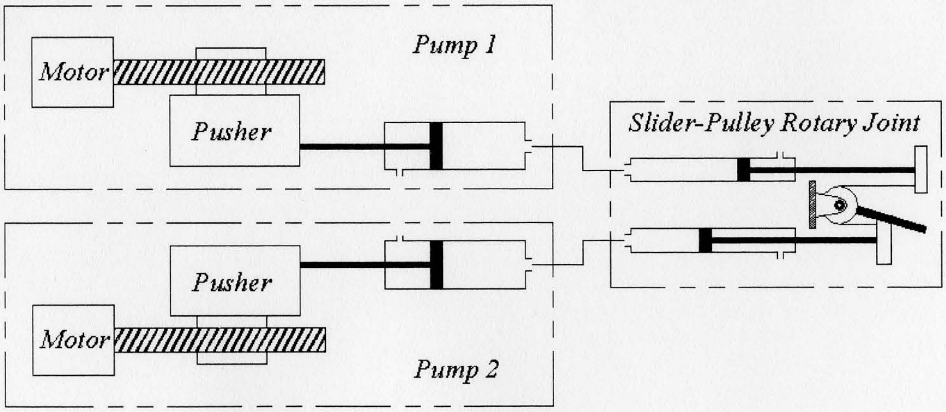

Figure 6.4.1: Alternative system layout

In this configuration the preload mechanism is removed and a second pump is added to the system. Each rotary joint cylinder can be controlled independently through a separate pump. The pump cylinders can also act as the preload in each line and a reservoir to compensate potential leakage. During tests, the control signals can be applied with opposite sign to the pumps. In this case the difficulty may be synchronizing two pumps. Another option could be controlling the two pumps independently. In this case the system becomes a multi-input single-output system which may be more difficult to control than the current single-input single-output system.

REFERENCES

[1] J. M. Hollerbach, I. W. Hunter and J. Ballentyne, "A comparative analysis of actuator technologies for robotics," in *The Robotics Review 2* O. Khatib, J. J. Craig and T. Lozano-Perez, Eds. Cambridge, MA: MIT Press, 1991, pp. 299-342.

[2] S. Davis, D. G. Caldwell, N. Tsagarakis and J. Canderle, "Enhanced modelling and performance in braided pneumatic muscle actuators," International Journal of Robotics Research, vol. 22, pp. 213-227, 2003.

[3] J. D. W. Madden, N. A. Vandesteeg, P. A. Anquetil, P. G. A. Madden, A. Takshi, R. Z. Pytel, S. R. Lafontaine, P. A. Wieringa and I. W. Hunter, "Artificial muscle technology: Physical principles and naval prospects," IEEE Journal of Oceanic Engineering, vol. 29, pp. 706-728, 2004.

[4] G. Monkman, "Micro-actuators: Not so small any more," Assembly Automation, vol. 18, pp. 286-290, 1998.

[5] H. Ishihara, F. Arai, and T. Fukuda, "Micro mechatronics and micro actuators, " IEEE/ASME Transactions on Mechatronics, vol. 1, pp. 68-79, 1996.

[6] M. Cenk Cavusoglu, W. Williams, F. Tendick and S. Shankar Sastry, "Robotics for telesurgery: second generation Berkeley/UCSF laparoscopic telesurgical workstation and looking towards the future applications," Industrial Robot, vol. 30, pp. 22-9, 2003.

[7] M. C. Cavusoglu, F. Tendick, M. Cohn and S. S. Sastry, "Laparoscopic telesurgical workstation, " IEEE Transactions on Robotics and Automation, vol. 15, pp. 728-739, 1999.

[8] S. S. Sastry, M. Cohn and F. Tendick, " Milli-robotics for remote, minimally invasive surgery," Robotics and Autonomous Systems, vol. 21, pp. 305-16, 1997.

[9] R. G. Gilbertson and J. D. Busch, "A Survey of Micro-Actuator Technologies for Future Spacecraft Missions," Journal of Molecular Evolution, vol. 42, pp. 129, 1996.

[10] H. Suzuki, N. Ohya, N. Kawahara, M. Yokoi, S. Ohyanagi, T. Kurahashi and T. Hattori, " Shell-body fabrication for micromachines," Journal of Micromechanics and Microengineering, vol. 5, pp. 36-40, 1995.

[11] A. Teshigahara, M. Watanabe, N. Kawahara, Y. Ohtsuka and T. Hattori, "Performance of a 7-mm microfabricated car, " Journal of Microelectromechanical Systems, vol. 4, pp. 76-80, 1995.

[12] MiniMotor SA: Brushless DC-Servomotors, Retrieved from the World Wide Web: Jan. 2008. http://www.minimotor.ch/uk/welcome_uk.html

[13] Maxon Motor: EC Brushless Motors, Retrieved from the World Wide Web: Jan. 2008. http://www.maxonmotor.com/EC_motor.asp

[14] M. Mehregany, P. Nagarkar, S. D. Senturia and J. H. Lang, "Operation of microfabricated harmonic and ordinary side-drive motors," in Proceedings - IEEE Micro Electro Mechanical Systems: An Investigation of Micro Structures, Sensors, Actuators, Machines and Robots, 1990, pp. 1-8.

[15] T. Fukuda and T. Tanaka, "Micro electro static actuator with three degrees of freedom," in Proceedings - IEEE Micro Electro Mechanical Systems: An Investigation of Micro Structures, Sensors, Actuators, Machines and Robots, 1990, pp. 153-158.

[16] D. C. Roberts, H. Li, J. L. Steyn, K. T. Turner, R. Mlcak, L. Saggere, S. M. Spearing, M. A. Schmidt and N. W. Hagood, "A high-frequency, high-stiffness piezoelectric actuator for microhydraulic applications," in Transducers'01 Eurosensors XV, 2002, pp. 620-631.

[17] T. Morita, "Miniature piezoelectric motors," Sensors and Actuators, A: Physical, vol. 103, pp. 291-300, 2003.

[18] M. Bexell and S. Johansson, "Characteristics of a piezoelectric miniature motor, " Sensors and Actuators, A: Physical, vol. 75, pp. 118-130, 1999.

[19] New Scale Technologies, Inc.: Squiggle Motors, Retrieved from the World Wide Web: Jan. 2008. www.newscaletech.com

[20] V. R. C. Kode and M. C. Cavusoglu, "Design and characterization of a novel hybrid actuator using shape memory alloy and DC micromotor for minimally invasive surgery applications, "IEEE/ASME Transactions on Mechatronics, vol. 12, pp. 455-464, 2007.

[21] F. Daerden and D. Lefeber, "Pneumatic artificial muscles: Actuators for robotics and automation, " European Journal of Mechanical and Environmental Engineering, vol. 47, pp. 11-21, 2002.

[22] D. G. Caldwell, G. A. Medrano-Cerda and M. Goodwin, "Control of pneumatic muscle actuators," IEEE Control Systems Magazine, vol. 15, pp. 40-48, 1995.

[23] Y. K. Lee and I. Shimoyama, "A skeletal framework artificial hand actuated by pneumatic artificial muscles" in proceedings – IEEE International Conference on Robotics and Automation, 1999, pp. 926-931

[24] M. C. Birch, R. D. Quinn, G. Hahm, S. M. Phillips, B. Drennan, A. Fife, H. Verma, and R. D. Beer, "Design of a cricket microrobot" in proceedings – IEEE International Conference on Robotics and Automation, 2000, pp. 1109-1114

[25] K. Suzumori, S. Iikura and H. Tanaka, "Development of flexible microactuator and its applications to robotic mechanisms," in Proceedings – IEEE International Conference on Robotics and Automation, 1991, pp. 1622-7.

[26] J. Peirs, D. Reynaerts and H. Van Brussel, "Design of miniature parallel manipulators for integration in a self-propelling endoscope," Sensors and Actuators, A: Physical, vol. 85, pp. 409-417, 2000.

[27] Parker Hannifin Corp.: Pneumatic rotary actuators, Retrieved from the World Wide Web: July 2006. http://www.parker.com/ead/cm2.asp?cmid=11128

[28] J. Heintze, G. van Schothorst, van der Weiden, A.J.J. and P. C. Teerhuis, "Modeling and control of an industrial hydraulic rotary vane actuator," in Proceedings of 32nd IEEE Conference on Decision and Control, 1993, pp. 1913-18.

[29] J. L. Shearer, "Study of pneumatic processes in the continuous control of motion with compressed air (I,II)," in ASME Transaction 78 (2), 1956, pp. 233-249.

[30] M. C. Shih and S. I. Tseng, "Identification and position control of a servo pneumatic cylinder, " Control Engineering Practice, vol. 3, pp. 1285-1290, 1995.

[31] Z. Rao and G. M. Bone, "Modeling and control of a miniature servo pneumatic actuator, " in 2006 IEEE International Conference on Robotics and Automation, ICRA 2006, 2006, pp. 1806-1811.

[32] R. B. van Varseveld and G. M. Bone, "Accurate position control of a pneumatic actuator using on/off solenoid valves," in Proceedings of the 1997 IEEE International Conference on Robotics and Automation, ICRA. Part 2 (of 4), Apr. 20-25 1997, 1997, pp. 1196-1201.

[33] H. Murrenhoff, "Systematic approach to the control of hydrostatic drives," Proceedings of the Institution of Mechanical Engineers. Part I: Journal of Systems and Control Engineering, vol. 213, pp. 333-347, 1999.

[34] Danfoss Group Global: High Pressure Water Solutions, Retrieved from the World Wide Web: July 2007. http://www.danfoss.com.libaccess.lib.mcmaster.ca/BusinessAreas/High-pressure_Water_Solutions/Hydraulics/Products.htm

[35] S. H. Cho, M. Linjama, H. Sairiala, K. T. Koskinen and M. Vilenius, "Sliding mode tracking control of a low-pressure water hydraulic cylinder under non-linear friction," Proceedings of the Institution of Mechanical Engineers. Part I: Journal of Systems and Control Engineering, vol. 216, pp. 383-392, 2002.

[36] R. Sindrey, "Design and control of a miniature rotary joint, " M. A. Sc. thesis, McMaster University, Hamilton, ON, Canada, 2006.

[37] R. Sindrey and G. M. Bone, "Position tracking control of miniature low pressure water hydraulic cylinders, " in ASME International Mechanical Engineering Congress & Exposition, 2007.

[38] J. J. Thomsen, "Some general effects of strong high-frequency excitation: stiffening, biasing and smoothening," Journal of Sound and Vibration, vol. 253, pp. 807-31, 2002.

[39] M. A. Michaux, A. A. Ferri and K. A. Cunefare, "Effect of tangential dither signal on friction induced oscillations in an SDOF model, Journal of Computational and Nonlinear Dynamics, vol. 2, pp. 201-210, 2007.

[40] Airpot Corp.: Anti-stiction air cylinders, Retrieved from the World Wide Web: July 2007. http://airpot.com/beta/html/exhibit31.html

[41] M. De Volder, J. Peirs, D. Reynaerts, J. Coosemans, R. Puers, O. Smal and B. Raucent, "Production and characterization of a hydraulic microactuator," Journal of Micromechanics and Microengineering, vol. 15, pp. 15-21, 07. 2005.

[42] M. De Volder, F. Ceyssens, D. Reynaerts and R. Puers, "A PDMS lipseal for hydraulic and pneumatic microactuators, " Journal of Micromechanics and Microengineering, vol. 17, pp. 1232-7, 07. 2007.

[43] W. S. Owen, E. A. Croft and J. R. McFarlane, "Reducing stick-slip friction in hydraulic actuators," in proceedings - IEEE/ASME International Conference on Advanced Intelligent Mechatronics, 2001, pp. 642-7.

[44] A. G. Erdman, G.N.Sandor, *Mechanism Design: Analysis and Synthesis, Vol. 1.* N.J.: Prentice Hall, 1984, pp. 17- 19.

[45] E. Trostmann, *Water Hydraulics Control Technology.* New York: Marcel Dekker Inc., 1996, pp. 11-15.

[46] V. L. Streeter, *Handbook of Fluid Dynamics.* New York: McGraw-Hill, 1961, p. 3.18-3.22, and 21.13-21.26.

[47] D. McCloy and Martin H.R., *Control of Fluid Power: Analysis and Design.* New York: Halsted Press, 1980, pp. 31-36.

[48] J. E. Shigley, C. R. Mischke, *Standard Handbook of Machine Design.* New York: McGraw-Hill, 1986, pp. 17.7-17.14.

Coulomb friction (*Fc*) and viscous friction coefficient (*Cv*)

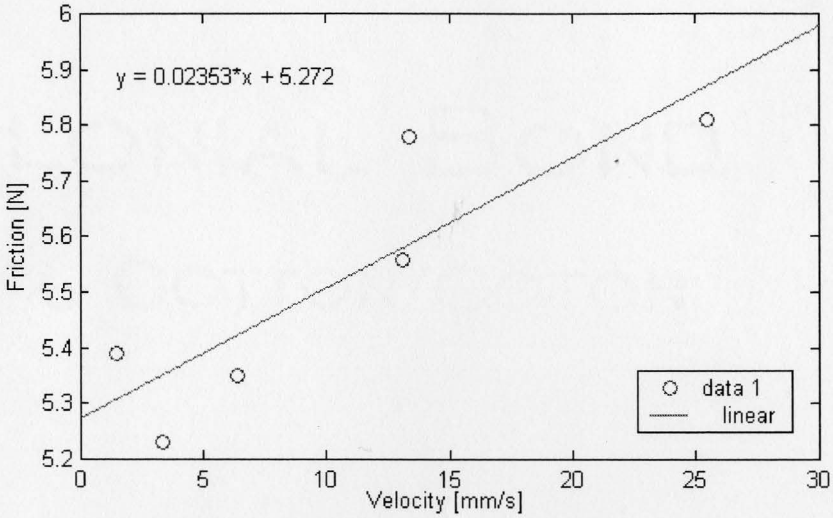

Figure A.1: Coulomb and viscous friction vs. slider velocity (positive direction)

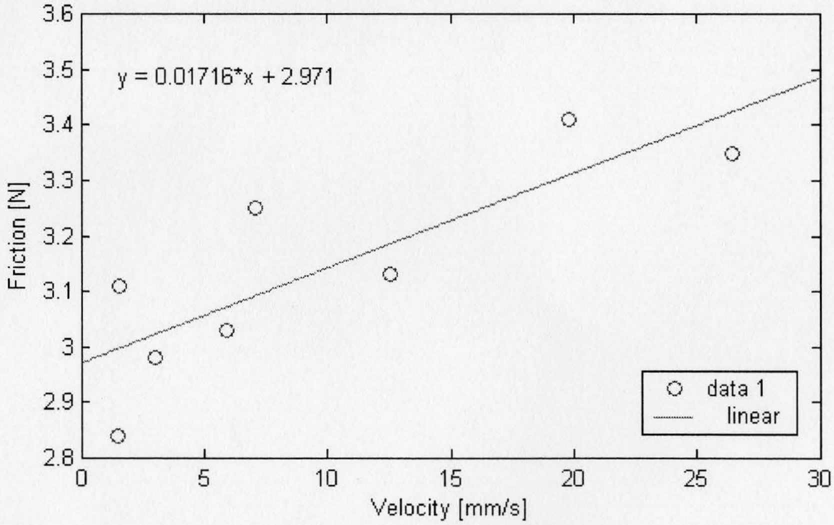

Figure A.2: Coulomb and viscous friction vs. slider velocity (negative direction)